Electromagnetic Wave Scattering by Discrete Random Media with Remote Sensing Applications

by

Chi On Ao

A.B., University of California, Berkeley (1993)

Submitted to the Department of Physics
in partial fulfillment of the requirements for the degree of

Doctor of Philosophy

at the

MASSACHUSETTS INSTITUTE OF TECHNOLOGY

June 2001

Author . . . .
Department of Physics
May 18, 2001

Certified by . . . .
Jin Au Kong
Professor, Department of Electrical Engineering and Computer Science
Thesis Supervisor

Accepted by . . . .
Thomas J. Greytak
Professor, Associate Department Head for Education

Electromagnetic Wave Scattering by Discrete Random Media with Remote Sensing Applications

by

Chi On Ao

Submitted to the Department of Physics
on May 18, 2001, in partial fulfillment of the
requirements for the degree of
Doctor of Philosophy

Abstract

The scattering of electromagnetic waves in medium with randomly distributed discrete scatterers is studied. Analytical and numerical solutions to several problems with implications for the active and passive remote sensing of the Earth environment are obtained.

The quasi-magnetostatic (QMS) solution for a conducting and permeable spheroid under arbitrary excitation is presented. The spheroid is surrounded by a weakly conducting background medium. The magnetic field inside the spheroid satisfies the vector wave equation, while the magnetic field outside can be expressed as the gradient of the Laplace solution. We solve this problem exactly using the separation of variables method in spheroidal coordinates by expanding the internal field in terms of vector spheroidal wavefunctions. The exact formulation works well for low to moderate frequencies; however, the solution breaks down at high frequency due to numerical difficulty in computing the spheroidal wavefunctions. To circumvent this difficulty, an approximate theory known as the small penetration-depth approximation (SPA) is developed. The SPA relates the internal field in terms of the external field by making use of the fact that at high frequency, the external field can only penetrate slightly into a thin skin layer below the surface of the spheroid. For spheroids with general permeability, the SPA works well at high frequency and complements the exact formulation. However, for high permeability, the SPA is found to give accurate broadband results. By neglecting mutual interactions, the QMS frequency response from a collection of conducting and permeable spheroids is also studied.

In a dense medium, the failure to properly take into account of multiple scattering effects could lead to significant errors. This has been demonstrated in the past from extensive theoretical, numerical, and experimental studies of electromagnetic wave scattering by densely packed dielectric spheres. Here, electromagnetic wave scattering by dense packed dielectric spheroids is studied both numerically through Monte Carlo simulations and analytically through the quasi-crystalline approximation (QCA) and QCA with coherent potential (QCA-CP). We assume that the spheroids are electrically small so that single-particle scattering is simple.

In the numerical simulations, the Metropolis shuffling method is used to generate realizations of configurations for non-interpenetrable spheroids. The multiple scattering problem is formulated with the volume integral equation and solved using the method of moments with electrostatic basis functions. General expressions for the self-interaction elements are obtained using the low-frequency expansion of the dyadic Green's function, and radiative correction terms are included. Results of scattering coefficient, absorption coefficient, and scattering matrix for spheroids in random and aligned orientation configurations are presented. It is shown that independent scattering approximation can give grossly incorrect results when the fractional volume of the spheroids is appreciable.

In the analytical approach, only spheroids in the aligned configuration are solved. Low-frequency QCA and QCA-CP solutions are obtained for the average Green's function and the effective permittivity tensor. For QCA-CP, the low-frequency expansion of the uniaxial dyadic Green's function is required. The real parts of the effective permittivities from QCA and QCA-CP are compared with the Maxwell-Garnett mixing formula. QCA gives identical result to the mixing formula, while QCA-CP gives slightly higher values. The extinction coefficients from QCA and QCA-CP are compared with results from Monte Carlo simulations. Both QCA and QCA-CP agree well with simulations, although qualitative disagreement is evident at higher fractional volumes.

QCA can also be used with Mie scattering to yield solution that is valid for particle sizes comparable to or larger than the wavelength. This formulation is used to investigate thermal emission from sea foam, which is modeled here as a layer of randomly distributed air bubbles coated with sea water. The extinction behavior of sea foam is illustrated, and the extinction is shown to be dominated by absorption. Using QCA-derived parameters, the radiative transfer equation is solved. The brightness temperatures of the sea foam are presented as a function of observation angle and frequency. Large-scale rough ocean effects are also considered using a simple geometric tilting model. The final result is found by averaging the brightness temperatures over the Cox-Munk slope distribution. Thus a physical model of foam emission is obtained that relates observed brightness temperatures to the microstructure of foam as well as ocean surface wind vector.

Thesis Supervisor: Jin Au Kong
Title: Professor, Department of Electrical Engineering and Computer Science

Acknowledgments

This thesis would not be possible without the support and encouragement from Professor Kong, who introduced me to the fascinating world of electromagnetics and remote sensing. I appreciate greatly the conversations we had, the invaluable advices that he shared with me, and his wonderful sense of humor. Professor Kong's breadth of knowledge and the seemingly effortless way he could explain difficult concepts in simple terms never cease to amaze me.

During the course of my thesis research, I had the fortune to collaborate closely with several outstanding people. I am grateful to Ben Barrowes, Henning Braunisch, Kung-Hau Ding, Kevin O'Neill, and Yan Zhang for their insightful comments and suggestions. I would also like to thank Professor Leung Tsang, whose pioneering work on dense medium scattering has been a source of inspiration for my own research in this area. I am also grateful to Group 44 at Lincoln Laboratory for supporting me with a research assistantship and Mark Dickson for fruitful discussions.

I wish to thank Professor John Joannopoulos and Professor Michael Feld for agreeing to be in my thesis committee and for their helpful comments.

It also gives me great pleasure to acknowledge my colleagues at the Center for Electromagnetic Theory and Applications. To Ben Barrowes, Henning Braunisch, Kung-Hau Ding, Tomasz Grzegorczyk, Chris Moss, Peter Orondo, Joe Pacheco, Sang-Hoon Park, Sean Shih, Fernando Teixeira, Bae-Ian Wu, Eric Yang, and Yan Zhang, I thank you for your friendship and for your help. I enjoyed the many hours of lively exchanges (technical or not) that we had and look forward to future collaborations. I wish you the best of luck in your professional endeavors and personal lives.

Last but not least, I wish to express my deepest gratitude to my parents, my sister, and my brother for their unconditional love and support. Thank you for keeping me afloat when I was down and thank you, by always being there when I needed you, for reminding me the goodness of life.

For my parents

Contents

List of Figures

List of Tables

Chapter 1

Introduction

In this thesis, several problems related to the scattering of electromagnetic waves in discrete random media are studied. These problems are motivated by applications in the remote sensing of the Earth environment. However, the methodologies are theoretically and numerically oriented and aim to enrich our basic physical understanding of wave interactions with matter.

A discrete random medium consists of scatterers of simple shapes and material properties randomly distributed in a homogeneous background. The scattering characteristics of such a medium is generally described in an ensemble averaging sense. The discrete random medium provides a convenient model for a variety of geophysical, biological, and artificial systems.

We can classify a discrete random medium according to its scattering properties into two categories: *sparse* and *dense*. In a sparse medium, multiple scattering is negligible. This could be so because (*i*) particle concentration is low such that the mean separation of the scatterers is much larger than the wavelength, (*ii*) the material contrast is low such that the scattering strength from each scatterer is weak, and/or (*iii*) the scattered field falls off quickly in the background medium. Thus in a sparse medium, the total response is simply the sum of the individual responses from each scatterer in isolation. In contrast, in a dense medium, the scatterers are packed closely together with significant scattering. Hence multiple scattering effects must be properly included to get the correct results.

For a sparse medium, the challenge is to solve the single-particle scattering problem. Except for special cases such as spherical objects (Mie scattering) or small ellipsoidal particles (Rayleigh scattering) [1, 2, 3, 4], this is not always easy to do [5]. For dense medium, one faces the additional task of combining the scattered fields from all the particles in a self-consistent manner. One must also be able to come up with reasonable ways to characterize the joint probability distribution of the particle positions and other possible properties [6, 7, 8, 9].

In Chapter 2, I present the quasi-magnetostatic (QMS) field solution for conducting and permeable spheroids under arbitrary excitation. This problem is motivated by the need to discriminate subsurface unexploded ordnance (UXO) using the newly developed electromagnetic induction spectroscopy (EMIS) sensors. Much efforts will be devoted in the single spheroid solution because (*i*) the exact formulation, which is in terms of spheroidal wavefunction expansion, is fairly involved and (*ii*) mutual interactions between the spheroids are negligible largely due to the non-conductive nature of the background medium. Thus the QMS multiple spheroid problem can be considered to be a sparse medium. Subsequent chapters deal with dense medium.

So far I have used the term “multiple scattering” somewhat loosely. It is important to recognize in wave scattering and propagation through discrete random medium, there exists two scattering length scales. The first involves multiple scattering of *fields* and is known as coherent multiple scattering. Coherent multiple scattering is used for the classification of sparse and dense media. The length scale of coherent multiple scattering is characterized by the wavelength λ. The second involves multiple scattering of *intensities* and is known as incoherent multiple scattering. The length scale is characterized by the mean free path l_{mfp}. Incoherent multiple scattering has been treated thoroughly with the classical radiative transfer theory [4, 10, 11]. Coherent multiple scattering is a subject of extensive current research activities [12, 13]. In the event where $l_{\mathrm{mfp}} \gg \lambda$, as is the case in most geophysical remote sensing problems, both the coherent and incoherent multiple scattering can be combined in an elegant way in the so-called dense medium radiative transfer theory [9, 14]. This is achieved by calculating radiative transfer parameters such as absorption coefficient and scattering phase matrix using wave theory that incorporates coherent multiple scattering. These "mesoscopic" radiative transfer parameters are then used in the radiative transfer equation to solve the large-scale or "macroscopic" problem. Chapters 3–5 are studied in the context of dense medium radiative transfer theory.

In Chapters 3 and 4, the coherent multiple scattering of electromagnetic waves by dielectric spheroids is studied. While the problem of multiple scattering by spheres has been studied extensively, multiple scattering by nonspherical particles remain an underexplored subject, despite its relevance in many remote sensing applications (for example, sea ice and vegetation). The spheroids provide perhaps the simplest nonspherical model with which to study multiple scattering. I assume that the spheroids are small compared to the wavelength so that single scattering can be characterized essentially by Rayleigh scattering. The problem of multiple scattering by spheroids will be tackled from two directions, by using Monte Carlo simulations as well as analytical approximations that are based on wave theory. The Monte Carlo simulations are computationally time-consuming but allow for rather general spheroid distributions. The analytical approximations are derived only for spheroids with aligned orientation but give close-form solutions in the low-frequency limit. However, the approximations only take into account of pair correlation and might not give the correct results at high fractional volume. Results obtained using numerical simulations and analytical approximations are compared.

In Chapter 5, I study the problem of polarimetric thermal emission from sea foam. It has been known since the late 1960s that sea foam has microwave emissivities close to one, which represent twice the emission from the plain sea surface. Thus even though only a small portion of the sea surface is covered with foam, their effects on the overall emissivity measurements of the ocean need to be properly accounted for. The goal here is to develop a general electromagnetic model for foam emission that could relate to the underlying physical parameters of the foam and that does not place any strict limitation on particle size or frequency. To this end, we model the sea foam as a layer of randomly distributed, densely packed air bubbles. Each air bubble is taken to be spherical and coated with a thin outer layer of sea water. Coherent multiple scattering is incorporated using the analytical theory of quasi-crystalline approximation (QCA) with T-matrix formulation (known as the QCA-Mie theory). This allows the bubble size comparable or larger than the wavelength to be treated. Brightness temperatures from a foam-covered ocean surface are derived by solving the dense medium radiative transfer equation.

Chapter 2

Quasi-Magnetostatic Solution for Conducting and Permeable Spheroids

2.1 Introduction

The detection and identification of buried unexploded ordnance (UXO) is important from the prospective of humanitarian demining. Electromagnetic methods from ground penetrating radar (GPR) to electromagnetic induction (EMI) devices are useful in detecting these objects [15]. However, it is considerably more difficult to identify or discriminate between the responses from objects with different shapes and material properties. The uncertainty in target identification leads to a high false alarm rate and renders the UXO removal process costly.

The development of advanced broadband induction devices has prompted researchers to investigate the electromagnetic induction (EMI) frequency response from subsurface metallic objects [16, 17]. These devices measure the in-phase and quadrature magnetic field responses in a broad range of frequencies ($\sim$ 30 Hz–20 kHz). By operating in these low frequencies, the ground surface effects can conveniently be ignored. Measurements on typical ordnance have revealed significant differences in frequency responses depending on their sizes and orientations. Since UXO are generally nonspherical, it is desirable, for the purpose of physical interpretations and data analysis, to be able to compute theoretically the EMI response from nonspherical objects. However, while the EMI response from a conducting and permeable sphere is well-known [18, 19], the corresponding analytical and/or numerical solutions for nonspherical objects did not exist until recently [20, 21, 22, 23].

One of the simplest nonspherical shapes that lends itself to theoretical analysis is the prolate or oblate spheroid (ellipsoid of revolution). The spheroid also provides a versatile model for nonspherical object that ranges from long needles to spheres to flat discs. In this chapter, we obtain the quasi-magnetostatic (QMS) solution for conducting and permeable spheroids under *arbitrary* excitation using the separation of variables method. By "arbitrary," we mean that the primary field can be oriented in an arbitrary direction with respect to the symmetry axis of the spheroid and can be spatially non-uniform in general. This extends our previous work [20], in which the special case of axial excitation (i.e., the primary field is constant in magnitude and oriented along the symmetry axis of the spheroid) was considered. By exploiting the azimuthal symmetry of the problem, the axial-excitation problem can be formulated using only the *scalar* spheroidal wavefunction. In the general formulation presented here, the *vector* spheroidal wavefunctions must be used.

It should be noted that vector spheroidal wavefunctions expansion is a technique that has been used extensively to study electromagnetic wave scattering by dielectric spheroids [24, 25, 26, 27]. However, our problem differs from the usual scattering problems in the following important ways. First, in the QMS regime, the displacement current is negligible compared to the conduction current. This results in the dispersion relation $k^2 = i\omega\sigma\mu$, where σ is the conductivity and μ is the permeability of the medium. Thus the physical nature of the present problem is more properly described as diffusion instead of scattering. Second, the external field is taken to be *static* (in the sense that $k = 0$ — the external field still oscillates in time with $e^{-i\omega t}$). While this can be regarded formally as the limit of the *wave* problem as the wavenumber $k \to 0$, we prefer not to do so to bypass the anticipated analytical and numerical difficulties in performing such a limit.

The rest of this chapter proceeds as follows. In Sec. 2.2, we present the exact formulation based on vector spheroidal wavefunction expansion for a prolate spheroid. In Sec. 2.3, numerical results are shown for the case of uniform primary field excitation. Due to numerical difficulty in computing the spheroidal wavefunctions for high frequencies, an alternate system of equations for the external field is derived by introducing and making use of the small penetration-depth approximation (SPA). This is described in Sec. 2.4. For general parameters, SPA is valid at high frequencies and complements the exact solution. For high relative permeability, SPA is found to give an accurate solution over *all* frequencies. In Sec. 2.5, we extend the SPA to oblate spheroids. In Sec. 2.6, we investigate the EMI response due to a collection of spheroids by assuming that they comprise a sparse medium. The results are summarized in Sec. 2.7.

2.2 Exact Formulation

A conducting and permeable prolate spheroid is placed in a weakly conducting homogeneous background and excited by a time-harmonic primary magnetic field $\overline{H}_o(\overline{r})e^{-i\omega t}$ (Fig. 2-1). The time dependence expression of $e^{-i\omega t}$ is suppressed below. In the quasi-magnetostatic regime, we assume that the displacement current can be neglected in comparison to the conduction current. The magnetic field inside the spheroid satisfies the vector wave equation [28]

$$\nabla \times \nabla \times \overline{H}_1 - k_1^2 \overline{H}_1 = 0 \tag{2.1}$$

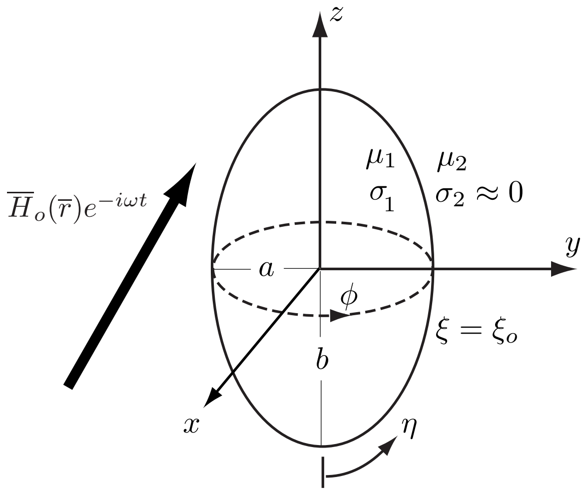

Figure 2-1: A conducting and permeable prolate spheroid is excited by a time-harmonic primary field $\overline{H}_o(\overline{r})e^{-i\omega t}$. The prolate spheroidal coordinate system is specified by (η, ξ, ϕ) with $-1 \leq \eta \leq 1$, $1 \leq \xi < \infty$, and $0 \leq \phi < 2\pi$. The surface of the spheroid is given by $\xi = \xi_o = b/\sqrt{b^2 - a^2}$.

with $k_1^2 = i\omega\sigma_1\mu_1$. Thus the field inside the spheroid ($\xi < \xi_o$) can be expanded using the (divergence-free) vector spheroidal wavefunctions of first kind [29], which are regular at the origin:

$$\overline{H}_1 = H_o \sum_{m=0}^{\infty} \sum_{n=m}^{\infty} \sum_{p=0}^{1} \left[A_{pmn}^{(M)} \overline{M}_{pmn}^{r(1)}(c_1; \eta, \xi, \phi) + A_{pmn}^{(N)} \overline{N}_{pmn}^{r(1)}(c_1; \eta, \xi, \phi) \right] \tag{2.2}$$

where H_o is a constant and the dimensionless spheroidal frequency parameter c_1 is defined as

$$c_1 = k_1 \frac{d}{2} \tag{2.3}$$

with $d = 2\sqrt{b^2 - a^2}$ being the focal distance. The vector wavefunctions can be generated from the scalar wavefunction as follows:

$$\overline{M}_{pmn}^{r(1)} = \nabla \psi_{pmn}^{(1)} \times \overline{r} \tag{2.4}$$

$$\overline{N}_{pmn}^{r(1)} = \frac{1}{k_1} \nabla \times \overline{M}_{pmn}^{r(1)} \tag{2.5}$$

with

$$\psi^{(1)}_{pmn} = S_{mn}(c_1,\eta) R^{(1)}_{mn}(c_1,\xi) T_{pm}(\phi) \tag{2.6}$$

where $S_{mn}(c_1,\eta)$ and $R^{(1)}_{mn}(c_1,\xi)$ are the spheroidal angle and radial functions, respectively, while the azimuthal function $T_{pm}(\phi)$ is simply

$$T_{pm}(\phi) = \begin{cases} \cos m\phi, & p=0 \\ \sin m\phi, & p=1 \end{cases} \tag{2.7}$$

Note that other choices for generating the vector wavefunctions are possible besides (2.4) and (2.5), cf. [27, 29]. The r-vector wavefunctions used here represent a common choice for scattering problems [25, 26].

To simplify notation, the superscripts (1) and r on the spheroidal wavefunctions will henceforth be dropped. Unless otherwise indicated, we will also dispense with the explicit dependence of the spheroidal wavefunctions on c_1.

Outside the spheroid, the medium is poorly conducting and weakly magnetic. Thus $k_2 \to 0$ in the quasi-static limit, and the magnetic field can be obtained from its scalar potential, which satisfies the Laplace equation. We define a scalar potential $U_2(\overline{r})$ such that the external magnetic field is $\overline{H}_2 = -\nabla U_2$. The total external magnetic field can be written as a sum of the primary and secondary fields, i.e.,

$$\overline{H}_2 = \overline{H}_o + \overline{H}^{(\mathrm{s})}_2 = -\nabla U_o - \nabla U_\mathrm{s} \tag{2.8}$$

The primary field potential $U_o(\overline{r})$ is expanded as

$$U_o(\overline{r}) = \frac{H_o d}{2} \sum_{m=0}^{\infty} \sum_{n=m}^{\infty} \sum_{p=0}^{1} b_{pmn} \Phi^{(1)}_{pmn}(\eta,\xi,\phi) \tag{2.9}$$

where

$$\Phi^{(1)}_{pmn}(\eta,\xi,\phi)=P_n^m(\eta)P_n^m(\xi)T_{pm}(\phi) \tag{2.10}$$

is the spheroidal Laplace solution of first kind which is regular at the origin ($\xi \rightarrow 1$). The source coefficients b_{pmn} are determined from the primary field. The functions $P_n^m(\eta)$ and $P_n^m(\xi)$ are the associated Legendre functions of first kind. The associated Legendre functions used here follow the convention of Abramowitz and Stegun [30] (eqs. 8.6.6 and 8.6.7), which is slightly different from that of Flammer [29].

Similarly, the secondary magnetic field potential $U_s(\overline{r})$ can be expanded as

$$U_{\mathrm{s}}(\overline{r}) = \frac{H_o d}{2}\sum_{m=0}^{\infty}\sum_{n=m}^{\infty}\sum_{p=0}^{1} B_{pmn}\Phi_{pmn}(\eta,\xi,\phi) \tag{2.11}$$

where

$$\Phi_{pmn}(\eta,\xi,\phi)=P_n^m(\eta)Q_n^m(\xi)T_{pm}(\phi) \tag{2.12}$$

is the spheroidal Laplace solution of second kind which is regular at infinity ($\xi \rightarrow \infty$). The function $Q_n^m(\xi)$ is the associated Legendre functions of first kind.

The boundary conditions are specified by the continuity of tangential components of $\overline{H}$ and normal component of $\overline{B}$ at the surface of the spheroid $\xi = \xi_o$ [28]:

$$H_{1\eta}=H_{2\eta} \tag{2.13}$$

$$H_{1\phi}=H_{2\phi} \tag{2.14}$$

$$\mu_r H_{1\xi}=H_{2\xi} \tag{2.15}$$

where $\mu_r = \mu_1/\mu_2$ is the relative permeability of the spheroid with respect to its surrounding.

The vector spheroidal wavefunctions in component forms are given in Appendix A.

In matching the boundary conditions, first note that from (2.7),

$$\frac{dT_{pmn}}{d\phi} = (-1)^{\tilde{p}} m T_{\tilde{p}mn}(\phi) \tag{2.16}$$

where $\tilde{p} = 0$ for $p = 1$ and vice versa. Then matching the angular component H_η according to (2.13) gives

$$\begin{aligned} &\sum_{n=m}^{\infty} \left[(-1)^p m A^{(M)}_{\tilde{p}mn} \widetilde{M}_{\eta;mn}(\eta, \xi_o) + \frac{1}{c_1} A^{(N)}_{pmn} \widetilde{N}_{\eta;mn}(\eta, \xi_o) \right] \\ &\qquad = -\sum_{n=m}^{\infty} \left[b_{pmn} P_n^m(\xi_o) + B_{pmn} Q_n^m(\xi_o) \right] \frac{dP_n^m}{d\eta} \end{aligned} \tag{2.17}$$

where we have made use of the orthogonality property of $\cos m\phi$ and $\sin m\phi$ to eliminate the sum over the indices m and p. However, the sum over n must be retained because no such orthogonality condition exists between the angular functions $S_{mn}(c, \eta)$ and $P_n^m(\eta) = S_{mn}(c = 0, \eta)$. In general, $S_{mn}(c, \eta)$ and $S_{mn}(c', \eta)$ are orthogonal only when $c = c'$. This accounts for the complexity of the two-media spheroidal boundary value problem.

Similarly, matching H_ξ according to (2.15) gives

$$\begin{aligned} &\mu_r \sum_{n=m}^{\infty} \left[(-1)^p m A^{(M)}_{\tilde{p}mn} \widetilde{M}_{\xi;mn}(\eta, \xi_o) + \frac{1}{c_1} A^{(N)}_{pmn} \widetilde{N}_{\xi;mn}(\eta, \xi_o) \right] \\ &\qquad = -\sum_{n=m}^{\infty} \left[b_{pmn} \frac{dP_n^m}{d\xi_o} + B_{pmn} \frac{dQ_n^m}{d\xi_o} \right] P_n^m(\eta) \end{aligned} \tag{2.18}$$

Matching H_ϕ according to (2.14) gives the third set of equations

$$\begin{aligned} &\sum_{n=m}^{\infty} \left[(-1)^{p+1} A^{(M)}_{\tilde{p}mn} \widetilde{M}_{\phi;mn}(\eta, \xi_o) + \frac{m}{c_1} A^{(N)}_{pmn} \widetilde{N}_{\phi;mn}(\eta, \xi_o) \right] \\ &\qquad = -\sum_{n=m}^{\infty} m \left[b_{pmn} P_n^m(\xi_o) + B_{pmn} Q_n^m(\xi_o) \right] P_n^m(\eta) \end{aligned} \tag{2.19}$$

Equations (2.17), (2.18), and (2.19) are used to determine the field expansion coefficients $A^{(M)}_{pmn}$, $A^{(N)}_{pmn}$, B_{pmn}. Further simplifications can be made by considering the parity of the η dependence on the left- and right-hand sides of these equations. Take (2.18), for example. Under the parity transformation $\eta \to -\eta$, the nth term of its right-hand side, due to the functional form of $P^m_n(\eta)$, gives a factor of $(-1)^{n-m}$. On the other hand, $\widetilde{M}_{\xi;mn}(\eta, \xi_o)$ and $\widetilde{N}_{\xi;mn}(\eta, \xi_o)$ gives $(-1)^{n-m+1}$ and $(-1)^{n-m}$, respectively. These can be deduced from their expressions in Appendix A and the fact that $S_{mn}(\eta)$ has the same parity property as $P^m_n(\eta)$ [29]. These considerations imply that excitations b_{pmn} with $n-m$ even and $n-m$ odd are decoupled and can be treated separately. If $b_{pmn} \neq 0$ for $n-m$ even, then $B_{pmn'}$, $A^{(N)}_{pmn'}$, and $A^{(M)}_{pm(n'+1)}$ can be nonzero only for $n' = m, m+2, \ldots$. This will be referred to as the case of *even* excitation. If $b_{pmn} \neq 0$ for $n-m$ odd, then $B_{pmn'}$, $A^{(N)}_{pmn'}$, and $A^{(M)}_{pm(n'-1)}$ can be nonzero only for $n' = m+1, m+3, \ldots$. This will be referred to as the case of *odd* excitation.

Note that (2.17), (2.18), and (2.19) must hold for all η on the surface of the spheroid. A common procedure to solve such equations is to expand the left-hand sides, which are regular functions of η, in terms of an infinite series of $P^m_n(\eta)$. This can be accomplished by multiplying both sides of the equations by $P^m_{n'}(\eta)$, $n' = m, m+1, \ldots$, and integrating over η from -1 to 1. Applying this "testing" procedure to (2.18) and (2.19) yields respectively,

$$\mu_r \sum_{n=m}^{\infty} \left[(-1)^p m A^{(M)}_{\tilde{p}mn} I_\xi(n', n) + \frac{1}{c_1} A^{(N)}_{pmn} J_\xi(n', n) \right] = - \left[b_{pmn'} \frac{dP^m_{n'}}{d\xi_o} + B_{pmn'} \frac{dQ^m_{n'}}{d\xi_o} \right] \tag{2.20}$$

and

$$\sum_{n=m}^{\infty} \left[(-1)^{p+1} A^{(M)}_{\tilde{p}mn} I_\phi(n', n) + \frac{m}{c_1} A^{(N)}_{pmn} J_\phi(n', n) \right] = -m \left[b_{pmn'} P^m_{n'}(\xi_o) + B_{pmn'} Q^m_{n'}(\xi_o) \right] \tag{2.21}$$

The integrals $I_\xi(n',n)$, $J_\xi(n',n)$, $I_\phi(n',n)$, $J_\phi(n',n)$ are matrices that couple different angular modes as a result of the non-orthogonality of the angular wavefunctions. They are defined in Appendix A.

For the angular component, the angular dependence of the right-hand side of (2.17) is $dP_n^m/d\eta$. Multiplying the right-hand side with $P_{n'}^m(\eta)$ and integrating would result in a somewhat complicated expression on the right-hand side. We prefer therefore to multiply both sides of (2.17) by the factor $(1-\eta^2)$ before applying the testing procedure. Since

$$(1-\eta^2)\frac{dP_n^m}{d\eta} = \gamma_{1m}(n)P_{n-1}^m(\eta) - \gamma_{2m}(n)P_{n+1}^m(\eta) \tag{2.22}$$

with

$$\gamma_{1m}(n) = \frac{(n+1)(n+m)}{2n+1}, \qquad \gamma_{2m}(n) = \frac{n(n-m+1)}{2n+1} \tag{2.23}$$

we get, from (2.17),

$$\begin{aligned}\sum_{n=m}^{\infty}&\left[(-1)^p m A_{\tilde{p}mn}^{(M)} I_\eta(n',n) + \frac{1}{c_1}A_{pmn}^{(N)} J_\eta(n',n)\right]\\ &= -\gamma_{1m}(n'+1)\left[b_{pm(n'+1)}P_{n'+1}^m(\xi_o) + B_{pm(n'+1)}Q_{n'+1}^m(\xi_o)\right]\\ &\quad +\gamma_{2m}(n'-1)\left[b_{pm(n'-1)}P_{n'-1}^m(\xi_o) + B_{pm(n'-1)}Q_{n'-1}^m(\xi_o)\right]\end{aligned} \tag{2.24}$$

The definitions for $I_\eta(n',n)$ and $J_\eta(n',n)$ can be found in Appendix A.

Eqs. (2.20), (2.21), and (2.24) are the master equations with which the unknown expansion coefficients can be solved. Using (2.20), we can solve for $B_{pmn'}$ in terms of $A_{\tilde{p}mn}^{(M)}$ and $A_{pmn}^{(N)}$:

$$\begin{aligned}B_{pmn'} = -\left[\frac{dQ_{n'}^m}{d\xi_o}\right]^{-1}&\left\{b_{pmn'}\frac{dP_{n'}^m}{d\xi_o}\right.\\ &\left.+\mu_r\sum_{n=m}^{\infty}\left[(-1)^p m A_{\tilde{p}mn}^{(M)} I_\xi(n',n) + \frac{1}{c_1}A_{pmn}^{(N)} J_\xi(n',n)\right]\right\}\end{aligned} \tag{2.25}$$

Incidentally, Eq. (2.25) can be used to obtain the high-frequency limit for $B_{pmn'}$. In this limit, only surface currents exist; therefore, the internal field must vanish. Thus setting $A^{(M)}_{pmn} = A^{(N)}_{pmn} = 0$ in (2.25) gives

$$B_{pmn'} \to - \left[\frac{dQ^m_{n'}}{d\xi_o} \right]^{-1} \frac{dP^m_{n'}}{d\xi_o}\, b_{pmn'} \qquad \text{as } |c_1| \to \infty \tag{2.26}$$

which is only a function of ξ_o (or equivalently elongation ratio $e = b/a$) and the source vector $b_{pmn'}$.

To obtain numerical results, the infinite system of equations must be truncated. Let N_T be the maximum order of coefficients considered, i.e., $A^{(M)}_{\tilde{p}m(n+1)} = A^{(N)}_{pmn} = B_{pmn} = 0$ (even excitation) or $A^{(M)}_{\tilde{p}mn} = A^{(N)}_{pm(n+1)} = B_{pm(n+1)} = 0$ (odd excitation) for $n > N_T$. We choose N_T such that $N_T - m$ is even. Then the total number for each set of coefficients is $L_T = (N_T - m)/2 + 1$.

To cast the system of equations in matrix form, we let, for even excitation,

$$\overline{B} = \left[B_{pmm}, B_{pm(m+2)}, \cdots, B_{pmN_T} \right]^t \tag{2.27}$$

$$\overline{b} = \left[b_{pmm}, b_{pm(m+2)}, \cdots, b_{pmN_T} \right]^t \tag{2.28}$$

be column vectors with length L_T and

$$\begin{aligned} \overline{A} = \Bigg[& \frac{A^{(N)}_{pmm}}{c_1}, \frac{A^{(N)}_{pm(m+2)}}{c_1}, \cdots, \frac{A^{(N)}_{pmN_T}}{c_1}, \\ & (-1)^p A^{(M)}_{\tilde{p}m(m+1)}, (-1)^p A^{(M)}_{\tilde{p}m(m+3)}, \cdots, (-1)^p A^{(M)}_{\tilde{p}m(N_T+1)} \Bigg]^t \end{aligned} \tag{2.29}$$

be a column vector with length $2L_T$. (The superscript t denotes matrix transpose.) Similarly, for odd excitation,

$$\overline{B} = \left[B_{pm(m+1)}, B_{pm(m+3)}, \cdots, B_{pm(N_T+1)} \right]^t \tag{2.30}$$

$$\overline{b} = \left[b_{pm(m+1)}, b_{pm(m+3)}, \cdots, b_{pm(N_T+1)} \right]^t \tag{2.31}$$

$$\overline{A} = \left[\frac{A^{(N)}_{pm(m+1)}}{c_1}, \frac{A^{(N)}_{pm(m+3)}}{c_1}, \cdots, \frac{A^{(N)}_{pm(N_T+1)}}{c_1}, \right.$$
$$\left. (-1)^p A^{(M)}_{\tilde{p}mm}, (-1)^p A^{(M)}_{\tilde{p}m(m+2)}, \cdots, (-1)^p A^{(M)}_{\tilde{p}mN_T} \right]^t \tag{2.32}$$

Then (2.25), (2.24), and (2.21) can be rewritten in matrix notation as

$$\overline{\overline{Z}}_\eta \cdot \overline{A} = \overline{\overline{W}}_\eta \cdot \overline{b} \tag{2.33}$$
$$\overline{\overline{Z}}_\phi \cdot \overline{A} = \overline{\overline{W}}_\phi \cdot \overline{b} \tag{2.34}$$
$$\overline{B} = \overline{\overline{W}}_\xi \cdot \overline{b} - \overline{\overline{Z}}_\xi \cdot \overline{A} \tag{2.35}$$

where $\overline{\overline{Z}}_\beta$ and $\overline{\overline{W}}_\beta$ ($\beta = \eta, \xi, \phi$) are $L_T \times 2L_T$ matrices and $L_T \times L_T$ matrices, respectively. Their expressions can be found in Appendix A. Equations (2.33) and (2.34) provide $2L_T$ linear equations for the $2L_T$ unknowns in $\overline{A}$. After $\overline{A}$ is solved, we use (2.35) to solve $\overline{B}$ and obtain the external secondary field.

It should be remarked that for the special axisymmetric case of $m = 0$ ($p = 0$), it follows from (2.21) that

$$A^{(M)}_{10n} = 0, \quad \text{for } n = 0, 1, 2, \ldots \tag{2.36}$$

Thus we only need to solve for $A^{(N)}_{00n}$ using (2.33). The size of the truncated system of equations in this case is reduced to $L_T \times L_T$ (for either even or odd excitation).

2.2.1 Uniform Primary Field

In many practical applications, the primary field can be taken to be spatially uniform in the region of interest. In this section, we present numerical results for uniform field excitation. Without loss of generality, we let the primary field be in the x-z plane,

$$\overline{H}_o(\overline{r}) = H_o(\hat{z}\cos\zeta + \hat{x}\sin\zeta) \tag{2.37}$$

The corresponding scalar potential in spheroidal coordinates is

$$U_o = \frac{H_o d}{2}\left[-P_1(\eta)P_1(\xi)\,\cos\zeta + P_1^1(\eta)P_1^1(\xi)\cos\phi\,\sin\zeta\right] \tag{2.38}$$

In this case, $b_{pmn'}$ is nonzero only for $n' = 1$ and $p = 0$ while m can be either 0 or 1. The case of $m = 0$ corresponds to a primary field oriented along the z-axis ($\zeta = 0$) and is referred to as the *axial* excitation [20], while the case $m = 1$ corresponds to a primary field oriented along the x-axis ($\zeta = 90^\circ$) and is referred to as the *transverse* excitation. The general case of arbitrary ζ can be obtained by the superposition of these two solutions.

Note that axial excitation is odd ($n' - m$ is odd) while transverse excitation is even ($n' - m$ is even). Thus $B_{00n} \neq 0$ and $B_{01n} \neq 0$ only for $n = 1, 3, \ldots$ under axial excitation and transverse excitation, respectively. The secondary field has the following potential

$$U_\mathrm{s} = \frac{H_o d}{2}\sum_{r=0}^{\infty}\left[B_{00(2r+1)}P_{2r+1}(\eta)Q_{2r+1}(\xi) + B_{01(2r+1)}P_{2r+1}^1(\eta)Q_{2r+1}^1(\xi)\cos\phi\right] \tag{2.39}$$

2.2.2 Far-Field Response

In the far-field, $\xi \to \infty$. In this case, the leading order behavior of $Q_n^m(\xi)$ is [30] (eq. 8.1.3)

$$Q_n^m(\xi) \to (-1)^m \frac{2^n n!(n+m)!}{(2n+1)!}\frac{1}{\xi^{n+1}} \tag{2.40}$$

Thus the leading order contribution to the secondary field comes from the $r = 0$ terms in (2.39). Moreover, as $\xi \to \infty$, the spheroidal coordinate system reduces to the spherical coordinate system: $(d/2)\xi \to r$ and $\eta \to \cos\theta$. Equation (2.39) becomes

$$\begin{aligned} U_\mathrm{s} &\approx H_o\left(\frac{d}{2}\right)^3\frac{1}{r^2}\left[\frac{1}{3}B_{001}P_1(\cos\theta) - \frac{2}{3}B_{011}P_1^1(\sin\theta)\cos\phi\right] \\ &= H_o\left(\frac{\pi d^3}{6}\right)\frac{1}{4\pi r^3}\left[B_{001}z + 2B_{011}x\right] \end{aligned} \tag{2.41}$$

This can be rewritten as

$$U_{\mathrm{s}} = \frac{1}{4\pi r^3}\overline{r} \cdot \overline{M} \tag{2.42}$$

so that we can identify the equivalent induced axial and transverse dipole moments respectively as

$$M_z = H_o\left(\frac{\pi d^3}{6}\right)B_{001} \tag{2.43}$$

$$M_t = H_o\left(\frac{\pi d^3}{3}\right)B_{011} \tag{2.44}$$

When comparing results with different physical parameters, it is convenient to normalize the axial and transverse dipole moments such that they approach one asymptotically at high frequency. The normalized dipole moments m_z and m_t is also known as the magnetic polarizability [20]. It follows from Eqs. (2.26) and (2.38) that

$$m_z = B_{001}N_z \tag{2.45}$$

$$m_t = B_{011}N_t \tag{2.46}$$

where the normalization factors are:

$$N_z = \left[\frac{dP_1}{d\xi_o}\right]^{-1}\frac{dQ_1}{d\xi_o} = \frac{1}{2}\ln\frac{\xi_o+1}{\xi_o-1} - \frac{\xi_o}{\xi_o^2-1} \tag{2.47}$$

$$N_t = -\left[\frac{dP_1^1}{d\xi_o}\right]^{-1}\frac{dQ_1^1}{d\xi_o} = -\frac{1}{2}\ln\frac{\xi_o+1}{\xi_o-1} + \frac{\xi_o^2-2}{\xi_o(\xi_o^2-1)} \tag{2.48}$$

2.3 Numerical Results

To obtain the numerical results presented here, we find it sufficient to truncate the system of equations at $N_T = 70 + m$. The spheroidal wave functions are computed by expanding $S_{mn}(c_1, \eta)$ in an infinite series of associated Legendre functions and

$R^{(1)}_{mn}(c_1, \xi_o)$ in an infinite series of spherical Bessel functions, where the expansion coefficients depend on c_1. More details on the computation of these functions can be found elsewhere [20]. These expansions work well for low to moderate frequencies c_1 [29]. Due to numerical problems associated with calculating the spheroidal wavefunctions at high frequencies, we find that we have to terminate the solution at $|c_1| \approx 30$ (independent of other parameters). Since $c_1 = k_1 d/2$ where d increases with elongation, the termination occurs at a lower k_1 for a more elongated spheroid.

To present broadband results, we shall plot the far-field response as a function of the induction number

$$|k_1|a = \sqrt{\omega\mu_1\sigma_1}\, a \tag{2.49}$$

Holding other parameters fixed, this is equivalent to plotting over the square root of frequency ω.

Figs. 2-2(a) and 2-2(b) show the induced dipole moment as a function of the the induction number for the case of axial and transverse excitations respectively. The relative permeability is $\mu_r = 10$. Both the real part (in-phase component) and the imaginary part (quadrature component) of the dipole moment are shown. To examine shape dependency, the elongation ratio $e = b/a$ is varied from 1 (sphere) to 10 ($\sim$ needle). The behaviors of the induced dipole moment can be understood qualitatively by recognizing the interplay of two physical processes. First, the nonzero magnetic susceptibility of the spheroid causes the spheroid to be magnetized even at zero frequency. Second, the time-varying magnetic field that penetrates the body induces a volume current inside the spheroid. The induced current lags behind the primary field and gives rise to an imaginary part in the induced dipole moment. At very high frequency, the induced current is limited to the surface of the spheroid and is 180° out of phase with the primary field (Lenz's law). Thus the quadrature response approaches zero at both the low and high induction numbers and is largest at some intermediate induction number, while the real part changes its sign as the induction number increases.

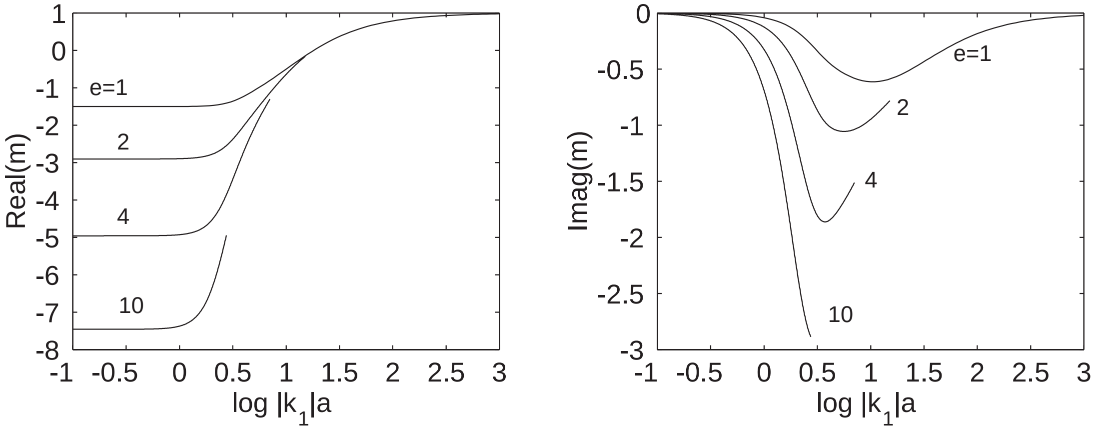

(a) Axial excitation

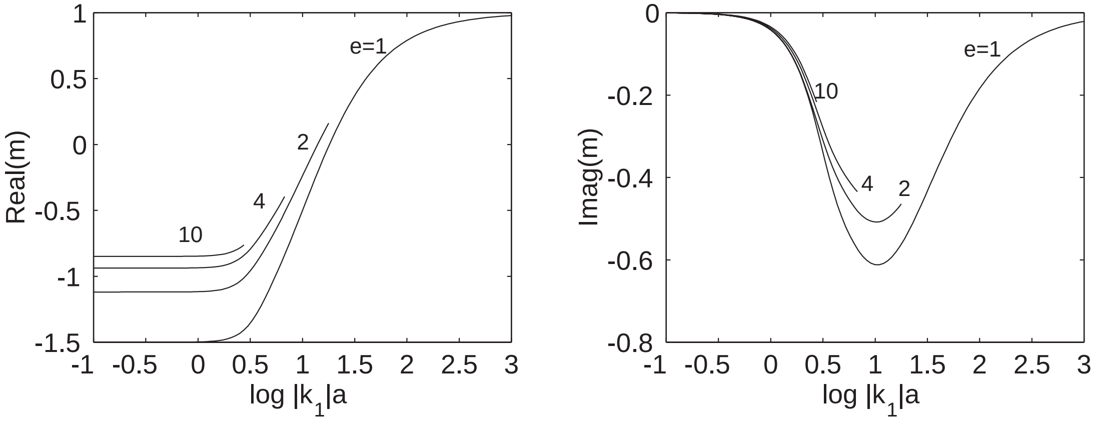

(b) Transverse excitation

Figure 2-2: Normalized induced magnetic dipole moment as a function of induction number for $\mu_r = 10$.

It is important to note that the broadband responses for different elongations are very different depending whether the excitation is axial or transverse. For the axial case, the location of the minimum in the imaginary part clearly shifts to the left as e increases. In contrast, for the transverse case, there is very little change in both the real and imaginary parts as e varies. Thus, an elongated object oriented with its major axis along the primary field will exhibit much more significant low-frequency behaviors.

To investigate the dependence of the solutions on the relative permeability, we show in Figs. 2-3(a) and 2-3(b) the axial and transverse induced dipole moments respectively for the case of $\mu_r = 100$. For a fixed induction number, the product of $\omega\mu_1$ is constant. Thus increasing μ_1 has the equivalent effect of decreasing ω. As a result, the curves for $\mu_r = 100$ appear to shift to the right (higher induction number) when compared to the corresponding solutions for $\mu_r = 10$. This is most evident when looking at the real part of the responses. On the other hand, it is important to recognize that since the relative permeability also comes into the system equations explicitly through the boundary condition (2.15), it could have an additional impact on the solutions besides its effect through the induction number. Indeed, numerical results for finite-length cylinders indicate that when the aspect ratio is large enough, the maximum of the quadrature response under axial excitation actually shifts to the left (lower induction number) when μ_r increases [31]. This, however, cannot be confirmed here due to the early termination of the responses at high elongation ratios.

2.4 Small Penetration-depth Approximation (SPA)

The formulation presented in Section 2.2 is formally exact and applicable for any elongation and frequency within the quasi-magnetostatic assumptions. Nevertheless, as we have seen in Section 2.3, numerical results for the solution require the evaluation

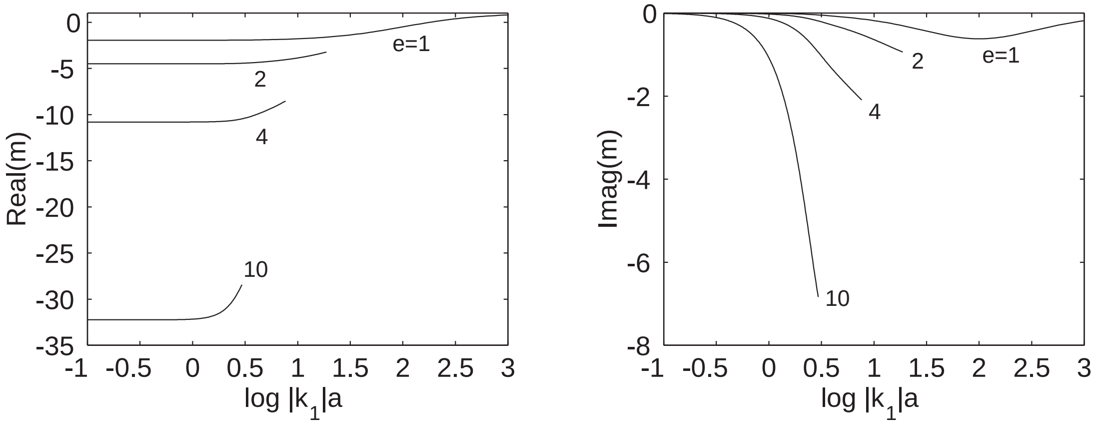

(a) Axial excitation.

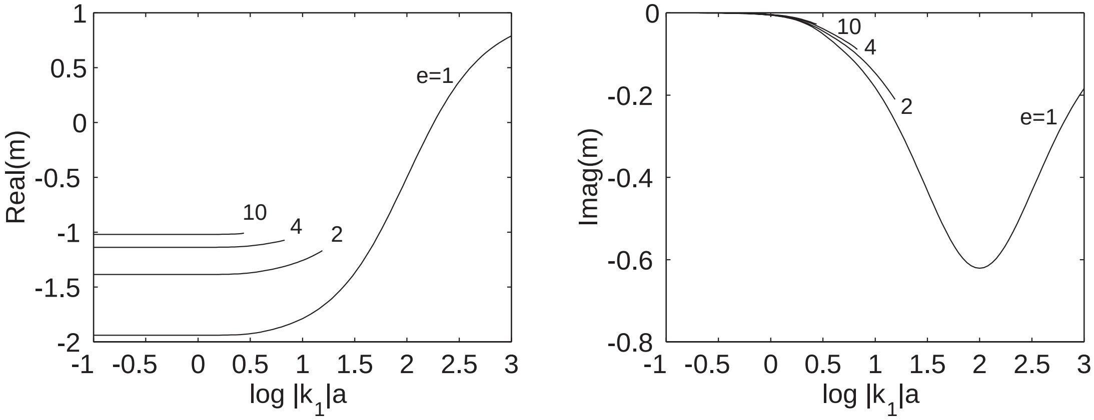

(b) Transverse excitation.

Figure 2-3: Normalized induced magnetic dipole moment as a function of induction number for $\mu_r = 100$.

of the radial and angular spheroidal wavefunctions, which are only readily computed for small and moderate values of frequency parameter c_1. It is therefore desirable to establish an alternative formulation that avoids any reference to the spheroidal wavefunctions and that would be applicable at least for high-frequencies.

We observe that at high frequency, the internal fields are only nonzero in a thin layer beneath the surface. Thus the internal field must decay rapidly near the surface. This implies that terms with the normal derivative $\partial/\partial\xi$ would be dominant near the surface. Under this small penetration-depth approximation (SPA) condition, the vector wave equation (2.1) implies that just below the surface,

$$k_1^2 \tilde{H}_{1\eta} \approx -\frac{h_\eta}{h_\xi h_\phi}\frac{\partial}{\partial\xi}\left[\frac{h_\phi}{h_\eta h_\xi}\frac{\partial \tilde{H}_{1\eta}}{\partial\xi}\right] \tag{2.50}$$

$$k_1^2 \tilde{H}_{1\phi} \approx -\frac{h_\phi}{h_\eta h_\xi}\frac{\partial}{\partial\xi}\left[\frac{h_\eta}{h_\xi h_\phi}\frac{\partial \tilde{H}_{1\phi}}{\partial\xi}\right] \tag{2.51}$$

where $\tilde{H}_\alpha = h_\alpha H_\alpha$ for $\alpha = \eta, \xi, \phi$, with h_α being the metric coefficients for the prolate spheroidal coordinates [See Appendix A]. Thus the tangential components of the magnetic field $\tilde{H}_\eta$ and $\tilde{H}_\phi$ become decoupled near the surface. Simplifying (2.50) and (2.51), we obtain

$$k_1^2 \tilde{H}_{1\eta} \approx -\frac{1}{h_\xi^2}\frac{\partial^2 \tilde{H}_{1\eta}}{\partial\xi^2} - \frac{h_\eta}{h_\xi h_\phi}\frac{\partial}{\partial\xi}\left[\frac{h_\phi}{h_\eta h_\xi}\right]\frac{\partial \tilde{H}_{1\eta}}{\partial\xi} \tag{2.52}$$

$$k_1^2 \tilde{H}_{1\phi} \approx -\frac{1}{h_\xi^2}\frac{\partial^2 \tilde{H}_{1\phi}}{\partial\xi^2} \tag{2.53}$$

Eq. (2.53) is satisfied at $\xi = \xi_o$ by letting

$$\tilde{H}_{1\phi}(\eta, \xi, \phi) = \tilde{H}_{1\phi}(\eta, \xi_o, \phi)\, e^{-ik_1 h_\xi(\eta,\xi_o)(\xi-\xi_o)} \tag{2.54}$$

where the sign in the exponential has been chosen so that the field decays inward ($\xi < \xi_o$), given that $\mathrm{Im}\{k_1\} > 0$.

To solve Eq. (2.52), we let

$$\tilde{H}_{1\eta}(\eta,\xi,\phi) = \tilde{H}_{1\eta}(\eta,\xi_o,\phi)\; e^{-ik_1 h_\xi(\eta,\xi_o) f(\eta)(\xi-\xi_o)} \tag{2.55}$$

Then Eq. (2.52) at $\xi = \xi_o$ gives

$$0 = f^2 + \frac{iq}{c_1} f - 1 \tag{2.56}$$

where

$$\begin{aligned} q &= \frac{d}{2}\frac{h_\eta(\eta,\xi_o)}{h_\phi(\eta,\xi_o)}\left[\frac{\partial}{\partial\xi}\frac{h_\phi}{h_\eta h_\xi}\right]_{\xi=\xi_o} \\ &= \frac{2\xi_o}{(\xi_o^2-\eta^2)^{1/2}(\xi_o^2-1)^{1/2}}\left[1-\frac{\xi_o^2-1}{\xi_o^2-\eta^2}\right] \end{aligned} \tag{2.57}$$

Note that because of the first term in the above equation, $q \to \infty$ as $\xi_o \to 1$. Thus the middle term in (2.56) should in general be retained even when $|c_1| \gg 1$ but finite. From (2.56), the two possible solutions for f are

$$f = \pm\sqrt{1-\frac{q^2}{4c_1^2}} - \frac{iq}{2c_1} \tag{2.58}$$

Thus

$$\tilde{H}_{1\eta}(\eta,\xi,\phi) = \tilde{H}_{1\eta}(\eta,\xi_o,\phi)\exp\left[-ik_1 h_\xi(\eta,\xi_o)\left(\sqrt{1-\frac{q^2}{4c_1^2}}-\frac{iq}{2c_1}\right)(\xi-\xi_o)\right] \tag{2.59}$$

where the plus sign for f has been chosen so that the field decays inward.

Using (2.1) together with the SPA condition, the normal component of the internal field on the surface $\xi = \xi_o$ can be found from the tangential components by

$$\tilde{H}_{1\xi} = \frac{1}{ik_1}\frac{h_\xi}{h_\eta h_\phi}\left[\frac{h_\eta}{h_\phi}\frac{\partial \tilde{H}_{1\phi}}{\partial\phi} + \frac{\partial}{\partial\eta}\left(\frac{h_\phi}{h_\eta} f \tilde{H}_{1\eta}\right)\right] \tag{2.60}$$

Making use of the boundary conditions (2.13)–(2.15) at $\xi = \xi_o$, we obtain

$$\frac{1}{\mu_r}\tilde{H}_{2\xi} = \frac{1}{ik_1}\frac{h_\xi}{h_\eta h_\phi}\left[\frac{h_\eta}{h_\phi}\frac{\partial \tilde{H}_{2\phi}}{\partial\phi} + \frac{\partial}{\partial\eta}\left(\frac{h_\phi}{h_\eta} f \tilde{H}_{2\eta}\right)\right] \tag{2.61}$$

which refers only to the external fields. In (2.60) and (2.61), it is understood that the metric coefficients are to be evaluated at $\xi = \xi_o$.

The field expansions for $\tilde{H}_{2\alpha}$ can be obtained from Eqs. (2.11) and (2.9). Putting these field expansions into (2.61), we obtain

$$\begin{aligned} &\frac{ic_1}{\mu_r}\sum_{n=m}^{\infty} B_{pmn}\frac{dQ_n^m}{d\xi_o}P_n^m(\eta) - \frac{1}{\xi_o^2-1}\sum_{n=m}^{\infty} B_{pmn}Q_n^m(\xi_o)E_n^m(\eta;\xi_o,c_1) \\ &= -\frac{ic_1}{\mu_r}\sum_{n=m}^{\infty} b_{pmn}\frac{dP_n^m}{d\xi_o}P_n^m(\eta) + \frac{1}{\xi_o^2-1}\sum_{n=m}^{\infty} b_{pmn}P_n^m(\xi_o)E_n^m(\eta;\xi_o,c_1) \end{aligned} \tag{2.62}$$

where

$$\begin{aligned} E_n^m(\eta;\xi_o,c_1) &= -\frac{h_\eta}{h_\phi}\, m^2 P_n^m(\eta) + \frac{\partial}{\partial\eta}\left(\frac{h_\phi}{h_\eta} f \frac{dP_n^m}{d\eta}\right) \\ &= -\frac{(\xi_o^2-\eta^2)^{1/2}}{(\xi_o^2-1)^{1/2}}\,\frac{m^2}{1-\eta^2}P_n^m(\eta) + (\xi_o^2-1)^{1/2}\frac{\partial}{\partial\eta}\left(\frac{(1-\eta^2)f}{(\xi_o^2-\eta^2)^{1/2}}\frac{dP_n^m}{d\eta}\right) \end{aligned} \tag{2.63}$$

Now multiply both sides of Eq. (2.62) by $P_{n'}^m(\eta)$ and integrate over η. The final system of equations for B_{pmn} is

$$\begin{aligned} &\frac{ic_1}{\mu_r}B_{pmn'}\frac{dQ_{n'}^m}{d\xi_o} - \frac{1}{\xi_o^2-1}\sum_{n=m}^{\infty} B_{pmn}Q_n^m(\xi_o)\Gamma_{n'n}^m(\xi_o,c_1) \\ &= -\frac{ic_1}{\mu_r}b_{pmn'}\frac{dP_{n'}^m}{d\xi_o} + \frac{1}{\xi_o^2-1}\sum_{n=m}^{\infty} b_{pmn}P_n^m(\xi_o)\Gamma_{n'n}^m(\xi_o,c_1) \end{aligned} \tag{2.64}$$

with

$$\Gamma_{n'n}^m(\xi_o,c_1) = \frac{2n'+1}{2}\,\frac{(n'-m)!}{(n'+m)!}\int_{-1}^{1} d\eta\, P_{n'}^m(\eta)E_n^m(\eta;\xi_o,c_1) \tag{2.65}$$

At very high frequency, the terms with the c_1 coefficient dominate, and we get the limit

$$B_{pmn'} = -\left[\frac{dQ_{n'}^{m}}{d\xi_o}\right]^{-1} \frac{dP_{n'}^{m}}{d\xi_o}\, b_{pmn'} \tag{2.66}$$

which is identical to (2.26).

The SPA approach developed here is based on similar thin-skin physical arguments employed in the high-frequency approximation used in [20] for axial excitation. The latter approach assumes an expression for the azimuthal component of the *electric* field much like Eq. (2.54) for the magnetic field. The resulting system of equations is different for the two approaches. However, where these two approaches are valid, the two solutions should be close to each other. The present approach also bears some similarity to the numerical thin skin approximation (TSA) approach used in [21], where the approximation ansatz is used for the *normal* component of the magnetic field — as opposed to the *tangential* components that are found here.

Numerical results for B_{pmn} can easily be obtained by truncating the infinite system of equations and evaluating the integrals in $\Gamma_{n'n}^{m}(\xi_o, c_1)$ in (2.65) using Gaussian quadrature. Using (2.64), we compute the solutions corresponding to the uniform primary excitation as in Sec. 2.3. The strength of this new system of equations is that there is no numerical limitation in frequency and elongation. Figs. 2-4(a) and 2-4(b) show the normalized induced dipole moment as a function of induction number under axial and transverse excitations, respectively. The relative permeability is 10. The exact solutions are also displayed for comparison. It can be seen that, based on the cases of $e = 1$ and 2, the results from SPA match well with those from the exact solution above an induction number of approximately 10.

Figs. 2-5(a) and 2-5(b) show the corresponding results for $\mu_r = 100$. In this case, the SPA results are not only accurate at high induction numbers as expected, but they provide a reasonable approximation at low induction numbers as well. This suggests that for spheroids with large μ_r, the SPA of (2.64) is capable of providing reasonably accurate, broadband EMI responses for a wide range of elongations. To see this more clearly, we show in Fig. 2-6 for elongation ratio of $e = 3$ but with the

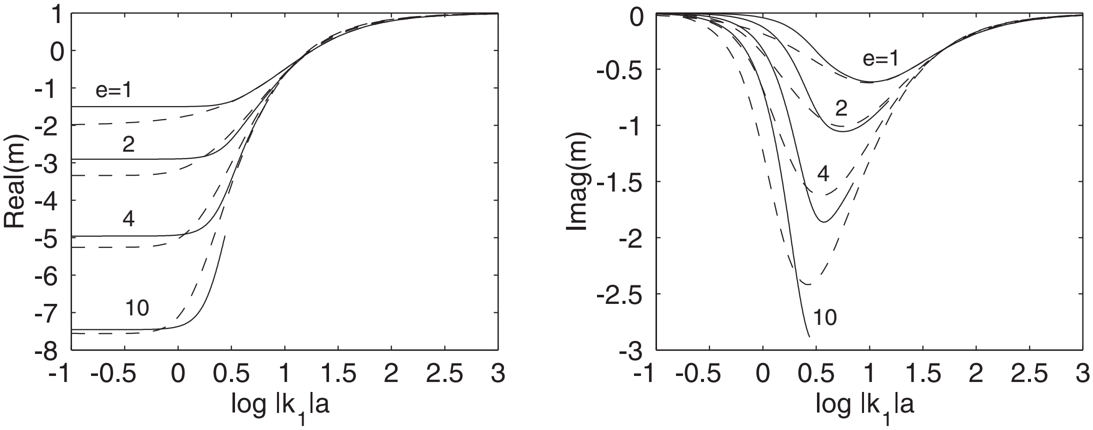

(a) Axial excitation.

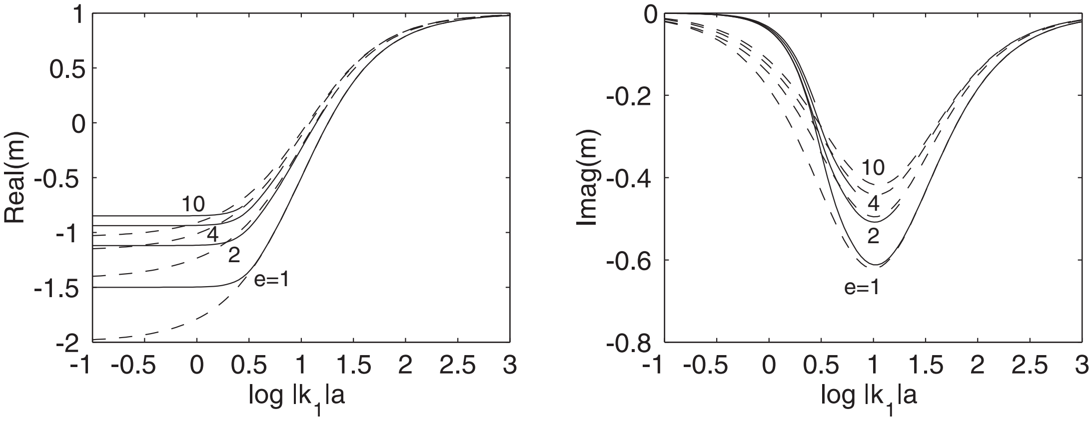

(b) Transverse excitation.

Figure 2-4: Normalized induced magnetic dipole moment as a function of induction number for $\mu_r = 10$. Dashed line: SPA. Solid line: Exact solution.

relative permeability of the spheroid varying from $\mu_r = 5$ to $\mu_r = 500$. For $\mu_r = 5$, there is considerable difference between the exact and SPA results at low induction numbers. This is to be expected since SPA is developed to handle the higher frequency regime. However, it can be seen that as μ_r increases, the exact and SPA results begin to merge. For $\mu_r = 500$, the SPA results give excellent agreement with the exact results across the whole range of induction numbers.

2.5 SPA for Oblate Spheroids

In view of the relative simplicity of the SPA and its success for prolate spheroids with large permeability, we now extend the SPA to the case of an oblate spheroid (Fig. 2-7). A parallel development can be made using the oblate spheroidal coordinates. However, a simple and quick way to achieve the same is to apply the following transformation to the equations for prolate spheroids [29]:

$$\begin{cases} \xi_o \to i\xi_o \\ c_1 \to -ic_1 \text{ (or } d \to -id) \end{cases} \tag{2.67}$$

Applying the transformation (2.67) to Eq. (2.64), we obtain

$$\begin{aligned} &-\frac{c_1}{\mu_r} B_{pmn'} \frac{dQ_{n'}^m}{d\xi}(i\xi_o) - \frac{1}{\xi_o^2+1} \sum_{n=m}^{\infty} B_{pmn} Q_n^m(i\xi_o) \Gamma_{n'n}^m(i\xi_o, -ic_1) \\ &= \frac{c_1}{\mu_r} b_{pmn'} \frac{dP_{n'}^m}{d\xi}(i\xi_o) + \frac{1}{\xi_o^2+1} \sum_{n=m}^{\infty} b_{pmn} P_n^m(i\xi_o) \Gamma_{n'n}^m(i\xi_o, -ic_1) \end{aligned} \tag{2.68}$$

with

$$\Gamma_{n'n}^m(i\xi_o, -ic_1) = \frac{2n'+1}{2} \frac{(n'-m)!}{(n'+m)!} \int_{-1}^{1} d\eta P_{n'}^m(\eta) E_n^m(\eta; i\xi_o, -ic_1) \tag{2.69}$$

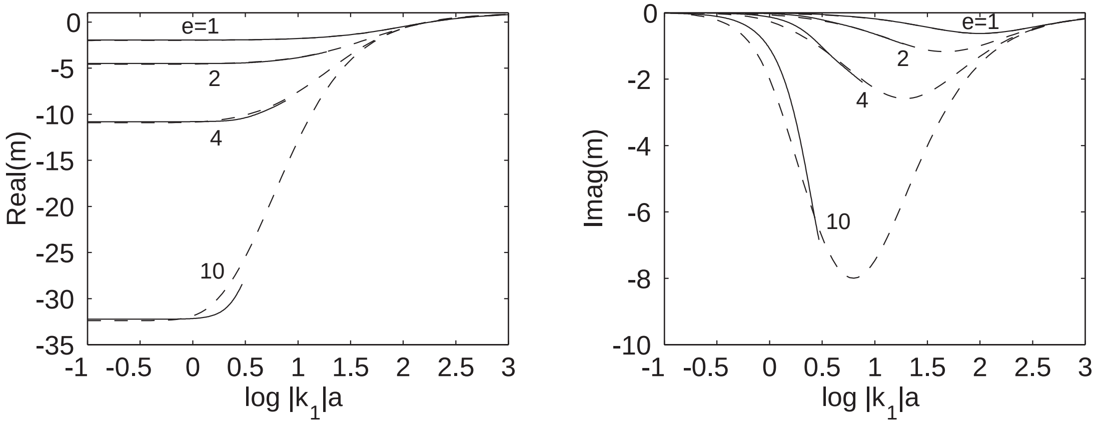

(a) Axial excitation.

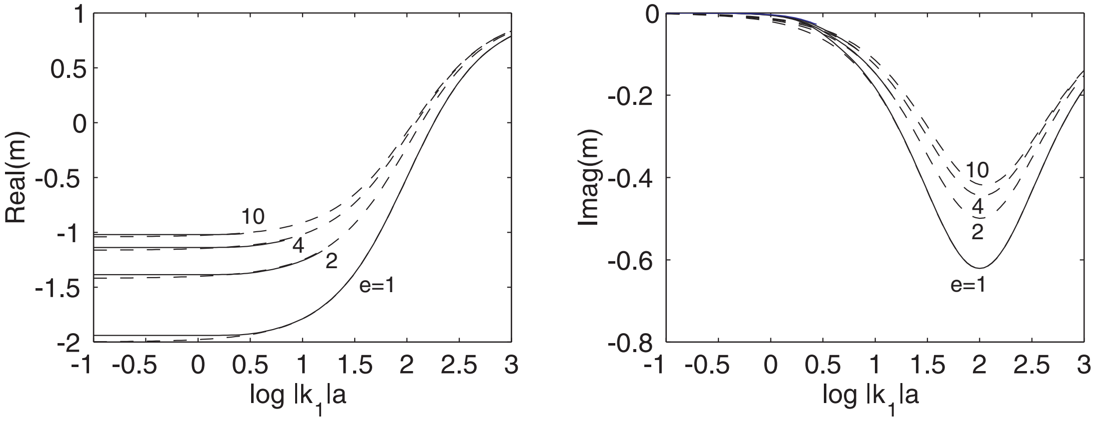

(b) Transverse excitation.

Figure 2-5: Normalized induced magnetic dipole moment as a function of induction number for $\mu_r = 100$. Dashed line: SPA. Solid line: Exact solution.

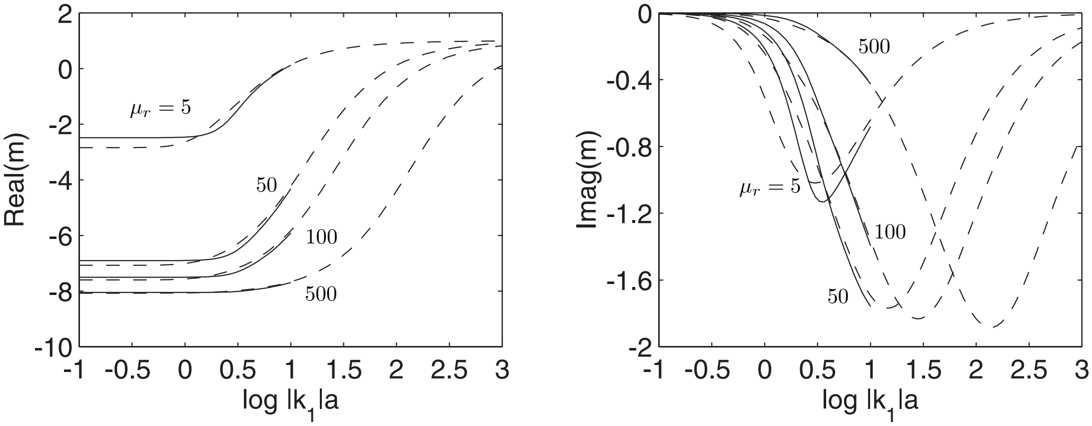

(a) Axial excitation.

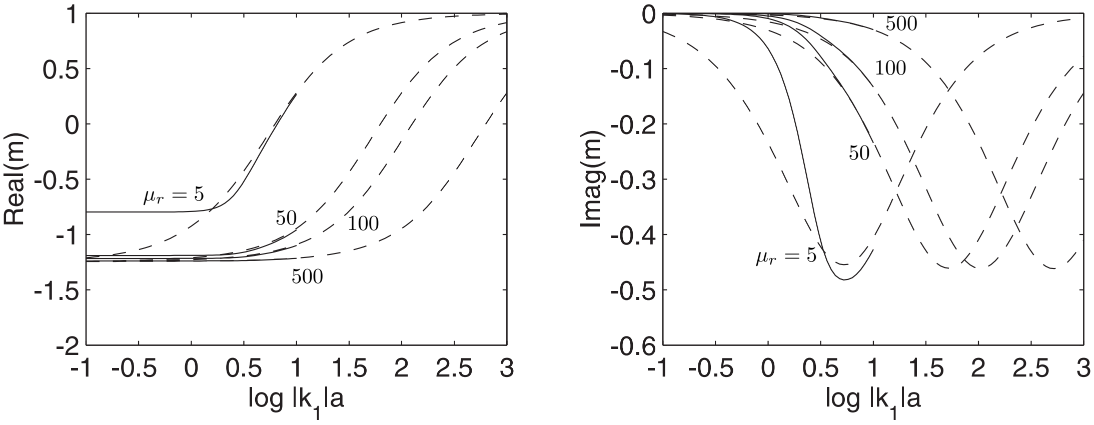

(b) Transverse excitation.

Figure 2-6: Normalized induced magnetic dipole moment as a function of induction number for $e = 3$. Dashed line: SPA. Solid line: Exact solution.

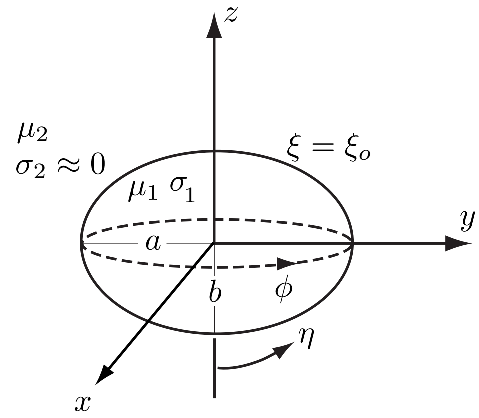

Figure 2-7: A conducting and permeable oblate spheroid. The oblate spheroidal coordinate system is specified by (η, ξ, ϕ) with $-1 \leq \eta \leq 1$, $0 \leq \xi < \infty$, and $0 \leq \phi < 2\pi$. The surface of the spheroid is given by $\xi = \xi_o = b/\sqrt{a^2 - b^2}$.

Applying the transformation (2.67) to the field expansions of (2.9) and (2.11) gives respectively

$$U_o(\overline{r}) = \frac{H_o d}{2} \sum_{m=0}^{\infty} \sum_{n=m}^{\infty} \sum_{p=0}^{1} (-ib_{pmn}) \Phi^{(1)}_{pmn}(\eta, i\xi, \phi) \tag{2.70}$$

$$U_{\mathrm{s}}(\overline{r}) = \frac{H_o d}{2} \sum_{m=0}^{\infty} \sum_{n=m}^{\infty} \sum_{p=0}^{1} (-iB_{pmn}) \Phi_{pmn}(\eta, i\xi, \phi) \tag{2.71}$$

For the uniform primary field of (2.37), we have

$$U_o(\overline{r}) = \frac{H_o d}{2} \left[iP_1(\eta) P_1(i\xi)(\cos\zeta) - iP_1^1(\eta) P_1^1(i\xi) \cos\phi (\sin\zeta) \right] \tag{2.72}$$

in oblate spheroidal coordinates. The far-field response can be obtained by taking the limit $\xi \to \infty$. The leading order contribution is

$$U_{\mathrm{s}}(\overline{r}) = \frac{H_o}{4\pi r^3} \left(\frac{\pi d^3}{6} \right) \left[iB_{001} z + i2B_{011} x \right] \tag{2.73}$$

This gives the equivalent axial and transverse dipole moments of

$$M_z = H_o \left(\frac{\pi d^3}{6}\right) iB_{001} \tag{2.74}$$

$$M_t = H_o \left(\frac{\pi d^3}{3}\right) iB_{011} \tag{2.75}$$

To obtain the normalized dipole moments as in (2.45) and (2.46), we first solve (2.68) in the high-frequency limit:

$$B_{pmn} \to -\frac{dP_n^m}{d\xi}(i\xi_o)\left[\frac{dQ_n^m}{d\xi}(i\xi_o)\right]^{-1} b_{pmn}, \quad \text{as } |c_1| \to \infty \tag{2.76}$$

Thus the normalization factors for the oblate case are

$$N_z = \left[\frac{dP_1}{d\xi}(i\xi_o)\right]^{-1} \frac{dQ_1}{d\xi}(i\xi_o) = i\left[-\cot^{-1}\xi_o + \frac{\xi_o}{\xi_o^2+1}\right] \tag{2.77}$$

$$N_t = -\left[\frac{dP_1^1}{d\xi}(i\xi_o)\right]^{-1} \frac{dQ_1^1}{d\xi}(i\xi_o) = i\left[\cot^{-1}\xi_o - \frac{\xi_o^2+2}{\xi_o(\xi_o^2+1)}\right] \tag{2.78}$$

In Figs. 2-8(a) and 2-8(b), we show the normalized induced dipole moment as a function of the induction number for an oblate spheroid under axial and transverse excitation, respectively. The relative permeability is 100 so that the SPA should give fairly accurate broadband results. The flatness ratio a/b is varied from 1 (sphere) to 10 ($\sim$ flat disc). It is interesting to note that as a/b increases, the peak of the axial response shifts to a higher induction number, while the frequency characteristics of the transverse response show very little change. This is consistent with the trend observed for prolate spheroids (cf. Fig. 2-3). This suggests that the broadband EMI response of a nonspherical object is quite sensitive to its characteristic dimension along the primary field.

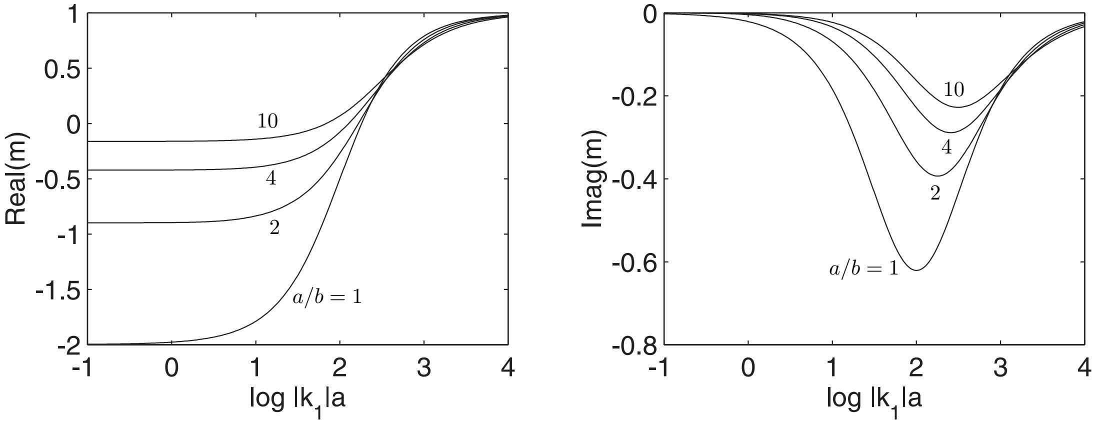

(a) Axial excitation.

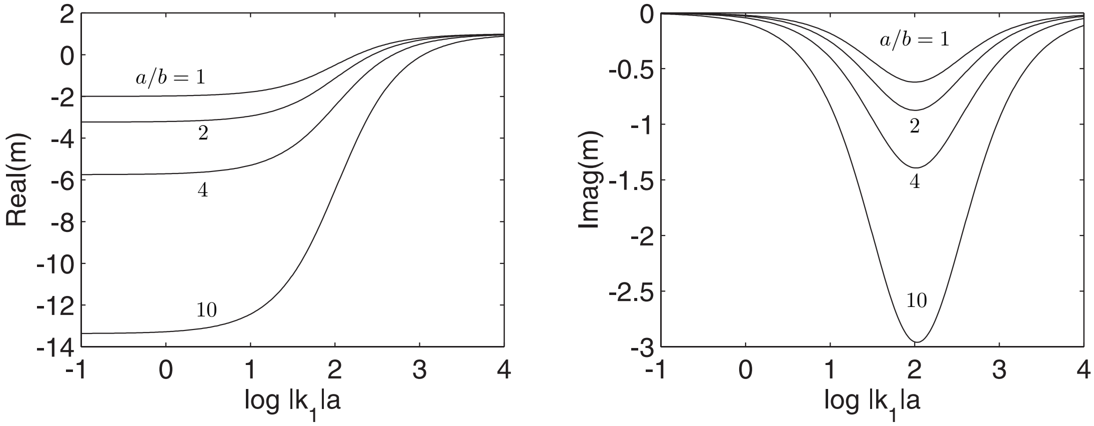

(b) Transverse excitation.

Figure 2-8: Normalized induced magnetic dipole moment as a function of induction number $|k_1|a$ for an oblate spheroid. Relative permeability is $\mu_r = 100$. SPA results only.

2.6 EMI Response from a Collection of Spheroids

In locations where landmines and UXO are found, significant amount of clutter could be present in the form of wires and shrapnel from exploded shells. It is also possible that multiple UXO are found next to each other. In this section, we investigate the EMI response from a collection of spheroids.

Consider the case where N spheroids are present with centers located at $\overline{r}_j$ and semiaxes a_j and b_j, with $j = 1, 2, \ldots, N$. The orientation of the spheroid j is specified by the Euler angles $\{\alpha_j, \beta_j, \gamma_j\}$ with respect to the laboratory frame ([4], pp. 81–83). Its permeability and conductivity are μ_{1j} and σ_{1j}, respectively. Then the dimensionless frequency parameter for spheroid j is $c_{1j} = k_{1j} d_j / 2$ with $k_{1j}^2 = i\omega\mu_{1j}\sigma_{1j}$. The focal length is $d_j = 2\sqrt{b_j - a_j}$ for a prolate spheroid or $d_j = 2\sqrt{a_j - b_j}$ for an oblate spheroid.

Suppose that the primary field is uniform over the entire region where the spheroids are present and is given by

$$\overline{H}_o(\overline{r}) = H_o \hat{z} \tag{2.79}$$

In the body (principal) coordinates of spheroid j, the primary field can be written as

$$\overline{H}_o(\overline{r}) = H_o \left[\hat{z}_{bj} \cos\beta_j + \hat{x}_{bj} \sin\beta_j \cos\alpha_j + \hat{y}_{bj} \sin\beta_j \sin\alpha_j \right] \tag{2.80}$$

where $\hat{x}_{bj}$, $\hat{y}_{bj}$, and $\hat{z}_{bj}$ are the unit vectors in the body coordinates of spheroid j.

If we assume that the interactions between the spheroids are negligible, the responses from the individual spheroids are additive [32]. From (2.42), the total far-field response can be written as

$$U_{\mathrm{s}}(\overline{r}) = \sum_{j=1}^{N} \frac{1}{4\pi |\overline{r} - \overline{r}_j|^3} \overline{M}^{(j)} \cdot (\overline{r} - \overline{r}_j) \approx \frac{1}{4\pi r^3} \overline{M}^{(\mathrm{tot})} \cdot \overline{r} \tag{2.81}$$

where

$$\begin{aligned}\overline{M}^{(\text{tot})} &= \sum_{j=1}^{N} \overline{M}^{(j)} \\ &= \sum_{j=1}^{N} \left[M_z^{(j)} \cos\beta_j \hat{z}_{bj} + M_t^{(j)} (\sin\beta_j \cos\alpha_j \hat{x}_{bj} + \sin\beta_j \sin\alpha_j \hat{y}_{bj}) \right] \end{aligned} \tag{2.82}$$

is the equivalent induced dipole moment from all the spheroids. Note that $M_z^{(j)}$ and $M_t^{(j)}$ are respectively the axial and transverse responses from spheroid j in isolation. They are independent of the Euler angles but do depend on the semiaxes a_j and b_j.

Suppose that the spheroids are uniformly distributed in α_j and γ_j. Then the orientation distribution function is

$$p(\alpha_j, \beta_j, \gamma_j) = p(\beta_j) \frac{1}{4\pi^2} \tag{2.83}$$

subject to the following normalization condition

$$\int_0^{2\pi} d\alpha_j \int_0^{\pi} d\beta_j \int_0^{2\pi} d\gamma_j \; p(\alpha_j, \beta_j, \gamma_j) = 1 \tag{2.84}$$

The orientation-averaged total dipole moment is

$$\langle \overline{M}^{(\text{tot})} \rangle = \hat{z} \left[M_z^{(\text{tot})} \langle \cos^2\beta \rangle + M_t^{(\text{tot})} \langle \sin^2\beta \rangle \right] \tag{2.85}$$

where

$$M_z^{(\text{tot})} = \sum_{j=1}^{N} M_z^{(j)} \tag{2.86}$$

$$M_t^{(\text{tot})} = \sum_{j=1}^{N} M_t^{(j)} \tag{2.87}$$

$$\langle \cos^2\beta \rangle = \int_0^{\pi} d\beta \; p(\beta) \cos^2\beta \tag{2.88}$$

$$\langle \sin^2\beta \rangle = 1 - \langle \cos^2\beta \rangle \tag{2.89}$$

If we consider further the simple case where the orientation distribution is uniform in solid angle, we have $p(\beta) = \frac{1}{2}\sin\beta$ and $\langle\cos^2\beta\rangle = 1/3$ and $\langle\sin^2\beta\rangle = 2/3$ so that

$$\langle\overline{M}^{(\mathrm{tot})}\rangle = \hat{z}\left[\frac{1}{3}M_z^{(\mathrm{tot})} + \frac{2}{3}M_t^{(\mathrm{tot})}\right] \tag{2.90}$$

Since the high-frequency limit is known, we can define a normalized total induced dipole moment as

$$\langle m_z^{(\mathrm{tot})}\rangle = \left[\sum_{j=1}^{N} d_j^3\left(\frac{1}{N_{zj}} + \frac{4}{N_{tj}}\right)\right]^{-1}\sum_{j=1}^{N} d_j^3\left(\frac{m_z^{(j)}}{N_{zj}} + \frac{4m_t^{(j)}}{N_{tj}}\right) \tag{2.91}$$

where $m_z^{(j)}$ and $m_t^{(j)}$ represent the normalized responses from a single spheroid with semiaxes $a = a_j$ and $b = b_j$. Similarly, N_{zj} and N_{tj} are the normalization factors for single spheroid responses with ξ_o replaced by ξ_{oj}.

Using the formulation developed, we provide numerical illustrations for the following two simple cases. We assume that the spheroids have identical conductivity σ_1 and permeability $\mu_1 = 100$. At this value of μ_r, the SPA is applicable over a broad frequency band.

Case (a): The spheroids have identical sizes but are randomly oriented. In this case the normalized dipole moment is

$$\langle m_z^{(\mathrm{tot})}\rangle = \left[\frac{1}{N_z} + \frac{4}{N_t}\right]^{-1}\left(\frac{m_z}{N_z} + \frac{4m_t}{N_t}\right) \tag{2.92}$$

Fig. 2-9 and shows the normalized dipole moment as a function of induction number from such a collection of prolate and oblate spheroids. For prolate spheroids, the axial response dominates in magnitude. The orientation-averaged response therefore resembles more the axial response from a single prolate spheroid. For oblate spheroids, the transverse response dominates in magnitude, and the average response resembles more the transverse response from a single oblate spheroid.

Case (b): One large object (the *target*) is surrounded by many randomly ori-

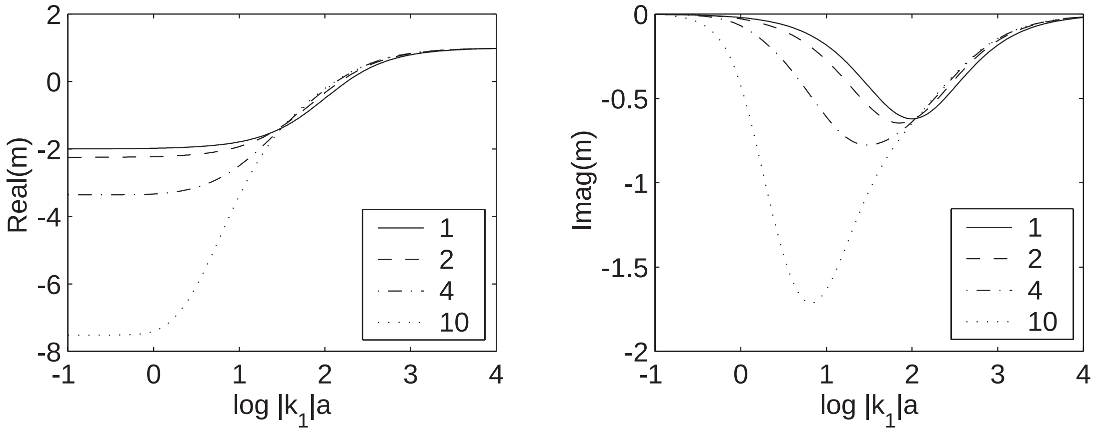

(a) Prolate.

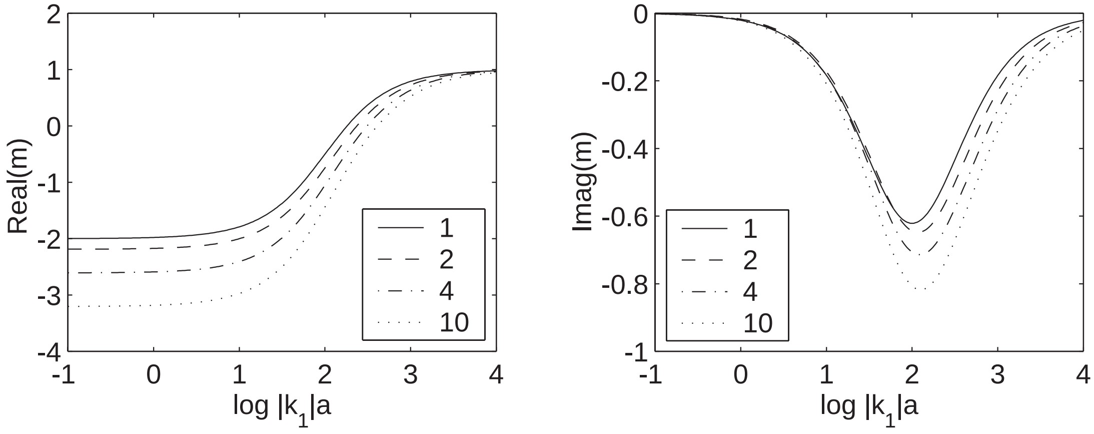

(b) Oblate.

Figure 2-9: Normalized induced magnetic dipole moment from a randomly oriented distribution of prolate and oblate spheroids as a function of induction number $|k_1|a$. $\mu_r = 100$; $b/a = 1, 2, 4, 10$ for prolate spheroid and $a/b = 1, 2, 4, 10$ for oblate spheroid as labeled.

Parameters	Large spheroid	Small spheroid
N	1	5000
a (cm)	10	0.2
b (cm)	20	2
μ_r	100	100
σ_1 (S/m)	10^7	10^7

Table 2.1: Parameters used for the target and clutter example.

ented small elongated objects (the *clutter*). The large object is taken to be a prolate spheroid with $e = 2$. The small objects are also prolate spheroids but with $e = 10$. The parameters are shown in Table 2.1. Note that with these parameters, the small objects occupy a volume which is only 20% of the volume of the large object. The background permeability is taken to be that of free space: $\mu_2 = \mu_o = 4\pi \times 10^{-7}$ henry/m. Let N_s be the number of small spheroids. Then the total response is

$$\overline{M}^{(\mathrm{tot})} = \overline{M} + N_s \langle \overline{M}^{(s)} \rangle \tag{2.93}$$

where $\overline{M}$ is the response from the large object while $N_s \langle \overline{M}^{(s)} \rangle$ is the orientation-averaged response from the small objects. The latter quantity can be obtained from (2.90). The orientation of the large object is chosen to be either axial or transverse to the primary field. Fig. 2-10 shows the total induced dipole moment from such a collection of spheroids as a function of frequency in Hertz. Note that the dipole moments are not normalized in this case. For comparison, the responses from the large spheroid and the small spheroids alone are also shown. The large elongation ratio of the small spheroids produce a large real-part response that distorts the response from the large spheroid. The total real-part response now crosses zero at a much higher frequency (by about one order of magnitude). Similarly, the total imaginary part has a maximum that shifts to higher frequency. Thus the presence of the small spheroids, if not accounted for properly, could lead us to conclude that the target spheroid is smaller and/or more elongated than it should be.

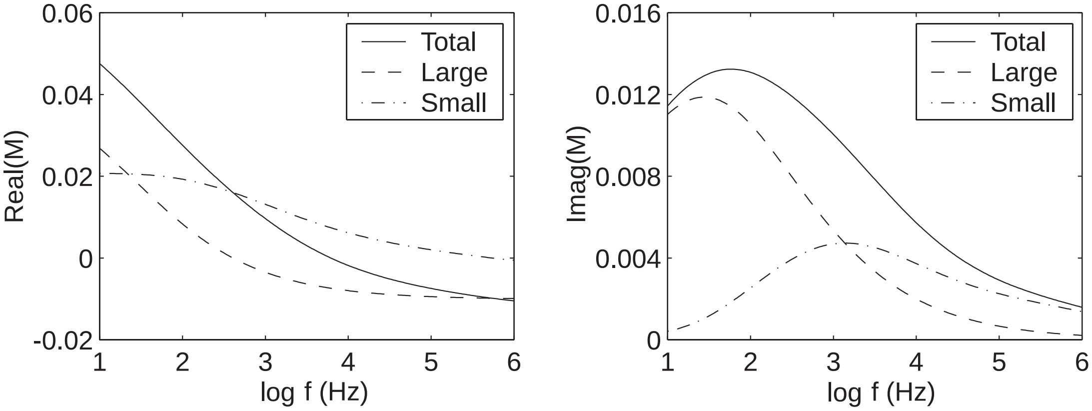

(a) Axial excitation.

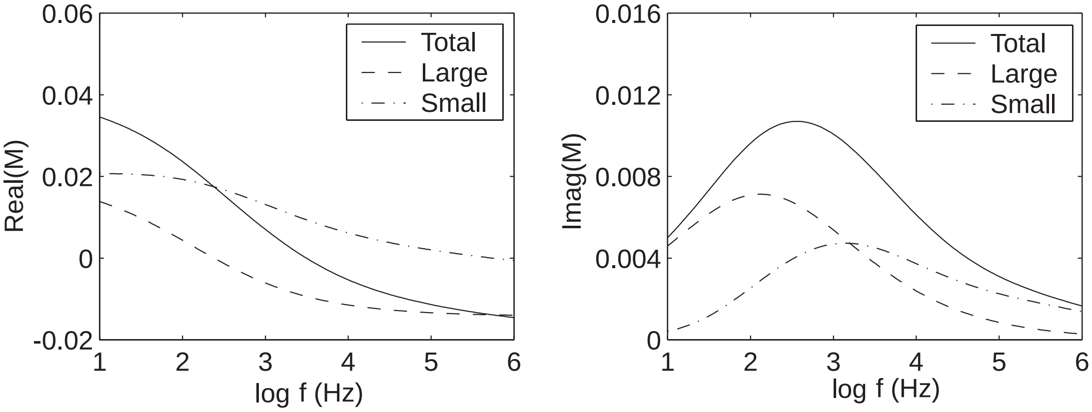

(b) Transverse excitation.

Figure 2-10: Induced magnetic dipole moment from a large prolate spheroid embedded in randomly oriented small prolate spheroids. The parameters for these results are shown in Table 2.1. Also $\mu_2 = \mu_o$ (free-space permeability) and $H_o = 1$.

2.7 Conclusions

We have obtained the quasi-magnetostatic solution for a conducting and permeable prolate spheroid under arbitrary excitation using the separation of variables method in prolate spheroidal coordinates. Since the surrounding medium is assumed to be poorly conducting, we consider a "hybrid" problem where the full-wave expansion of the internal field is matched with the static expansion of the external field. The vector spheroidal wavefunctions provide a basis for the internal field expansion. We derive a system of equations from which the unknown expansion coefficients can be solved. Numerical results are presented for the case of uniform primary excitation. It is shown that the frequency response of the induced dipole moment is notably different depending on the orientation of the spheroid with respect to the primary field. It is also sensitive to the permeability of the spheroid relative to the background.

Due to numerical problems associated with the computation of the spheroidal wavefunctions at high frequencies, the exact solutions are available only up to a certain cutoff induction number, which decreases as the elongation ratio increases. Since a broadband response is desired, we make use of the small penetration-depth approximation for the internal magnetic field to derive a system of equations that refers only to the external field. Thus the difficulties with the spheroidal wavefunctions do not arise here. Moreover, even though the SPA was developed for high frequencies, it appears to provide a good approximation at all frequencies for spheroids with large relative permeability ($\mu_r \gtrsim 100$ — as characteristic of steel, for example).

The simplicity and validity of the SPA method motivates us to apply it to case of the oblate spheroids. Using the SPA solutions, we also investigate the total response from a collection of spheroids by neglecting the mutual interactions between the spheroids. It is shown that when spheroids of multiple sizes are present, their responses could overlap in such a way that makes it difficult to isolate their individual responses or infer their individual parameters. Thus the relatively simple equations derived under SPA could serve very well in the development of model-based inversion methods, where fast forward model calculations are a prerequisite. Should higher accuracy or lower relative permeability be required, the simple and pragmatic method of rational function approximation presented in [20] can be adopted to bridge the "frequency gap" between the exact numerical results on the low induction-number end and the SPA results on the high induction-number end.

Chapter 3

Monte Carlo Simulation of Multiple Scattering by Dielectric Spheroids

3.1 Introduction

The study of electromagnetic wave scattering by nonspherical particles is rich in applications in the biomedical, interstellar, and geophysical settings [5]. In geophysical remote sensing, these include rain drops [24], leaves and branches in a forest [33], as well as ice particles and brine pockets in sea ice [34, 35]. The nonspherical objects might also be manmade, e.g., landmines and unexploded ordnance, a topic which is addressed in Chapter 2. Following the strategy of Chapter 2, we consider scattering by spheroid as the canonical nonspherical model. However, contrary to Chapter 2, the focus in this chapter and Chapter 4 is to study coherent multiple scattering of waves by a densely packed distribution of spheroidal particles. In the past, extensive theoretical, numerical, and experimental studies of wave scattering by densely packed dielectric spheres have demonstrated the significance of these multiple scattering effects [36, 37, 38, 39, 40] and its relevance in microwave remote sensing of snow [41, 42].

For scattering by a single dielectric spheroid, several methodologies are in use. For spheroids with shapes close to a sphere, the T-matrix approach, which is based on spherical wave expansions and the extended boundary conditions, is perhaps the most convenient [43]. For spheroids with size small compared to the incident wavelength, Rayleigh scattering offers a simple and accurate approximation [3, 44]. The spheroidal wavefunction expansion method, similar to the manner done in Chapter 2, provides the most rigorous basis for analytical calculations [24, 25, 26, 27]. Numerical techniques such as the discrete dipole approximation (DDA) are also useful for spheroids with moderate sizes [45, 46] and have the added benefit of being applicable to particles of arbitrary shapes.

The problem is more challenging when multiple scattering effects are to be included. Multiple scattering calculations are often formulated in terms of the Foldy-Lax multiple scattering equations [9]. In this formulation, the field that excites each particle is expressed as a sum of the incident field and the scattered fields from all other particles. A system of equations for the exciting field for each particle can then be set up in a self-consistent manner and solved numerically. The key is to come up with a way to relate the exciting field to the scattered field for each particle. For spherical particles, this can be done quite effectively using the spherical wavefunction expansion (or T-matrix coefficients) [37, 47]. For spheroids, the spheroidal wavefunction approach has been used [26]. Both of these wave expansion methods rely on the translational addition theorems to relate the waves centered at one particle to waves centered at another particle [48, 49]. For the case of spheroids, the formulation is sufficiently complex that even though the multiple scattering formulation exists, numerical investigations have been limited to only two spheroids. For multiple scattering in dense random medium, an additional complication arises from the need to obtain a physically realistic description of how spheroidal particles are distributed relative to one another. An oversimplified choice could lead to meaningless results

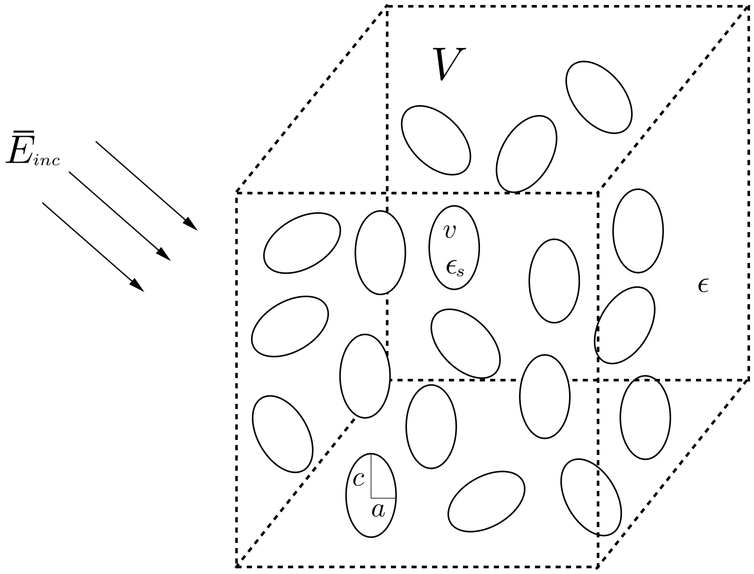

Figure 3-1: Scattering of electromagnetic waves by densely packed prolate spheroids with identical volume $v = 4\pi a^2 c/3$ and permittivity ϵ_s.

when the particles are packed sufficiently close together [8].

In this chapter, we use Monte Carlo simulations to study electromagnetic wave scattering by a collection of dielectric prolate spheroids (Fig. 3-1). The spheroids are assumed to be small compared to the wavelength. The small-particle assumption allows us to use a much simpler multiple scattering formulation in terms of volume integral equation instead of the spheroidal wavefunctions. This assumption is valid in many microwave remote sensing applications. The formulation presented can be applied to multiple species of particles with different sizes, permittivities, and aspect ratios. However, for the sake of simplicity, they are assumed here to be identical. In Chapter 4, analytical approximations are used to study the same problem.

The rest of this chapter proceeds as follows. In Sec. 3.2, we describe the procedure for generating random configurations of spheroids subjected to hard-core repulsion using the Metropolis Monte Carlo method. In Sec. 3.3, we present the multiple scattering formulation based on a volume integral equation for the electric field. The integral equation is solved numerically using the method of moment (MoM) with electrostatic basis functions. The simulation results are shown in Sec. 3.4 in terms of radiative transport quantities such as the scattering coefficient, absorption coefficient, and scattering phase matrix. The simulation results are compared with results from the independent scattering approximation. It is found that when the fractional volume of the spheroids is appreciable, the multiple scattering results differ significantly from independent scattering. The simulation results in Sec. 3.4 are obtained using only dipole basis functions with matrix elements approximated using point interactions. In Sec. 3.5, we evaluate the effects of nonuniform induced field by computing the interaction integrals exactly. The conclusions of this chapter can be found in Sec. 3.6.

3.2 Generation of Physical Configurations of Spheroids

Consider N prolate spheroids in a volume V. The spheroids are non-interacting except for hard-core repulsion. The spheroids are randomly positioned inside V; however, as a result of the hard-core repulsion, the joint probability distribution of the spheroids is non-trivial. We use the Monte Carlo method of Metropolis *et al.* [50] to generate statistical realizations of particle positions for these spheroids. Monte Carlo simulations of hard ellipsoids (of which the spheroids are special cases) were first reported by Perram *et al.* [51]. In Sect. 3.2.1, the implementation of the Metropolis method is described. In Sect. 3.2.2, we illustrate simulation results in terms of the pair distribution function, which plays an important role in multiple scattering theories. Monte Carlo simulation of nonspherical particles remains an active topic of research for molecular physicists with interests in liquid crystals [52].

3.2.1 Metropolis Shuffling Method

The Monte Carlo simulation is performed using the canonical ensemble (fixed V, N, and T). A state j with energy U_j is present with probability proportional to $\exp(-\beta U_j)$, where $\beta = 1/k_B T$. In their pioneering work, Metropolis *et al.* [50] proved that the states can be sampled computationally with the following *shuffling* procedure.

Given that the particles are in state j with energy U_j, make a random displacement to a particle so that the particles are in state l with energy U_l. Consider the factor $r = \exp(-\beta(U_l - U_j))$ and choose a random number ν from [0,1]. If $r \geq \nu$, then the new state l is accepted. Otherwise, we return the particles to state j. Note that if $U_l < U_j$, r is always greater than 1 so that the state l is always accepted regardless of the value of ν. Since the new state only depends on its previous state, this represents a Markov process. For a sufficiently long chain of configurations generated in this way, a state n will be approached with probability proportional to $\exp(-\beta U_n)$.

The algorithm is particularly simple for particles with hard-core repulsion, where the potential energy between a pair of particles is infinite if they overlap and zero otherwise. Since a displacement would lead to either the overlap or non-overlap of particles, the factor r is either 0 or 1 — leading to rejection or acceptance, respectively. Thus it is not necessary to compare it with some selected random number ν. For nonspherical particles, the displacement in general consists of both "translation" and "rotation" in space.

Now specialize to the case of prolate spheroids in a cubic volume. Instead of using the semiaxes a and c as inputs, we specify the fractional volume $f_v = Nv/V$, where $v = 4\pi(a^2c)/3$ is the volume of each spheroid, and the elongation ratio $e = c/a$. The configuration of each spheroid is completely determined by its center coordinates $\overline{r}_{cj}$ and orientation angles (α_j, β_j) (Fig. 3-2). The symmetry axis of spheroid j is given by

$$\hat{z}_{bj} = \sin\beta_j \cos\alpha_j \hat{x} + \sin\beta_j \sin\alpha_j \hat{y} + \cos\beta_j \hat{z} \tag{3.1}$$

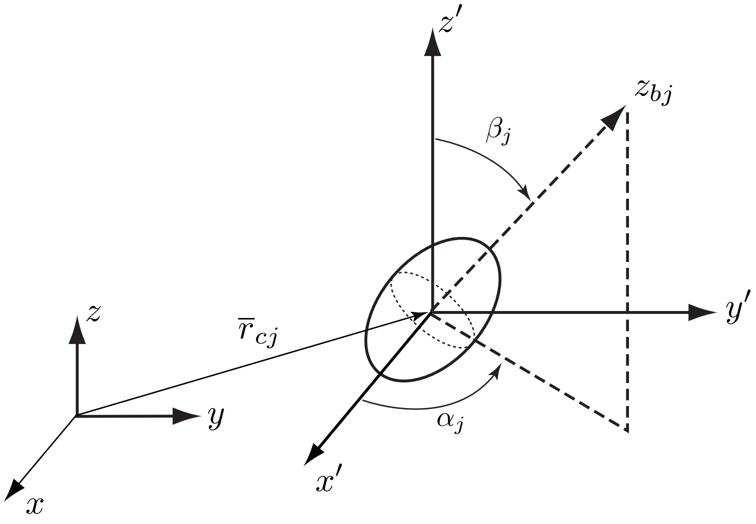

Figure 3-2: Coordinate and orientation specification of spheroid j.

The simulation proceeds as follows:

- *Step 1*: Start with an initial configuration, e.g., by placing the particles in a 3-D grid with no overlap.
- *Step 2*: Make a random displacement of one particle:

$$x_{cj} \to x_{cj} + \Delta(2a)\nu_1, \qquad y_{cj} \to y_{cj} + \Delta(2a)\nu_2, \qquad z_{cj} \to z_{cj} + \Delta(2a)\nu_3$$

and, for randomly oriented spheroids,

$$\cos\beta_j \to \cos\beta_j + \Delta_\beta\nu_4, \qquad \alpha_j \to \alpha_j + \Delta_\alpha(2\pi)\nu_5$$

where Δ determines maximum translation allowed in each displacement while Δ_α and Δ_β dictate the maximum rotation. The numbers ν_k with $k = 1, 2, \ldots, 5$ are randomly and uniformly chosen from the interval $[-1, 1]$. Note that $\cos\beta_j$ instead of β_j is used in the rotation since the random orientation implies uniform distribution in solid angle.

During the attempted displacement, a particle could move outside the simulation volume. To conserve particle number as well as to minimize surface boundary effects due to the finite simulation volume, periodic boundary condition is employed. Thus if a particle moves outside the cube on one side, it re-enters the cube from the opposite side.

- *Step 3*: If the new position and orientation results in overlap, reject the move and put particle back. Otherwise, accept the move. Each attempted displacement, whether eventually accepted or not, represents a new configuration and is called a Monte Carlo Step (MCS). The displacement constants $(\Delta, \Delta_\alpha, \Delta_\beta)$ are chosen so that the acceptance rate is about 50%. The checking of overlap is accomplished using the ellipsoidal contact function due to Perram *et al.* [53].

- *Step 4*: Repeat Steps 2–3 for all N particles.

- *Step 5*: Repeat Steps 2–4 M times to ensure that a sufficiently long Markov chain has been computed. Thus after MN MCS, we record one realization.

- *Step 5*: Repeat Steps 1–5 to obtain N_r realizations.

The positions and orientations of the particles for each realization generalized in this way will be used as inputs in the scattering calculations. Before we discuss scattering based on these particle configurations, it is interesting to make a brief digression and examine the statistics of particle positions in the form of the pair distribution function.

3.2.2 Pair Distribution Function

An important quantity which can be easily obtained from the Monte Carlo simulations is the pair distribution function. The pair distribution function is proportional to the two-particle joint probability distribution function [54, 55]:

$$g(\overline{r}_1, \overline{r}_2) = \frac{N-1}{N} V^2 p(\overline{r}_1, \overline{r}_2) = \frac{N-1}{N} V p(\overline{r}_1 | \overline{r}_2) \tag{3.2}$$

where $p(\overline{r}_1, \overline{r}_2)$ is the joint probability distribution function and $p(\overline{r}_1|\overline{r}_2)$ is the conditional probability. For $N \gg 1$, the prefactor of $(N-1)/N$ can be dropped. Since the system is translationally invariant, the pair distribution only depends on the separation vector $\overline{r} = \overline{r}_1 - \overline{r}_2$. Note that when the separation is large, the positions of particles 1 and 2 become uncorrelated. In this case $p(\overline{r}_1, \overline{r}_2) \to p(\overline{r}_1)p(\overline{r}_2) = 1/V^2$ and $g(\overline{r}) \to 1$ as $r \to \infty$. Moreover, for prolate spheroids governed by hard-core repulsion, $g(\overline{r}) = 0$ for $r < 2a$.

For spheroids with random orientations, the pair distribution function also depends on the orientations of the two particles [56]. We define the orientation-averaged pair distribution function

$$g(\overline{r}) = \int d\Omega_1 p(\Omega_1) \int d\Omega_2 p(\Omega_2) g(\overline{r}; \Omega_1, \Omega_2) \tag{3.3}$$

where $d\Omega_j = \sin\beta_j d\beta_j d\alpha_j$ and $p(\Omega_j) = 1/(4\pi^2)$. Averaging over the directions of the separation vector gives the radial distribution function (RDF)

$$g_o(r) = \frac{1}{4\pi^2} \int d\Omega_r g(\overline{r}) \tag{3.4}$$

To deduce the radial distribution function from the Monte Carlo simulations, we count and tabulate the number of pair separations. The detailed procedure can be found elsewhere (e.g., [9]) and will not be repeated here. In the following, we illustrate the radial distribution functions obtained using Monte Carlo simulations. For the cases of spheres and aligned spheroids, the analytical Percus-Yevick (PY) pair distribution function can be computed (see Chapter 4) and will be shown for comparison.

In Fig. 3-3, we show the RDFs for the special case of hard spheres by setting the

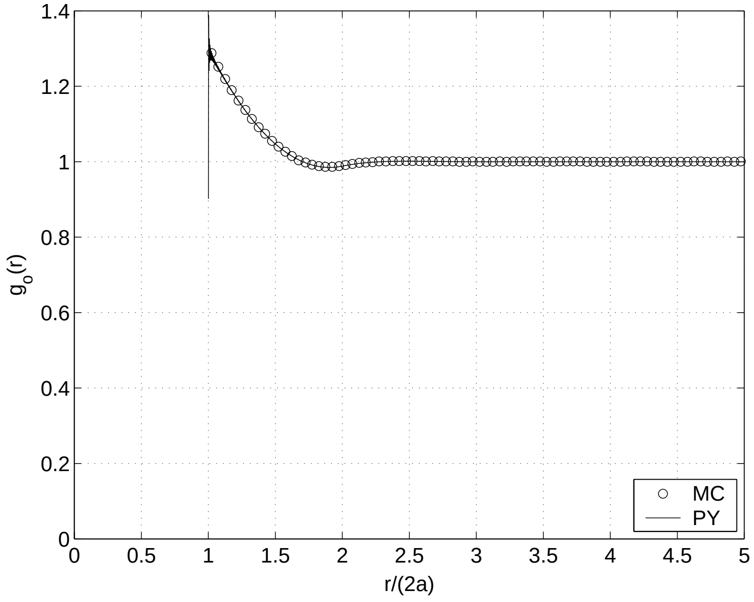

(a) $f_v = 0.1,\ e = 1.$

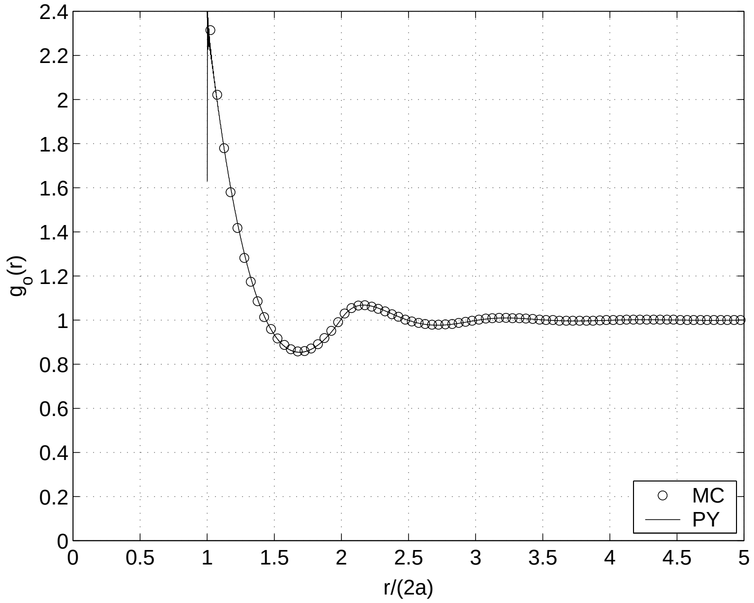

(b) $f_v = 0.3,\ e = 1.$

Figure 3-3: Radial distribution function $g_o(r)$ for hard spheres. The Monte Carlo (MC) simulation results agree very well with the analytical Percus-Yevick (PY) RDF. Parameters for MC: $N = 1000$, $N_r = 50$, $M = 1000$. For $f_v = 0.1$, $\Delta = 1$ giving an acceptance rate of 52%; for $f_v = 0.3$, $\Delta = 0.2$ giving an acceptance rate of 44%.

elongation ratio $e = 1$. Results for two fractional volumes, $f_v = 0.1$ and $f_v = 0.3$, are presented. For this special case, the RDF is equal to the pair distribution function. As discussed above, for $r < 2a$, the radial distribution function is zero due to core exclusion. At large separation, the pair of particles become uncorrelated and $g_o(r) \to 1$. At the larger fractional volume, the radial distribution becomes more sharply peaked at smaller separation and more oscillatory at larger separation. Note that the Monte Carlo simulation results agree very well with those from the PY pair distribution function. Both are quite different from the so-called "hole approximation," where $g_o(r) = 0$ for $r < 2a$ and 1 otherwise.

In Fig. 3-4, the RDFs for hard spheroids in aligned configurations with $e = 2$ are shown for $f_v = 0.1$ and 0.3. The main difference from the hard sphere case is that the RDF becomes much smaller near $r = 2a$ since overlap could occur for separations between $2a$ and $4a$. As in the hard sphere case, the PY RDF agrees well with the simulated RDF. Fig. 3-5 shows the corresponding RDFs for randomly oriented spheroids. For this case, no PY solution exists, and only the simulated data are plotted. The RDFs appear to be intermediate between the sphere case and the aligned spheroid case.

3.3 Multiple Scattering Formulation

In this section, we present the formulation used to solve the electromagnetic wave scattering problem for each of the realization of particle configurations generated using Metropolis shuffling. The size of the spheroid is assumed to be electrically small ($ka, kc \ll 1$), in which case the internal electric field of each spheroid is sufficiently well characterized by the electrostatic solutions. To incorporate these ideas, it is convenient to formulate the multiple scattering problem using the volume integral equation [9, 57]. This approach is quite similar to the discrete dipole approximation (DDA) [45, 46], which divides a "continuous" dielectric object into regular array of

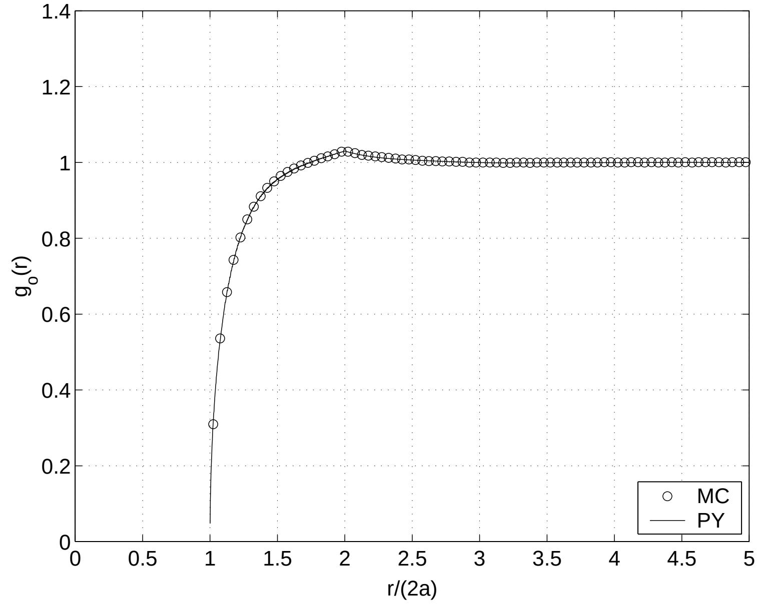

(a) $f_v = 0.1,\ e = 2.$

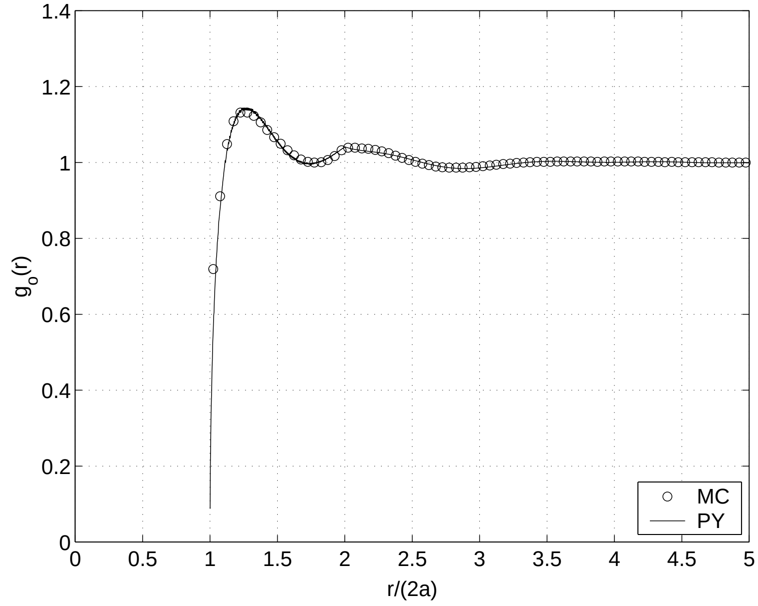

(b) $f_v = 0.3,\ e = 2.$

Figure 3-4: Radial distribution function $g_o(r)$ for hard prolate spheroids in aligned configurations. The Monte Carlo (MC) simulation results agree very well with the analytical Percus-Yevick (PY) RDF. Parameters for MC: $N = 1000$, $N_r = 50$, $M = 1000$. For $f_v = 0.1$, $\Delta = 1.2$ with acceptance rate of 51%; for $f_v = 0.3$, $\Delta = 0.2$ with acceptance rate of 49%.

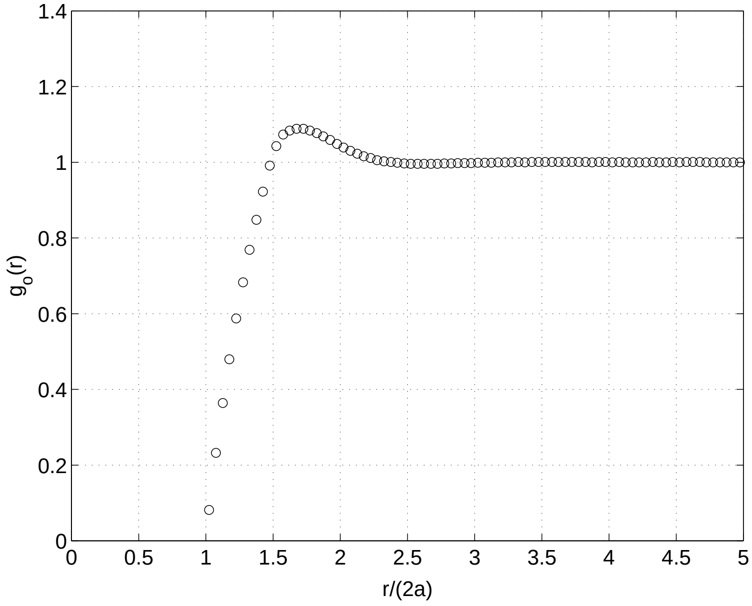

(a) $f_v = 0.1,\ e = 2.$

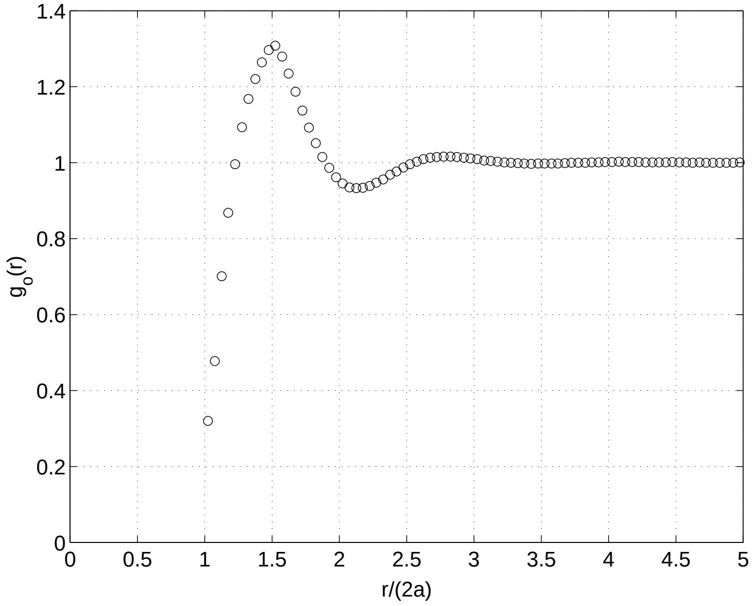

(b) $f_v = 0.3,\ e = 2.$

Figure 3-5: Radial distribution function $g_o(r)$ for randomly oriented hard prolate spheroids. Parameters for MC: $N = 1000$, $N_r = 50$, $M = 1000$. For $f_v = 0.1$, $\Delta = 1.2$, $\Delta_\alpha = \Delta_\beta = 1$ with acceptance rate of 48%; for $f_v = 0.3$, $\Delta = 0.1$, $\Delta_\alpha = \Delta_\beta = 0.05$ with acceptance rate of 39%.

small cells characterized by their dipole moments. In our case, the "cells" are the entire spheroidal particles which are randomly distributed in space.

3.3.1 Volume Integral Equation for the Electric Field

Consider a "scatterer" with permittivity $\epsilon_s(\overline{r})$ and volume V in a homogeneous background medium with permittivity ϵ. An incident field $\overline{E}_{inc}(\overline{r})$ impinges on the scatterer. The electric field satisfies the following integral equation [9]:

$$\overline{E}(\overline{r}) = \overline{E}_{inc}(\overline{r}) + k^2 \int_V d\overline{r}' \, \overline{\overline{G}}_o(\overline{r}, \overline{r}') \cdot [\varepsilon_s(\overline{r}') - 1] \, \overline{E}(\overline{r}') \tag{3.5}$$

where $k = \omega\sqrt{\mu\epsilon}$ is the background wavenumber, $\varepsilon_s(\overline{r}) = \epsilon_s(\overline{r})/\epsilon$ is the relative permittivity of the "scatterer," and $\overline{\overline{G}}_o(\overline{r}, \overline{r}')$ is the dyadic Green's function for the background medium

$$\overline{\overline{G}}_o(\overline{r}, \overline{r}') = \left(\overline{\overline{I}} + \frac{\nabla\nabla}{k^2}\right) \frac{e^{ikR}}{4\pi R} \tag{3.6}$$

with $\overline{R} = \overline{r} - \overline{r}'$.

Suppose now that the "scatterer" consists of N identical spheroids with constant relative permittivity ε_s. Then Eq. (3.5) becomes

$$\overline{E}(\overline{r}) = \overline{E}_{inc}(\overline{r}) + k^2 \left[\varepsilon_s - 1\right] \sum_{j=1}^{N} \int_v d\overline{r}_j \, \overline{\overline{G}}_o(\overline{r}, \overline{r}_j) \cdot \overline{E}(\overline{r}_j) \tag{3.7}$$

where v is the volume of the spheroid. In Eq. (3.7), let $\overline{r}$ be inside spheroid l ($l = 1, 2, \ldots, N$). This gives the volume integral equation with which the internal electric fields of all spheroids are related.

$$\overline{E}(\overline{r}_l) = \overline{E}_{inc}(\overline{r}_l) + k^2 \left[\varepsilon_s - 1\right] \sum_{j=1}^{N} \int_v d\overline{r}_j \, \overline{\overline{G}}_o(\overline{r}_l, \overline{r}_j) \cdot \overline{E}(\overline{r}_j) \tag{3.8}$$

3.3.2 Method of Moments

The volume integral equation (3.8) will be solved numerically using the method of moments (MoM) [58]. First expand the internal field $\overline{E}(\overline{r}_j)$ in terms of a set of orthonormal basis functions $\overline{f}_{j\alpha}$:

$$\overline{E}(\overline{r}_j) = \sum_{\alpha=1}^{N_b} a_{j\alpha}\overline{f}_{j\alpha}(\overline{r}_j) \tag{3.9}$$

where $a_{j\alpha}$ is the unknown expansion coefficients and N_b is the total number of basis functions. Note that we use Latin indices are used for particles and Greek indices for basis functions. The choice of the basis functions are discussed in Sec. 3.3.3.

The incident field can likewise be expanded.

$$\overline{E}_{inc}(\overline{r}_j) = \sum_{\alpha=1}^{N_b} b'_{j\alpha}\overline{f}_{j\alpha}(\overline{r}_j) \tag{3.10}$$

Putting (3.9) and (3.10) into (3.8) gives

$$\sum_{\beta=1}^{N_b} a_{l\beta}\overline{f}_{l\beta}(\overline{r}_l) = \sum_{\beta=1}^{N_b} b'_{l\beta}\overline{f}_{l\beta}(\overline{r}_l) + \sum_{j=1}^{N}\sum_{\alpha=1}^{N_b} a_{j\alpha}\overline{q}_{j\alpha}(\overline{r}_l) \tag{3.11}$$

where

$$\overline{q}_{j\alpha}(\overline{r}_l) = k^2\left[\varepsilon_s - 1\right]\int_v d\overline{r}_j\ \overline{\overline{G}}_o(\overline{r}_l, \overline{r}_j)\cdot\overline{f}_{j\alpha}(\overline{r}_j) \tag{3.12}$$

Note that when $l = j$ (or *self-patch* in MoM parlance), the dyadic Green's function $\overline{\overline{G}}_o(\overline{r}_j, \overline{r}_l)$ has a source region singularity at $\overline{r}_j = \overline{r}_l$ [59]. This requires special treatment and will be addressed in Sec. 3.3.3. It will be shown that when $l = j$, we can write

$$\overline{q}_{j\alpha}(\overline{r}_j) = C_\alpha\overline{f}_{j\alpha}(\overline{r}_j) \tag{3.13}$$

where C_α is a constant coefficient.

Applying the Galerkin's method to (3.11), we obtain

$$a_{l\beta} = b_{l\beta} + \frac{1}{(1 - C_{l\beta})} \sum_{j \neq l}^{N} \sum_{\alpha=1}^{N_b} A_{l\beta;j\alpha} a_{j\alpha} \tag{3.14}$$

where

$$b_{l\beta} = \frac{1}{(1 - C_{l\beta})} b'_{l\beta} \tag{3.15}$$

and

$$\begin{aligned} A_{l\beta;j\alpha} &= \int_v d\overline{r}_l \; \overline{f}_{l\beta}(\overline{r}_l) \cdot \overline{q}_{j\alpha}(\overline{r}_l) \\ &= k^2 \left[\varepsilon_s - 1\right] \int_v d\overline{r}_l \int_v d\overline{r}_j \; \overline{f}_{l\beta}(\overline{r}_l) \cdot \overline{\overline{G}}_o(\overline{r}_l, \overline{r}_j) \cdot \overline{f}_{j\alpha}(\overline{r}_j) \end{aligned} \tag{3.16}$$

Eq. (3.14) can be cast in matrix form by consolidating the two indices $\{j, \alpha\}$ into one. Then we have

$$\overline{\overline{Z}} \cdot \overline{a} = \overline{b} \tag{3.17}$$

where $\overline{\overline{Z}}$ is often called the impedance matrix and is of size $NN_b \times NN_b$.

If we set all interaction terms to zero, i.e., $A_{l\beta;j\alpha} = 0$, we obtain from Eq. (3.14)

$$a_{l\beta} = b_{l\beta} \tag{3.18}$$

This corresponds to the independent scattering approximation.

3.3.3 Electrostatic Basis Functions

Since we are interested in scattering by small dielectric spheroids, the electrostatic solution provides a good approximation to the internal field. Thus we choose the basis functions from the electrostatic solution. The scalar potential for the electrostatic field satisfies the Laplace solution, which is separable in spheroidal coordinates. (The Laplace solution has also been used in Chapter 2 for the magnetic field.) The solution

α	n	m	p	multipole
1	1	0	0	dipole
2	1	1	0	dipole
3	1	1	1	dipole
4	2	0	0	quadrupole
5	2	1	0	quadrupole
6	2	1	1	quadrupole
7	2	2	0	quadrupole
8	2	2	1	quadrupole

Table 3.1: Correspondence between the basis function index α and multipole indices $\{n, m, p\}$.

which is regular at the origin is given as

$$\Phi_\alpha(\overline{r}) = (-1)^{m+1} P_n^m(\eta) P_n^m(\xi) T_{pm}(\phi) \tag{3.19}$$

where $P_n^m(\eta)$ and $P_n^m(\xi)$ are associated Legendre functions of first kind [30] and

$$T_{pm}(\phi) = \begin{cases} \cos m\phi, & p = 0 \\ \sin m\phi, & p = 1 \end{cases} \tag{3.20}$$

The sign factor $(-1)^{m+1}$ in (3.19) is chosen so that the sign of the dipole basis functions will agree with the convention used in [57]. The triplet of indices $\{n, m, p\}$ range as follows: $n \geq 1$, $0 \leq m \leq n$, $p = 0, 1$. We shall use a single index α to denote the triplet. The correspondence between the indices can be found in Table 3.1.

The electric field corresponding to a particular multipole is given by $\overline{E}_\alpha = -\nabla\Phi_\alpha$. Consider a single spheroid with center at the origin and principal axes aligned with the coordinate axes. The basis functions are

$$\overline{f}_\alpha(\overline{r}) = -\frac{1}{\sqrt{N_\alpha}} \nabla\Phi_\alpha(\overline{r}) \tag{3.21}$$

with normalization constant N_α chosen such that

$$\int_v d\overline{r}\ \overline{f}_\alpha \cdot \overline{f}_\beta = \delta_{\alpha\beta} \tag{3.22}$$

The orthogonality between the different basis functions can be easily established. With the use of the divergence theorem, the normalization constant is

$$N_\alpha = \int_s dS \; \Phi_\alpha (\hat{n} \cdot \nabla \Phi_\alpha) \tag{3.23}$$

where s denotes the surface of the spheroid ($\xi = \xi_o$). Substituting Φ_α from (3.19), we arrive at

$$N_\alpha = \left[\frac{1}{\nu_m} \frac{4\pi}{2n+1} \frac{(n+m)!}{(n-m)!} \right] \frac{d}{2} (\xi_o^2 - 1) \frac{dP_n^m}{d\xi_o} P_n^m(\xi_o) \tag{3.24}$$

where $\nu_m = 2 - \delta_{m0}$ is known as the Neumann factor [60].

We now discuss the self-patch contributions and derive expressions for coefficients C_α as defined in (3.13). We need to evaluate

$$\overline{q}_\alpha(\overline{r}) = k^2 \left[\varepsilon_s - 1 \right] \int_v d\overline{r}' \; \overline{\overline{G}}_o(\overline{r}, \overline{r}') \cdot \overline{f}_\alpha(\overline{r}') \tag{3.25}$$

with $\overline{r} \in v$. This can be obtained in two ways. The first makes use of electrostatics [57] while the second proceeds through a low-frequency expansion of the dyadic Green's function.

Electrostatics approach

For small particles, the quantity $\overline{q}_\alpha(\overline{r})$ can be shown [9] to correspond physically to the electric field induced inside the particle as a result of the polarization:

$$\overline{P} = (\epsilon_s - \epsilon) \overline{f}_\alpha \tag{3.26}$$

Let V_1 and V_0 be the scalar potential inside and outside the spheroid. They must satisfy the following boundary conditions at $\xi = \xi_o$:

$$V_1 = V_0 \tag{3.27}$$

$$\hat{\xi} \cdot \nabla V_1 - \hat{\xi} \cdot \nabla V_0 = \hat{\xi} \cdot \frac{\overline{P}}{\epsilon} \tag{3.28}$$

It is clear from the expression of $\overline{P}$ in Eq. (3.26) that V_0 and V_1 contain only multipole α. Thus we let

$$V_0 = \frac{A_0}{\sqrt{N_\alpha}} P_n^m(\eta) Q_n^m(\xi) T_{pm}(\phi) \tag{3.29}$$

$$V_1 = \frac{A_1}{\sqrt{N_\alpha}} P_n^m(\eta) P_n^m(\xi) T_{pm}(\phi) \tag{3.30}$$

Note that $\overline{q}_\alpha = -\nabla V_1 = C_\alpha \overline{f}_\alpha$, which implies that $C_\alpha = A_1$.

Upon matching the boundary conditions, the coefficients A_0 and A_1 are easily solved. The latter is given by

$$A_1 = (\varepsilon_s - 1)(-1)^{m+1} \frac{(n-m)!}{(n+m)!} (\xi_o^2 - 1) \frac{dP_n^m}{d\xi_o} Q_n^m(\xi_o) \tag{3.31}$$

where we have made use of the following Wronskian relation for Legendre functions [30]:

$$W\{P_n^m(z), Q_n^m(z)\} = (-1)^{m+1} \frac{(n+m)!}{(n-m)!} \frac{1}{z^2 - 1} \tag{3.32}$$

Dyadic Green's function expansion

The electrostatics approach lends itself to simple interpretation of the self-patch term but represents only the leading order contribution. The more general method for deriving the self-patch term is to make use of the low-frequency expansion of the dyadic Green's function $\overline{\overline{G}}_o(\overline{r}, \overline{r}')$ [9, 61]. The dyadic Green's function is given in Eq. (3.6). The second term contains a non-integrable singularity which gives rise to the leading order contribution to the self-patch term.

In the low-frequency limit, we can expand the exponential term $\exp(ikR)$ in $\overline{\overline{G}}_o(\overline{r}, \overline{r}')$ in powers of kR. This leads to the following decomposition of the dyadic Green's function into a regular part and a singular part.

$$\overline{\overline{G}}_o(\overline{r}, \overline{r}') = \overline{\overline{G}}_r(\overline{r}, \overline{r}') + \frac{1}{k^2} \overline{\overline{G}}_s(\overline{r}, \overline{r}') \tag{3.33}$$

where

$$\overline{\overline{G}}_r(\overline{r},\overline{r}') = \frac{1}{8\pi R}\left(\overline{\overline{I}} + \hat{R}\hat{R}\right) + i\frac{2}{3}k\overline{\overline{I}} + \mathcal{O}(k^2) \tag{3.34}$$

$$\overline{\overline{G}}_s(\overline{r},\overline{r}') = \nabla\nabla g_s(\overline{r},\overline{r}') = \nabla\nabla\frac{1}{4\pi|\overline{r}-\overline{r}'|} \tag{3.35}$$

Note that the singular part $\overline{\overline{G}}_s(\overline{r},\overline{r}')$ has no k dependence and is present for electrostatics problem as well. This fact leads to the electrostatics approach used earlier. To obtain the self-patch coefficients, consider first

$$\begin{aligned}\overline{S}_\alpha &= \int_v d\overline{r}'\ \overline{\overline{G}}_s(\overline{r},\overline{r}')\cdot\overline{f}_\alpha(\overline{r}') = \frac{1}{\sqrt{N_\alpha}}\nabla\int_v d\overline{r}'\ \nabla' g_s(\overline{r},\overline{r}')\cdot\nabla'\Phi_\alpha(\overline{r}')\\ &= \frac{1}{\sqrt{N_\alpha}}\nabla\int_s dS'\ g_s(\overline{r},\overline{r}')\hat{n}'\cdot\nabla'\Phi_\alpha(\overline{r}')\end{aligned} \tag{3.36}$$

The static Green's function can be expanded in terms of the associated Legendre functions. For $\xi < \xi'$,

$$g_s(\overline{r},\overline{r}') = \frac{2}{d}\sum_{m=0}^{\infty}\sum_{n=m}^{\infty}\sum_{p=0}^{1} c_{nm}P_n^m(\eta)P_n^m(\eta')Q_n^m(\xi)P_n^m(\xi')T_{pm}(\phi)T_{pm}(\phi') \tag{3.37}$$

where

$$c_{nm} = \frac{2n+1}{4\pi}\nu_m(-1)^m\left[\frac{(n-m)!}{(n+m)!}\right]^2 \tag{3.38}$$

If we replace $(-1)^m$ with i^m in Eq. (3.38), we obtain Eq. (10.3.53) in Morse and Feshbach [60]. The "discrepancy" is due to the different definition of the associated Legendre functions for $\xi > 1$ used here, which follows that of Abramowitz and Stegun [30]. Using (3.37) in (3.36) gives

$$\overline{S}_\alpha = (-1)^{m+1}\frac{(n-m)!}{(n+m)!}(\xi_o^2-1)\frac{dP_n^m}{d\xi_o}Q_n^m(\xi_o)\overline{f}_\alpha \tag{3.39}$$

We can obtain the next order corrections through the integration over the regular part of the dyadic Green's function given in (3.34). For small particles, it is important to include at least the leading imaginary part, which is known as the radiative correction term. The radiative correction term is crucial for energy conservation of the entire system and must be included to satisfy the optical theorem [61, 62]. We let

$$\overline{U}_\alpha = \int_v d\overline{r}' \; \mathrm{Im}\overline{\overline{G}}_r(\overline{r}, \overline{r}') \cdot \overline{f}_\alpha(\overline{r}') = \int_v d\overline{r}' \; \frac{2}{3} k \overline{f}_\alpha(\overline{r}') \tag{3.40}$$

It is interesting to note that $\overline{U}_\alpha$ is a *constant* vector and independent of $\overline{r}$. Hence it can be expanded in terms of dipole ($n = 1$) terms only, which correspond to uniform internal field (i.e., $\overline{f}_\alpha$ is constant). Thus

$$\overline{U}_\alpha = \begin{cases} \frac{2}{3} k v \overline{f}_\alpha & \text{for } n = 1 \\ 0 & \text{otherwise} \end{cases} \tag{3.41}$$

Incorporating the leading real and imaginary contributions, we obtain from Eq. (3.25) that

$$\overline{q}_\alpha = k^2(\varepsilon_s - 1) \left[\frac{1}{k^2} \overline{S}_\alpha + \overline{U}_\alpha \right] \tag{3.42}$$

Thus the self-patch coefficient is

$$C_\alpha = (\varepsilon_s - 1) \left[(-1)^{m+1} \frac{(n-m)!}{(n+m)!} (\xi_o^2 - 1) \frac{dP_n^m}{d\xi_o} Q_n^m(\xi_o) + i \frac{2}{3} k^3 v \delta_{n1} \right] \tag{3.43}$$

This is identical to (3.31) when the radiative correction term is neglected. Subsequent calculations will be based on (3.43) with the radiative correction included.

3.3.4 Dipole Basis Functions and Point Interactions

In Appendix B, we provide explicit expressions for the first eight basis functions. When the spheroid is small enough, the electric field is sufficiently well characterized by just the electric dipoles. The three dipole basis functions for spheroid j are

$$\overline{f}_1(\overline{r}_j) = \hat{z}_{bj} \frac{1}{\sqrt{v}} \tag{3.44}$$

$$\overline{f}_2(\overline{r}_j) = \hat{x}_{bj}\frac{1}{\sqrt{v}} \tag{3.45}$$

$$\overline{f}_3(\overline{r}_j) = \hat{y}_{bj}\frac{1}{\sqrt{v}} \tag{3.46}$$

Furthermore, the interaction integrals of (3.16) can be approximated using point interactions, to viz.,

$$A_{l\beta;j\alpha} \approx k^2 v^2(\varepsilon_s - 1)\overline{f}_{l\beta} \cdot \overline{\overline{G}}_o(\overline{r}_{cl}, \overline{r}_{cj}) \cdot \overline{f}_{j\alpha} \tag{3.47}$$

where $\overline{r}_{cj}$, $\overline{r}_{cl}$ denote the center position vectors of spheroids j and l, respectively.

Likewise, the incident field component of (3.10) and (3.15) can be evaluated as:

$$b_{l\beta} \approx \frac{1}{(1 - C_{l\beta})}\overline{f}_{l\beta} \cdot \overline{E}_{inc}(\overline{r}_{cl}) \tag{3.48}$$

The dipole basis functions with point interactions will be used to compute the numerical results shown in Sec. 3.4. In Sec. 3.5, we evaluate the accuracy of point interactions by calculating the interaction integrals exactly.

3.4 Simulation Results

Let the incident field be a plane wave that propagates in the $\hat{y}$-direction with unit amplitude.

$$\overline{E}_{inc} = \hat{e}_i \; e^{iky} \tag{3.49}$$

The vertically polarized wave corresponds to $\hat{e}_i = \hat{v}_i = \hat{z}$ while the horizontally polarized wave corresponds to $\hat{e}_i = \hat{h}_i = \hat{x}$. The numerical results are presented for the cases of (*i*) perfectly aligned spheroids and (*ii*) randomly oriented spheroids. For the aligned case, the symmetry axis of the spheroid is chosen to be the z-axis. Thus vertically polarized incidence corresponds to *axial* excitation while horizontally polarized incidence corresponds to *transverse* excitation.

The matrix equation (3.17) is solved iteratively using the biconjugate gradient stabilized method (Bi-CGSTAB) [63]. For all cases presented here, the solutions converge quickly in less than 10 iterations with a relative error of less than 10^{-6}.

3.4.1 Scattering Coefficient

After the matrix equation (3.17) is solved, the scattered field can be obtained from (3.7) with $\overline{r}$ outside the spheroids. In the far field $r \to \infty$, we have

$$\overline{E}_s(\overline{r}) = \frac{e^{ikr}}{r}\overline{F}(\hat{k}_s, \hat{k}_i) \tag{3.50}$$

with the scattering amplitude $\overline{F}$ given by:

$$\overline{F}(\hat{k}_s, \hat{k}_i) = \frac{k^2 v}{4\pi}\left[\varepsilon_s - 1\right]\left(\hat{v}_s\hat{v}_s + \hat{h}_s\hat{h}_s\right) \cdot \sum_{j=1}^{N}\sum_{\alpha=1}^{3} a_{j\alpha}\overline{f}_{j\alpha}e^{-i\overline{k}_s\cdot\overline{r}_j} \tag{3.51}$$

Note that only the dipoles ($\alpha \leq 3$) contribute to the far-field radiation even when higher-order multipole basis functions are included. The average, or coherent, scattered field is

$$\langle E_{sp}\rangle = \frac{1}{N_r}\sum_{\ell=1}^{N_r} E_{sp}^{(\ell)} \tag{3.52}$$

where $p = v, h$ denotes the polarization of the scattered field. The incoherent scattering cross section is

$$\sigma_p^{(incoh)} = \frac{r^2}{N_r}\sum_{\ell=1}^{N_r}\left|E_{sp}^{(\ell)} - \langle E_{sp}\rangle\right|^2 \tag{3.53}$$

An important quantity to simulate is the scattering coefficient κ_s.

$$\kappa_s = \frac{1}{V}\int_{4\pi} d\Omega_s \,\left(\sigma_v^{(incoh)} + \sigma_h^{(incoh)}\right) \tag{3.54}$$

For lossless particles, $\kappa_s = \kappa_e$, where κ_e is the extinction coefficient.

In Fig. 3-6, we show the convergence of the normalized scattering coefficient κ_s/k with respect to the number of realizations used. For these results, $N = 1000$, $f_v = 0.2$, $ka = 0.2$, $e = 2$, and $\varepsilon_s = 3.2$. Note that the scattering coefficient starts at zero for one realization because the incoherent field is zero. For the aligned case, the scattering coefficient due to the vertically polarized wave is larger because the larger physical dimension in the axial direction. For the randomly oriented case, we do not expect any polarization dependence in the scattering coefficient. As convergence is reached, the difference between the scattering coefficients of the two polarizations approaches zero.

In Fig. 3-7, the normalized scattering coefficient is shown as a function of fractional volume f_v. The size parameter is $ka = 0.2$ with elongation ratio $e = 2$. The independent scattering results are shown for comparison. For small fractional volume ($f_v \lesssim 5\%$), the independent scattering approximation gives reasonable results compared with the Monte Carlo simulations. However, as f_v increases, multiple scattering become more important. The interference of the scattered waves from the particles tends to reduce the overall scattered field. As a result, the scattering coefficient is much smaller than that predicted by independent scattering. Note that the scattering coefficient first increases with f_v, reaches a maximum with f_v between 0.2 and 0.3, and declines as f_v increases further. The scattering coefficient for the randomly oriented case falls in between the vertical and horizontal polarized results of the aligned configuration.

We next illustrate in Fig. 3-8 the dependence of the κ_s on the elongation ratio. The fractional volume is fixed at 0.2 and $ka = 0.2$. The monotonous increase as a function of e for both the aligned and randomly oriented is expected since the overall volume of the spheroids increases linearly with e for fixed a. The difference between the simulated results and independent scattering results tends to increase as e increases. However, their ratios are found not to vary significantly with e.

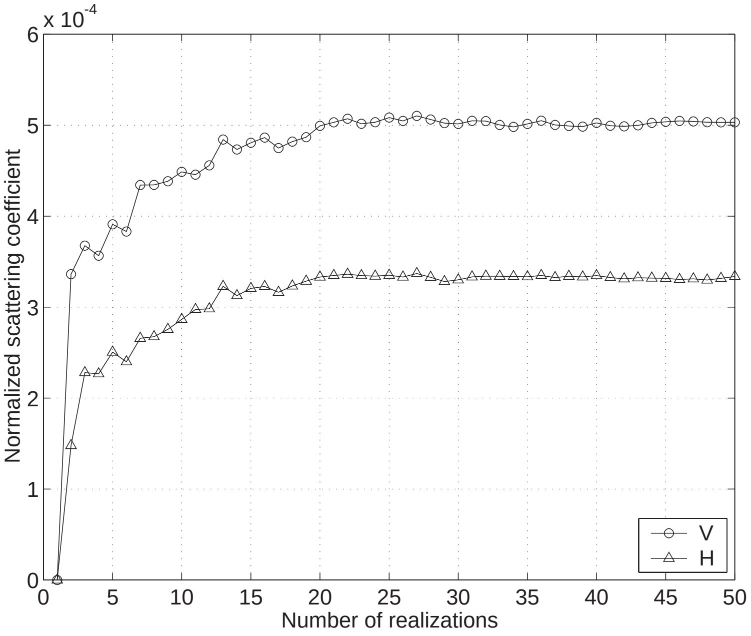

(a) Aligned case.

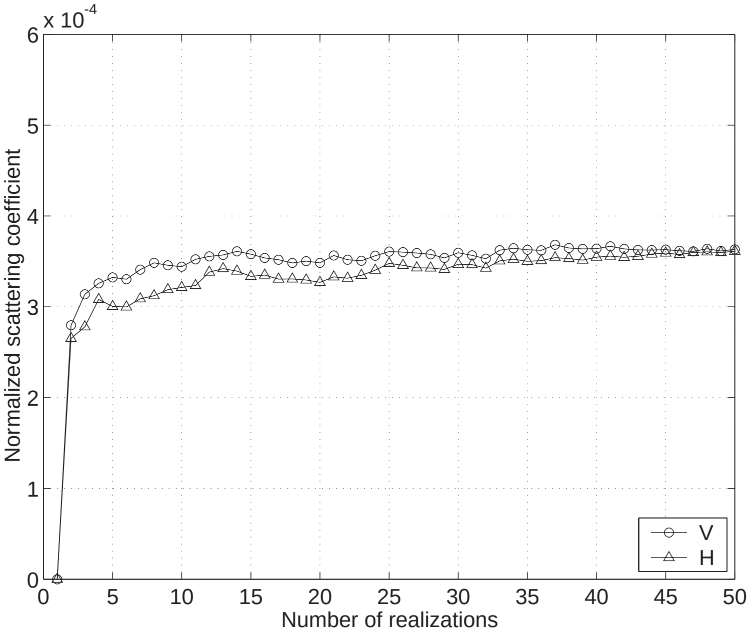

(b) Randomly oriented case.

Figure 3-6: Convergence of the normalized scattering coefficient κ_s/k with respect to the number of realizations. $N = 1000$, $ka = 0.2$, $e = 2$, and $\varepsilon_s = 3.2$.

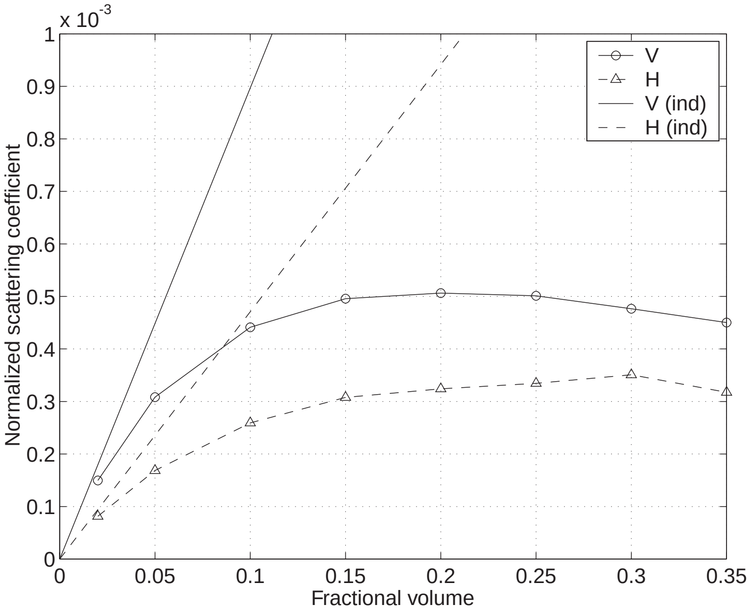

(a) Aligned case.

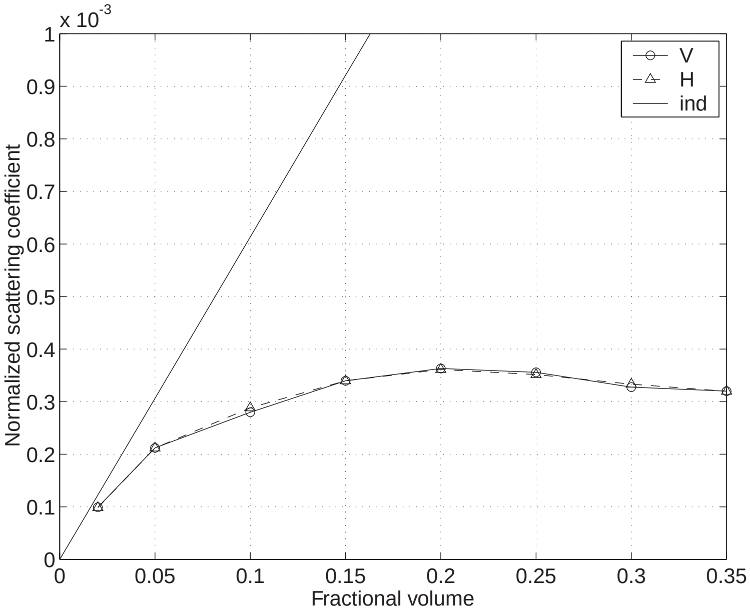

(b) Randomly oriented case.

Figure 3-7: Normalized scattering coefficient κ_s/k as a function of fractional volume f_v. $ka = 0.2$, $e = 2$, and $\varepsilon_s = 3.2$. $N = 1000$ and 50 realizations are used.

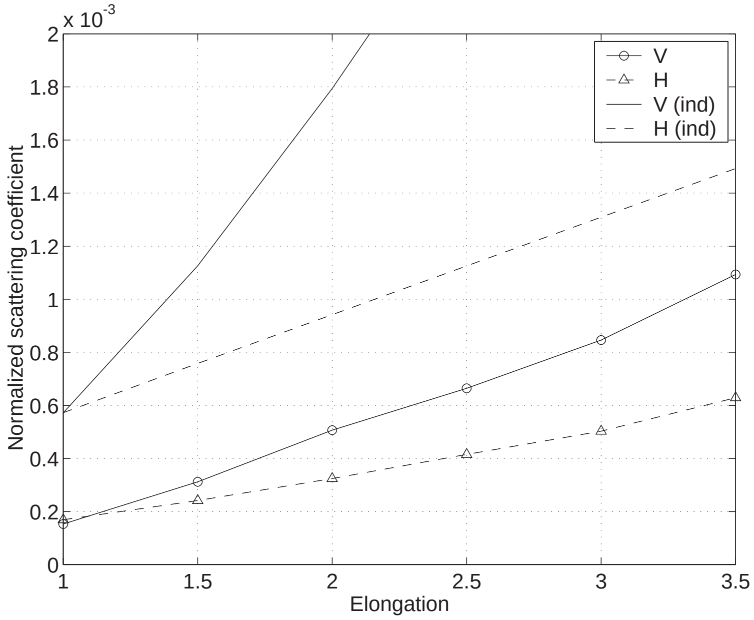

(a) Aligned case.

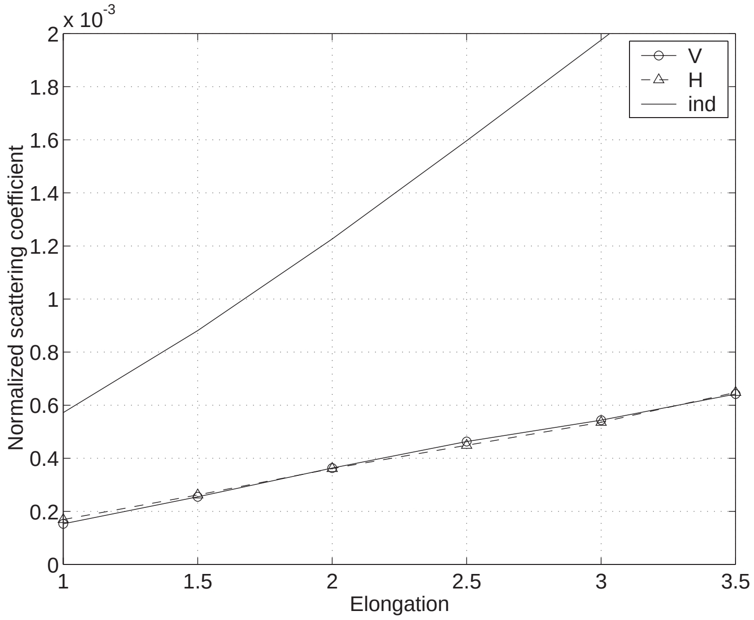

(b) Randomly oriented case.

Figure 3-8: Normalized scattering coefficient κ_s/k as a function of elongation ratio $e = b/a$. $ka = 0.2$, $f_v = 0.2$, and $\varepsilon_s = 3.2$. $N = 1000$ and 50 realizations are used.

3.4.2 Scattering Phase Matrix

The incoherent scattering cross sections defined in (3.53) can be used to obtain the scattering phase matrix. In the context of radiative transfer theory, the phase matrix $\overline{\overline{P}}$ is a 4×4 matrix that relates the incident intensity to the scattered intensity due to a random medium with elemental volume V. It can be expressed as bistatic scattering cross sections per unit volume [4, 9]:

$$\overline{\overline{P}} = \frac{1}{V} \begin{bmatrix} \langle |\mathcal{F}_{vv}|^2 \rangle & \langle |\mathcal{F}_{vh}|^2 \rangle & \langle \mathcal{F}_{vh}^* \mathcal{F}_{vv} \rangle' & -\langle \mathcal{F}_{vh}^* \mathcal{F}_{vv} \rangle'' \\ \langle |\mathcal{F}_{hv}|^2 \rangle & \langle |\mathcal{F}_{hh}|^2 \rangle & \langle \mathcal{F}_{hh}^* \mathcal{F}_{hv} \rangle' & -\langle \mathcal{F}_{hv} \mathcal{F}_{hh}^* \rangle'' \\ 2\langle \mathcal{F}_{vv} \mathcal{F}_{hv}^* \rangle' & 2\langle \mathcal{F}_{vh} \mathcal{F}_{hh}^* \rangle' & \langle \mathcal{F}_{vv} \mathcal{F}_{hh}^* + \mathcal{F}_{vh} \mathcal{F}_{hv}^* \rangle' & -\langle \mathcal{F}_{vv} \mathcal{F}_{hh}^* - \mathcal{F}_{vh} \mathcal{F}_{hv}^* \rangle' \\ 2\langle \mathcal{F}_{vv} \mathcal{F}_{hv}^* \rangle'' & 2\langle \mathcal{F}_{vh} \mathcal{F}_{hh}^* \rangle'' & \langle \mathcal{F}_{vv} \mathcal{F}_{hh}^* + \mathcal{F}_{vh} \mathcal{F}_{hv}^* \rangle'' & \langle \mathcal{F}_{vv} \mathcal{F}_{hh}^* - \mathcal{F}_{vh} \mathcal{F}_{hv}^* \rangle'' \end{bmatrix} \tag{3.55}$$

where the prime denotes the real part and double prime denotes the imaginary part. The quantity $\mathcal{F}_{\alpha\beta}$ $(\alpha, \beta = h, v)$ denotes the *incoherent* scattering amplitude from all particles in V with scattered field polarized in $\hat{\alpha}$-direction and incident field polarized in $\hat{\beta}$-direction. In the following, we provide numerically results for the elements $P_{vv} = \langle |\mathcal{F}_{vv}|^2 \rangle / V$, $P_{hv} = \langle |\mathcal{F}_{hv}|^2 \rangle / V$, $P_{hh} = \langle |\mathcal{F}_{hh}|^2 \rangle / V$, and $P_{vh} = \langle |\mathcal{F}_{vh}|^2 \rangle / V$ pertaining to coupling between first two Stokes parameter I_v and I_h. The incoherent scattering amplitude is obtained from Eq. (3.51) by subtracting out the coherent component $\langle F_{\alpha\beta} \rangle$.

The phase matrix elements will be presented in the y-z plane (i.e., $\phi_s = 90°$ and $270°$). We define the scattering angle Φ such that

$$\Phi = \begin{cases} \theta_s & \text{for } \phi_s = 90° \\ 360° - \theta_s & \text{for } \phi_s = 270° \end{cases} \tag{3.56}$$

where $0 \leq \theta_s \leq 180°$. Thus Φ varies from $0°$ to $360°$. Note that with the chosen incident wavevector direction $\hat{k}_i = \hat{y}$, $\Phi = 90°$ corresponds to the forward propagation direction and $\Phi = 270°$ corresponds to the backscattering direction. In Fig. 3-9, the phase matrix elements for aligned spheroids are shown. The most important

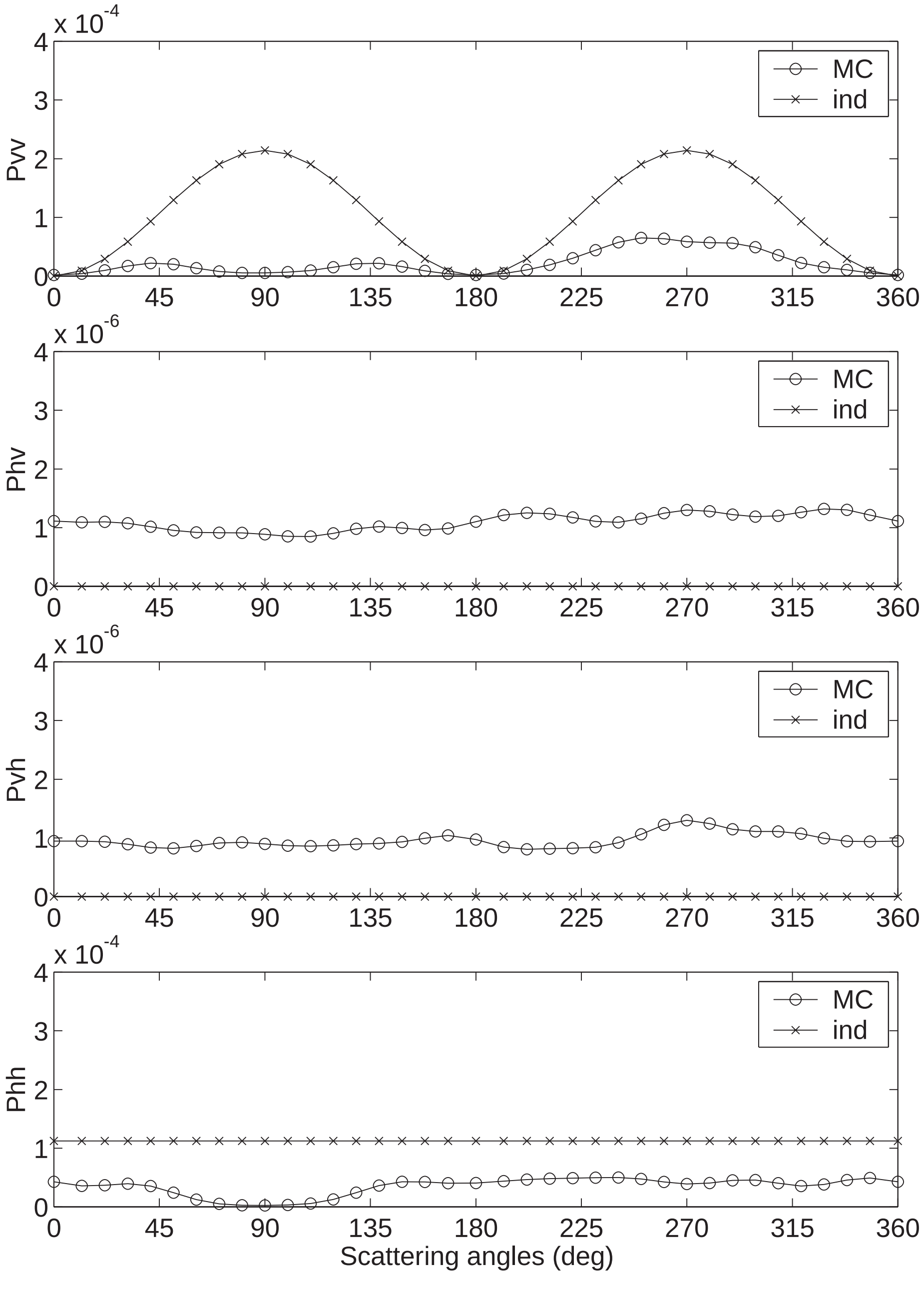

Figure 3-9: Phase matrix elements $P_{\alpha\beta}$ as a function of scattering angles for aligned spheroids. $ka = 0.2$, $f_v = 0.2$, and $\varepsilon_s = 3.2$. $N = 1000$ and 50 realizations are used.

feature from these curves is that for the co-polarized components (P_{vv} and P_{hh}), multiple scattering gives smaller values than independent scattering while the opposite is true for the cross-polarized components (P_{hv} and P_{vh}). In other words, *multiple scattering enhances depolarization*. For independent scattering, expressions for the phase matrix can be found in [64]. Independent scattering predicts that $P_{vv} \propto \sin^2 \Phi$ and $P_{hh} =$ constant while $P_{hv} = P_{vh} = 0$ in the y-z plane. The multiple scattering results show similar pattern except for two differences: (i) a broad "null" in the forward direction of $\Phi = 90°$ for the co-polarized components as a result of coherent wave subtraction and (ii) fluctuations that persist as a result of finite realization sampling. It is worth mentioning that the fluctuations appear worse for the cross-polarized components because their values are quite small. Similar conclusions can be reached based on Fig. 3-10, which shows the corresponding results for randomly oriented spheroids. In this case, independent scattering has nonzero P_{hv} and P_{vh}, but these are smaller than the multiple scattering values.

A direct consequence of these results is that any inference of geometric parameters which is based on polarimetric scattering measurements must take into account of multiple scattering effects when the scatterers are densely packed. Otherwise, one might conclude wrongly that the particles are more elongated than they actually are.

3.4.3 Absorption Coefficient

For lossy particles, the total extinction coefficient is a sum of the scattering coefficient and absorption coefficient. The absorption coefficient can be simulated by computing

$$\kappa_a = \frac{1}{V} \sum_{j=1}^{N} k\varepsilon_s'' \int d\overline{r}_j \langle |\overline{E}(\overline{r}_j)|^2 \rangle \tag{3.57}$$

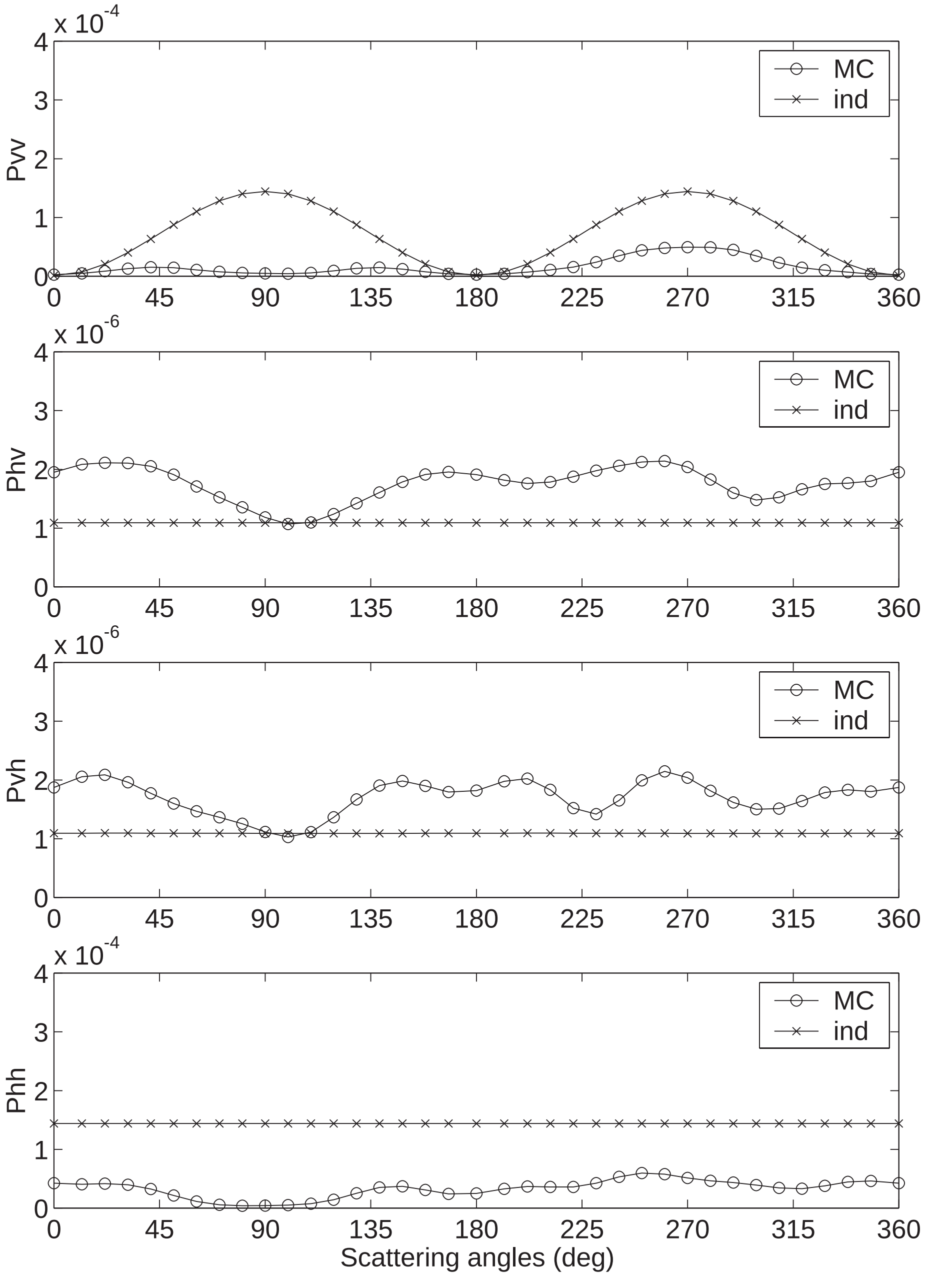

Figure 3-10: Phase matrix elements $P_{\alpha\beta}$ as a function of scattering angles for randomly oriented spheroids. $ka = 0.2$, $f_v = 0.2$, and $\varepsilon_s = 3.2$. $N = 1000$ and 50 realizations are used.

where $\varepsilon_s'' = \mathrm{Im}\{\varepsilon_s\}$ and the average internal field intensity is

$$\langle|\overline{E}(\overline{r}_j)|^2\rangle = \frac{1}{N_r}\sum_{\ell=1}^{N_r}\left|\sum_{\alpha=1}^{N_b} a_{j\alpha}^{(\ell)}\overline{f}_{j\alpha}(\overline{r}_j)\right|^2 \tag{3.58}$$

Making use of the orthonormality condition of the basis functions [Eq. (3.22)], the absorption coefficient can be expressed as:

$$\kappa_a = \frac{1}{N_r}\sum_{\ell=1}^{N_r}\left[\sum_{j=1}^{N}\sum_{\alpha=1}^{N_b}\frac{1}{V}k\varepsilon_s''|a_{j\alpha}^{(\ell)}|^2\right] \tag{3.59}$$

In Fig. 3-11, we show the absorption coefficient as a function of fractional volume f_v. Parameters are the same as in Fig. 3-7 except that $\varepsilon_s'' \neq 0$. In contrast to the scattering coefficient, the absorption coefficient increases monotonously with f_v. Moreover, multiple scattering enhances the absorption coefficient over independent scattering.

3.5 Nonuniform Induced Fields

For spheroids close to each other, nonuniform internal fields are induced inside the spheroids even though they are small compared to the wavelength. In this case, the point dipole approximation of (3.47) might no longer be accurate. In this section, we evaluate the accuracy of the point dipole approximation by calculating the interaction integrals exactly for pairs of spheroids that are close to each other.

Consider spheroids labeled l and j with center coordinates $\overline{r}_{cl}$ and $\overline{r}_{cj}$, respectively. We wish to compute the interaction integral given by (3.16).

$$A_{l\beta;j\alpha} = k^2\,[\varepsilon_s - 1]\int_v d\overline{r}_l \int_v d\overline{r}_j\ \overline{f}_{l\beta}(\overline{r}_l)\cdot\overline{\overline{G}}_o(\overline{r}_l,\overline{r}_j)\cdot\overline{f}_{j\alpha}(\overline{r}_j) \tag{3.60}$$

A neighborhood distance r_d is chosen such that when $|\overline{r}_l - \overline{r}_j| \geq r_d$, the point dipole approximation of (3.47) is used. However, when $|\overline{r}_l - \overline{r}_j| < r_d$, we compute $A_{l\beta;j\alpha}$

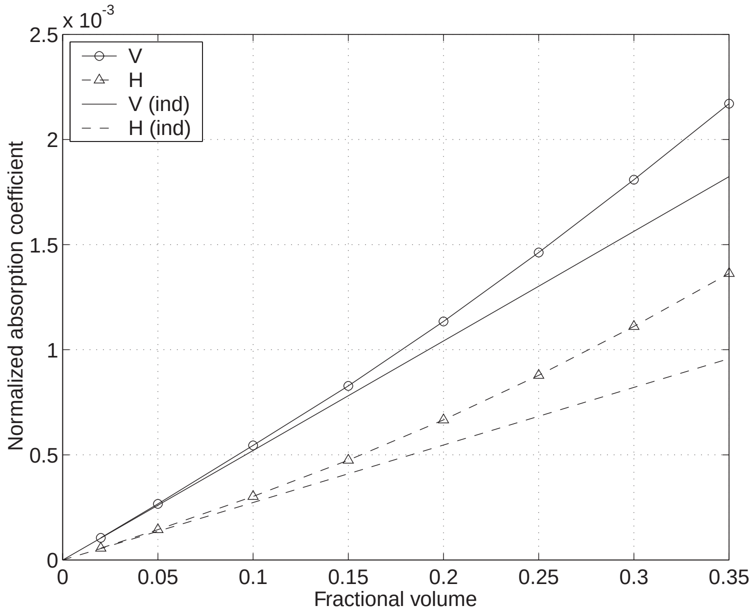

(a) Aligned case.

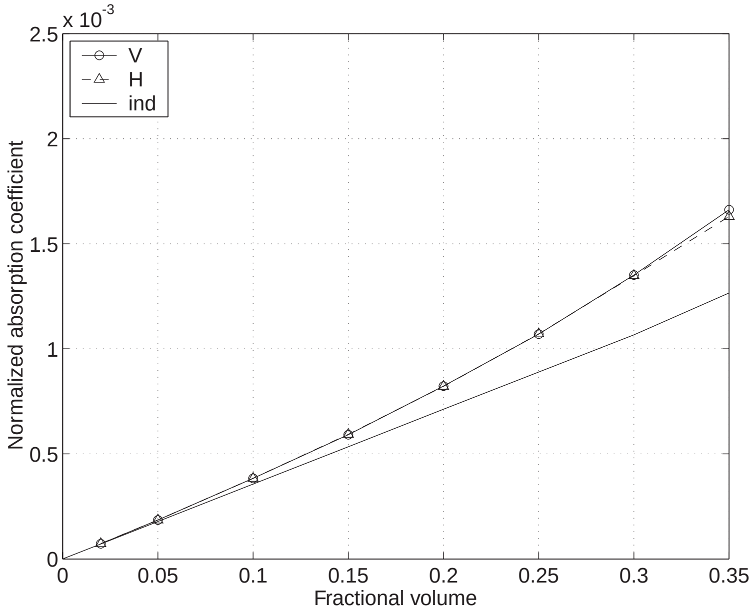

(b) Randomly oriented case.

Figure 3-11: Normalized absorption coefficient κ_a/k as a function of fractional volume f_v. $ka = 0.2$, $e = 2$, and $\varepsilon_s = 3.2 + i0.01$. $N = 1000$ and 50 realizations are used.

ka	f_v	with	without	difference (%)
0.2	0.2	3.548	3.612	1.77
0.2	0.3	3.174	3.333	4.75
0.3	0.2	9.562	9.750	1.92
0.3	0.3	7.563	7.936	4.70

Table 3.2: Normalized scattering coefficient κ_s/k with and without numerical integrations of matrix elements. Randomly oriented case.

ka	f_v	with	without	difference (%)
0.2	0.2	3.157	3.336	5.38
0.2	0.3	3.175	3.508	9.50
0.3	0.2	8.924	9.354	4.60
0.3	0.3	8.079	8.862	8.84

Table 3.3: Normalized scattering coefficient κ_s/k with and without numerical integrations of matrix elements. Aligned case with horizontal incident polarization.

exactly. The dipole basis functions of (3.44)–(3.46) are constant vectors and can be moved outside the integrals. Thus

$$A_{l\beta;j\alpha} = k^2 \left[\varepsilon_s - 1\right] \overline{f}_{l\beta} \cdot \overline{\overline{K}}_{lj} \cdot \overline{f}_{j\alpha} \tag{3.61}$$

where

$$\overline{\overline{K}}_{lj} \equiv \int_v d\overline{r}_l \int_v d\overline{r}_j \, \overline{\overline{G}}_o(\overline{r}_l, \overline{r}_j) \tag{3.62}$$

The sixfold integrations are performed numerically using Gauss-Legendre quadrature with 125 basis points for each of the two volume integrals.

Tables 3.2 and 3.3 show the comparison between results obtained using the point dipole interactions and using numerical integrations. The neighborhood distance is chosen to be $r_d = 3a$. Other parameters are: $e = 2$, $N = 1000$, and $N_r = 50$. The "difference" column in the tables is defined as

$$\delta\kappa_s = \frac{\kappa_s^{(wo)} - \kappa_s^{(w)}}{\kappa_s^{(wo)}} \tag{3.63}$$

where the subscripts (w) and (wo) denote cases with and without numerical integrations, respectively. Note that the scattering coefficients are smaller with numerical integrations for all the cases presented. Not surprisingly, numerical integrations affect the randomly oriented case less because the induced fields due to different spheroids are more randomized. The relative difference increases with fractional volume but changes little with when particle size is increased from $ka = 0.2$ to $ka = 0.3$.

The results in Tables 3.2 and 3.3 suggest that the point dipole approximations provide reasonably accurate scattering results. However, should accuracy of better than 5% be required, numerical integrations ought to be employed in calculating the matrix elements. It should be pointed out that this statement applies only to the hard spheroid distributions. In cases where clustering effects are important (e.g., particles with surface adhesion), a significantly larger number of close neighbors could be present. Thus the point dipole approximation might perform worse. In addition, the quadrupole basis functions should also be included.

3.6 Conclusions

In this chapter, we solve Maxwell's equations numerically for the multiple scattering of electromagnetic waves by dielectric spheroids. Recognizing the importance of particle positions on the collective scattering response, we first describe the Metropolis Monte Carlo method used to generate physically realistic configurations of hard prolate spheroids. Results of pair distribution functions show that the particle positions are far from uncorrelated. The correlation of particle positions affect the coherent addition of scattered waves from the spheroids. This fact is neglected in the independent scattering approximation which is widely used in the classical radiative transfer theory.

By formulating the problem in terms of volume integral equation for the electric field and assuming that the spheroidal particles have sizes small compared to the electromagnetic wavelength, a method of moment (MoM) solution is provided. In the MoM solution, the unknown electric field inside each spheroid is expanded in terms of electrostatic multipole basis functions. Using Galerkin's method, a matrix equation for the unknown expansion coefficients is constructed. Special care must be exercised in calculating the diagonal elements due to the source-region singularity in the dyadic Green's function. We derive these so-called self-patch terms by using a low-frequency expansion of the dyadic Green's function. It is shown that the leading real part comes from the singular part of the Green's function, while the leading imaginary part comes from the regular part. The leading imaginary part is much smaller than the leading real part for small particles; however, they account for the radiative loss as the wave is scattered away from the forward propagation direction. Thus it needs to be included to preserve energy conservation.

The most important basis functions for small spheroids are the three electric dipoles. Thus we include only the dipoles in the numerical calculations presented in this chapter. Moreover, in order to compute the interaction matrix elements quickly, we assume that the induced field is uniform within the spheroid and is equal to its value at the center of the spheroid. Using this point dipole approximation, we solve the multiple scattering equations for a large number of spheroids generated using the Metropolis Monte Carlo method. The scattering results are averaged over many realizations and presented in terms of scattering coefficient, scattering phase matrix, and absorption coefficient. These are important input physics parameters for equations for describing radiative transport in a random medium. We compare the simulation results with those obtained under the assumption of independent scattering. It is found that for appreciable fractional volume ($f_v \gtrsim 5\%$), the independent approximation overestimates the scattering coefficient and underestimates the absorption coefficient. The discrepancy also tends to increase as a function of elongation ratio. Examination of the phase matrix elements shows that depolarization effects become more significant as a result of multiple scattering. This has important implication for any attempt to deduce particle shape based on depolarization measurements.

Instead of using the point dipole approximation, one could evaluate the interaction matrix elements exactly by numerical integrations for pairs of spheroids that are close to each other. As expected, the point dipole approximation is worse at higher fractional volume and for spheroids in aligned orientation. However, overall, it gives fairly accurate scattering coefficients and is superior in terms of computational efficiency.

Throughout this chapter, we present results for spheroids that are randomly oriented and spheroids that have aligned orientations. Other orientation distribution can be considered by a simple modification of the shuffling procedure. This kind of generality in scattering configurations represents one of the great strengths of Monte Carlo simulations. In the next chapter, we solve the problem of multiple scattering of spheroids using analytical approximations. However, the discussion will be limited to spheroids in aligned configurations. The difficulty in tackling the more general problem of arbitrary orientation distribution is that analytical expressions of the pair distribution function, which is a crucial ingredient in multiple scattering theories, are not readily available. Thus numerical simulations provide the best way to solve these problems.

Chapter 4

Analytical Approximations in Multiple Scattering by Aligned Dielectric Spheroids

4.1 Introduction

In Chapter 3, we studied multiple scattering by dielectric spheroids numerically using Monte Carlo simulations. By packing many spheroids and averaging over many realizations, we were able to simulate important radiative transport quantities such as the extinction coefficient, absorption coefficient, and scattering phase matrix. The simulation results show that for appreciable fractional volume, the commonly used approximation of independent scattering is no longer valid. However, while Monte Carlo simulations have proven to be extremely useful, they are computationally demanding and do not lead to simple relations between the various parameters. Thus in this chapter, we study the problem using the multiple scattering theories of quasi-crystalline approximation (QCA) and quasi-crystalline approximation with coherent potential (QCA-CP) [7, 14]. These approximations have shown to be accurate for scattering by dielectric spheres [37, 38] and will be extended here to the case of dielectric spheroids. Multiple scattering of nonspherical particles using QCA has been considered in the past by Twersky with his multiple-scattered field formulation [65, 6] and by Tsang [66] as well as Varadan *et al.* [67, 68] using the T-matrix (i.e., spherical wave expansion) formulation. The work here differs in that a rigorous operator formalism is used, which allows for the inclusion of the coherent potential.

One of the most important consequences of multiple scattering in discrete random medium is that the scattering and absorption proprieties of the medium depend crucially on the joint probability distribution of the particle positions. In particular, the pair distribution function, which is proportional to the two-particle joint probability distribution, is required in many multiple scattering theories. In the study of multiple scattering by spheres, it has been recognized that unphysical prescription of the pair distribution function (e.g., the hole approximation) could lead to disastrous results when the fractional volume of the particles is appreciable [8].

The pair distribution function can be found analytically by solving the Percus-Yevick (PY) integral equation, which is an approximation for the Ornstein-Zernike equation [69]. For spherical particles interacting via the hard-sphere potential, a closed-form solution can be obtained [70, 71, 72]. This is the celebrated Percus-Yevick pair distribution function for hard spheres and provides a simple way to incorporate physically realistic pair statistics into multiple scattering models. Unfortunately, for more general interaction potentials and particle shapes, the PY pair distribution function cannot be obtained without solving the integral equation. Monte Carlo simulations using the Metropolis shuffling method described in Chapter 3 or molecular dynamics simulations are often the best way to compute the statistical mechanical properties of the particles [56, 73]. As we have seen in Chapter 3, it is relatively straightforward to calculate the pair distribution function based on Metropolis shuffling. However, for scattering calculations, we actually need the structure factor, which is related to the Fourier transform of the pair distribution function. Due to the fluctuating nature of the pair distribution function, it can be difficult to obtain a very accurate structure factor from Monte Carlo methods.

A simple nonspherical system where the PY pair distribution function is available in closed form consists of hard ellipsoids that have aligned orientation but random positions. This is because the aligned ellipsoid problem can be easily mapped into the sphere problem via a simple coordinate transformation [74]. Since spheroid represents a special case of an ellipsoid, we have in our disposal an analytical pair distribution function for multiple scattering by aligned spheroids. Thus in this chapter, we consider only scattering by spheroids in aligned configuration.

The rest of this chapter proceeds as follows. In Sec. 4.2, we discuss briefly the PY pair distribution function for aligned hard ellipsoids. In Sec. 4.3, we present the multiple scattering formulation in operator notation. The method of conditional averaging is applied to the multiple scattering equations which allow for the imposition of QCA and QCA-CP. The QCA and QCA-CP equations can be readily solved in closed-form in low-frequency (or small particle size) limit. In Sec. 4.4, we derive the average Green's function and effective medium characteristics from QCA and QCA-CP in such a limit. In Sec. 4.5, we compare the effective permittivity obtained using QCA and QCA-CP with the Maxwell-Garnett mixing formula. In Sec. 4.6, extensive comparisons are made with the Monte Carlo simulation results obtained using the methods of Chapter 3. Conclusions to this chapter can be found in Sec. 4.7.

4.2 Percus-Yevick Pair Distribution Function

The pair distribution function $g(\overline{r})$ is proportional to the two-particle probability distribution function and has been discussed in Sec. 3.2.2. Consider aligned ellipsoids with interparticle potential $u(\overline{r})$. The only dependence of the pair distribution function is on the separation vector $\overline{r}$ between the centers of the two ellipsoids.

It is common to define the total correlation function $h(\overline{r})$ as

$$h(\overline{r}) = g(\overline{r}) - 1 \tag{4.1}$$

The Ornstein-Zernike (OZ) equation *defines* the direct correlation function $c(\overline{r})$ in terms of the total correlation function $h(\overline{r})$ [54]:

$$h(\overline{r}) = c(\overline{r}) + n_o \int d\overline{r}' c(\overline{r}') h(\overline{r} - \overline{r}') \tag{4.2}$$

where $n_o = N/V$ is the number density of the particles. In words, the OZ equation states that the total correlation of two particles is the sum of the direct correlation and the indirect correlation function, which is a convolution integral of the total and direct correlation functions.

To introduce the Percus-Yevick (PY) approximation, let

$$g(\overline{r}) = y(\overline{r}) \exp\left[-\beta u(\overline{r})\right] \tag{4.3}$$

where $\beta = 1/k_B T$. Thus $h(\overline{r})$ is related to $y(\overline{r})$ through Eqs. (4.1) and (4.3). The PY approximation is [69]

$$h(\overline{r}) - c(\overline{r}) = y(\overline{r}) - 1 \tag{4.4}$$

and relates the direct correlation function to $y(\overline{r})$. This allows us to turn the OZ equation into an integral equation for $y(\overline{r})$ only. For hard spheres, the PY integral equation can be solved in closed form [70, 71, 72].

For hard ellipsoids, the interparticle potential is

$$u(\overline{r}) = \begin{cases} \infty & \text{for } P < 1 \\ 0 & \text{for } P > 1 \end{cases} \tag{4.5}$$

where $P^2 = \overline{r}^T \overline{\overline{A}}^2 \overline{r}$ and $\overline{\overline{A}} = \mathrm{diag}[1/a, 1/b, 1/c]$ with a, b, c being the semiaxes of the ellipsoid. Let [74]

$$\overline{R} = \overline{\overline{A}}\,\overline{r}, \quad \overline{R}' = \overline{\overline{A}}\,\overline{r}' \tag{4.6}$$

Then (4.2) transforms to

$$h(\overline{R}) = c(\overline{R}) + \frac{3}{4\pi} f_v \int d\overline{R}' c(\overline{R}') h(\overline{R} - \overline{R}') \tag{4.7}$$

where $f_v = n_o(4\pi/3)abc$ is the fractional volume occupied by the ellipsoids. More importantly, under this transformation, the hard ellipsoid potential now becomes the hard sphere potential:

$$u(\overline{R}) = \begin{cases} \infty & \text{for } R < 1 \\ 0 & \text{for } R > 1 \end{cases} \tag{4.8}$$

Thus the pair distribution function $g(\overline{R}) = g(R) = h(R) + 1$ is identical to that of a hard sphere system with the same fractional volume (with radial distance normalized by its diameter). Plots of the pair distribution function for hard spheroids can be found in Chapter 3, where they are shown to agree very well with Monte Carlo simulations.

In analytical scattering calculations, it is often not the pair distribution function but its Fourier transform that appears directly in the final expressions. We define the structure factor

$$S(\overline{p}) = 1 + n_o H(\overline{p}) \tag{4.9}$$

where

$$\overline{H}(\overline{p}) = \int d\overline{r} e^{-i\overline{p}\cdot\overline{r}} h(\overline{r}) \tag{4.10}$$

is the Fourier transform of the total correlation function. From the PY solution for hard spheres, the structure factor at $p = 0$ is given by

$$S_o \equiv S(0) = \frac{(1 - f_v)^4}{(1 + 2f_v)^2} \tag{4.11}$$

Anisotropy features in the structure factor of aligned hard ellipsoids only arise at

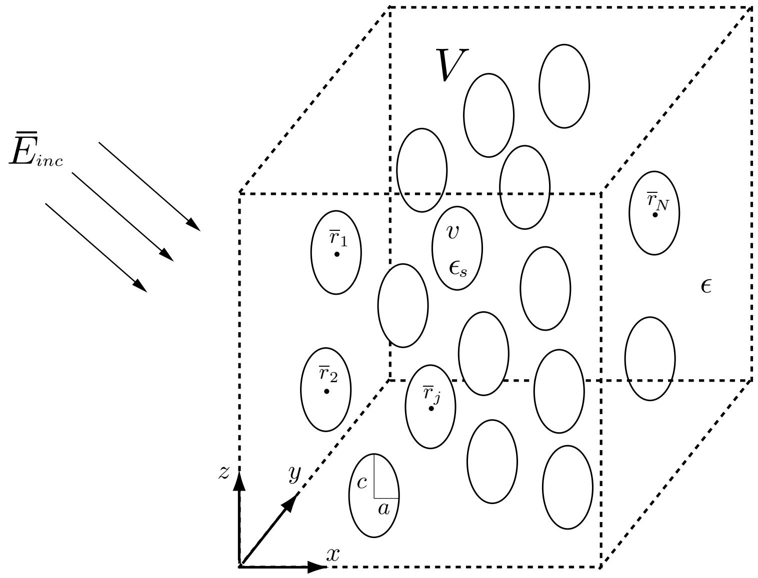

Figure 4-1: Scattering of electromagnetic waves by densely packed aligned prolate spheroids. The symmetry axis of the spheroid is chosen to be in the $\hat{z}$-direction.

nonzero frequencies [74].

4.3 Multiple Scattering Formulation

In this section, we discuss the formulation for the multiple scattering of waves by aligned dielectric spheroids (Fig. 4-1). The operator notation of Tsang and Kong [7, 14], which has its root in quantum mechanical scattering formulation, will be adopted here. Detailed derivation on the multiple scattering formulation presented in this section can be found in [75, 14].

First consider a single spheroid with center at $\overline{r}_j$. The dielectric constants of the scatterer and the background are ϵ_s and ϵ_o, respectively. The single-particle Green's function $\overline{\overline{G}}_s$ satisfies the following integral equation

$$\overline{\overline{G}}_s(\overline{r},\overline{r}') = \overline{\overline{G}}_o(\overline{r},\overline{r}') + \int d\overline{r}''\,\overline{\overline{G}}_o(\overline{r},\overline{r}')U(\overline{r}''-\overline{r}_j)\overline{\overline{G}}_s(\overline{r}'',\overline{r}') \tag{4.12}$$

where $\overline{\overline{G}}_o(\overline{r}, \overline{r}')$ is the background Green's function, $k^2 = \omega^2\epsilon_o\mu_o$, and $k_s^2 = \omega^2\epsilon_s\mu_o$. The scattering potential $U(\overline{r})$ is defined as

$$U(\overline{r} - \overline{r}_j) = \begin{cases} k_s^2 - k^2 & \text{for } P_j < 1 \text{ (inside spheroid)} \\ 0 & \text{otherwise (outside spheroid)} \end{cases} \tag{4.13}$$

where $P_j^2 = (\overline{r} - \overline{r}_j)^T \overline{\overline{A}}^2 (\overline{r} - \overline{r}_j)$ and $\overline{\overline{A}} = \text{diag}[1/a, 1/a, 1/c]$.

In operator notation, Eq. (4.12) can be written succinctly as

$$\overline{\overline{G}}_s = \overline{\overline{G}}_o + \overline{\overline{G}}_o \overline{\overline{U}}_j \overline{\overline{G}}_s \tag{4.14}$$

where in coordinate representation, $\langle \overline{r} | \overline{\overline{U}}_j | \overline{r}' \rangle = U(\overline{r} - \overline{r}_j)\delta(\overline{r} - \overline{r}')\overline{\overline{I}}$. It is convenient to define the transition operator $\overline{\overline{T}}_j$ such that $\overline{\overline{U}}_j \, \overline{\overline{G}}_s = \overline{\overline{T}}_j \, \overline{\overline{G}}_o$. Then it follows from Eq. (4.14) that

$$\overline{\overline{G}}_s = \overline{\overline{G}}_o + \overline{\overline{G}}_o \, \overline{\overline{T}}_j \, \overline{\overline{G}}_o \tag{4.15}$$

and

$$\overline{\overline{T}}_j = \overline{\overline{U}}_j + \overline{\overline{U}}_j \, \overline{\overline{G}}_o \overline{\overline{T}}_j \tag{4.16}$$

which can be solved formally as

$$\overline{\overline{T}}_j = (\overline{\overline{I}} - \overline{\overline{U}}_j \, \overline{\overline{G}}_o)^{-1} \overline{\overline{U}}_j \tag{4.17}$$

Eq. (4.16) is known as the Lippmann-Schwinger equation. Once the transition operator is found using the Lippmann-Schwinger equation, the single-particle scattering problem is considered to be solved.

We next consider the multiple scattering problem for N randomly positioned spheroids with the same orientation. The N-particle Green's function $\overline{\overline{G}}$ satisfies the equation

$$\overline{\overline{G}} = \overline{\overline{G}}_o + \overline{\overline{G}}_o \sum_{j=1}^{N} \overline{\overline{U}}_j \overline{\overline{G}} \tag{4.18}$$

One can define the "exciting field" Green's function $\overline{\overline{G}}_l$ for particle l by excluding the $j = l$ term in the sum above. This gives

$$\overline{\overline{G}}_l = \overline{\overline{G}}_o + \overline{\overline{G}}_o \sum_{j=1, j \neq l}^{N} \overline{\overline{U}}_j \overline{\overline{G}} \tag{4.19}$$

Note that $\overline{\overline{G}}_l$, unlike $\overline{\overline{U}}_l$ and $\overline{\overline{T}}_j$, depends on the the configurations of all N particles. Eq. (4.18) can then be written as

$$\overline{\overline{G}} = \overline{\overline{G}}_j + \overline{\overline{G}}_o \overline{\overline{U}}_j \overline{\overline{G}} \tag{4.20}$$

Using (4.17) and (4.20), it can be inferred that $\overline{\overline{U}}_j \, \overline{\overline{G}} = \overline{\overline{T}}_j \, \overline{\overline{G}}_j$. Then (4.18) and (4.19) give

$$\overline{\overline{G}} = \overline{\overline{G}}_o + \overline{\overline{G}}_o \sum_{j=1}^{N} \overline{\overline{T}}_j \overline{\overline{G}}_j \tag{4.21}$$

$$\overline{\overline{G}}_j = \overline{\overline{G}}_o + \overline{\overline{G}}_o \sum_{l=1, l \neq j}^{N} \overline{\overline{T}}_l \overline{\overline{G}}_l \tag{4.22}$$

which are the Foldy-Lax multiple scattering equations in operator form. The multiple scattering equations as given in (4.21) and (4.22) can be used to solve for $\overline{\overline{G}}_j$ and $\overline{\overline{G}}$ given the the configurations of all N spheroids. This is the approach taken in numerical simulations. In analytical treatments, we are interested in the average properties from a statistical ensemble of such scatterers, and it would be best to derive the equations for the average Green's function directly.

Let $E(\overline{\overline{O}})$ denote the ensemble average of $\overline{\overline{O}}$, $E_j(\overline{\overline{O}})$ denote the ensemble average with particle j fixed, $E_{jl}(\overline{\overline{O}})$ denote the ensemble average with particles j and l fixed, etc. Then, taking ensemble averaging of (4.21) and the ensemble average of (4.22) with particle j fixed give

$$E(\overline{\overline{G}}) = \overline{\overline{G}}_o + N\overline{\overline{G}}_o E(\overline{\overline{T}}_j E_j(\overline{\overline{G}}_j)) \tag{4.23}$$

$$E_j(\overline{\overline{G}}_j) = \overline{\overline{G}}_o + (N-1)\overline{\overline{G}}_o E_j(\overline{\overline{T}}_j E_{jl}(\overline{\overline{G}}_j)) \quad (j \neq l) \tag{4.24}$$

Note that the second equation depends on the ensemble average of $\overline{\overline{G}}_j$ with j and l fixed. Thus these two equations alone are not sufficient to determine the average Green's function. In principle, we need to take the ensemble average of (4.22) with two particles fixed, which would in turn depend on the ensemble average with three particles fixed, and so on. Thus the conditional averaging procedure introduces a hierarchy of equations which must all be included to yield a complete set of equations and unique solutions. To provide closure condition without resorting to higher hierarchy of equations, various approximations can be introduced. The simplest one is the Foldy's approximation, which set the ensemble average with one particle fixed to the ensemble average with no particle fixed:

$$E_j(\overline{\overline{G}}_j) = E(\overline{\overline{G}}) \tag{4.25}$$

Using this in (4.23) gives an equation for $E(\overline{\overline{G}})$. Note that Eq. (4.24) is not needed in the Foldy's approximation. However, Foldy's approximation does not take into account of correlation of the particle configurations and is not valid at higher fractional volumes. A better approximation, which is due to Lax [76], involves a higher order closure condition. This is the quasi-crystalline approximation (QCA).

4.3.1 Quasi-Crystalline Approximation (QCA)

To introduce QCA, first recast the Foldy-Lax equations in an alternate form by defining $\overline{\overline{Q}}_j\overline{\overline{G}}_o = \overline{\overline{T}}_j\overline{\overline{G}}_j$. Then (4.21) and (4.22) become

$$\overline{\overline{G}} = \overline{\overline{G}}_o + \overline{\overline{G}}_o \sum_{j=1}^{N} \overline{\overline{Q}}_j \overline{\overline{G}}_o \tag{4.26}$$

$$\overline{\overline{Q}}_j = \overline{\overline{T}}_j + \overline{\overline{T}}_j \overline{\overline{G}}_o \sum_{l=1, l\neq j}^{N} \overline{\overline{Q}}_l \tag{4.27}$$

Upon averaging:

$$E(\overline{\overline{G}}) = \overline{\overline{G}}_o + N\overline{\overline{G}}_o E(E_j(\overline{\overline{Q}}_j))\overline{\overline{G}}_o \tag{4.28}$$

$$E_j(\overline{\overline{Q}}_j) = \overline{\overline{T}}_j + (N-1)\overline{\overline{T}}_j\overline{\overline{G}}_o E_j(E_{jl}(\overline{\overline{Q}}_l)) \quad (j \neq l) \tag{4.29}$$

QCA specifies that the conditional average holding two particles fixed is approximately equal to the conditional average holding one particle fixed. Thus

$$E_{jl}(\overline{\overline{Q}}_l) \approx E_l(\overline{\overline{Q}}_l) \tag{4.30}$$

Then (4.29) becomes

$$E_j(\overline{\overline{Q}}_j) = \overline{\overline{T}}_j + (N-1)\overline{\overline{T}}_j\overline{\overline{G}}_o E_j(E_l(\overline{\overline{Q}}_l)) \tag{4.31}$$

which provides an equation for $E_j(\overline{\overline{Q}}_j)$. An integral equation can be obtained in the momentum representation.

After ensemble averaging with particle j fixed, $E_j(\overline{\overline{Q}}_j)$ depends only on the position of the spheroid j. Moreover, the medium is statistically translationally invariant, which implies that in the momentum representation,

$$\langle \overline{p} | E_j(\overline{\overline{Q}}_j) | \overline{p}' \rangle = \overline{\overline{Q}}(\overline{p}, \overline{p}')\, e^{-i(\overline{p}-\overline{p}')\cdot \overline{r}_j} \tag{4.32}$$

$$\langle \overline{p}|\overline{\overline{T}}_j|\overline{p}'\rangle = \overline{\overline{T}}(\overline{p},\overline{p}')\, e^{-i(\overline{p}-\overline{p}')\cdot\overline{r}_j} \tag{4.33}$$

where $\overline{\overline{Q}}(\overline{p},\overline{p}')$ and $\overline{\overline{T}}(\overline{p},\overline{p}')$ are independent of $\overline{r}_j$. Thus in the momentum representation, (4.31) becomes

$$\begin{aligned}\overline{\overline{Q}}(\overline{p},\overline{p}') = \overline{\overline{T}}(\overline{p},\overline{p}') + (N-1)\int d\overline{r}_l\; p(\overline{r}_l|\overline{r}_j)\\ \int \frac{d\overline{p}''}{(2\pi)^3} e^{-i(\overline{p}''-\overline{p}')\cdot(\overline{r}_l-\overline{r}_j)}\overline{\overline{T}}(\overline{p},\overline{p}'')\overline{\overline{G}}_o(\overline{p}'')\overline{\overline{Q}}(\overline{p}'',\overline{p}')\end{aligned} \tag{4.34}$$

By relating the conditional probability to the pair distribution function [Eq. (3.2)]

$$p(\overline{r}_l|\overline{r}_j) = \frac{1}{V}\frac{N}{N-1}g(\overline{r}_l-\overline{r}_j) \tag{4.35}$$

Eq. (4.34) can be written as

$$\overline{\overline{C}}(\overline{p},\overline{p}') = \overline{\overline{T}}(\overline{p},\overline{p}') + n_o\int \frac{d\overline{p}''}{(2\pi)^3}H(\overline{p}''-\overline{p}')\overline{\overline{T}}(\overline{p},\overline{p}'')\overline{\overline{G}}_o(\overline{p}'')\overline{\overline{C}}(\overline{p}'',\overline{p}') \tag{4.36}$$

where $n_o = N/V$ is the number density of the spheroids, $H(\overline{p})$ is defined in (4.10), and

$$\overline{\overline{C}}(\overline{p},\overline{p}') \equiv \overline{\overline{Q}}(\overline{p},\overline{p}')\left[\overline{\overline{I}} + n_o\overline{\overline{G}}_o(\overline{p}')\overline{\overline{Q}}(\overline{p}',\overline{p}')\right]^{-1} \tag{4.37}$$

From (4.28), the average Green's function in momentum representation is given by

$$\overline{\overline{G}}(\overline{p}) = \left[\overline{\overline{G}}_o^{-1}(\overline{p}) - n_o\overline{\overline{C}}(\overline{p},\overline{p})\right]^{-1} \tag{4.38}$$

Thus the average Green's function differs from the background Green's function by the addition of the second term on the right hand side. The dispersion relation of the effective medium corresponds to the poles of the average Green's function. This can be done by solving the following determinant equation:

$$\det\left[\overline{\overline{G}}_o^{-1}(\overline{p}) - n_o\overline{\overline{C}}(\overline{p},\overline{p})\right] = 0 \tag{4.39}$$

The term $n_o\overline{\overline{C}}$ is sometimes referred to as the mass operator.

Note that for the homogeneous and isotropic background, the Green's function has the following form in the spectral domain [see Appendix C]:

$$\overline{\overline{G}}_o^{-1}(\overline{p}) = (p^2 - k^2)\overline{\overline{I}} - \overline{p}\,\overline{p} \tag{4.40}$$

4.3.2 Quasi-Crystalline Approximation with Coherent Potential (QCA-CP)

The coherent potential (CP) concept can be introduced to renormalize the multiple scattering solution obtained previously. The basic idea behind CP is that as multiple scattering becomes more important, the coherent wave "sees" more of the average medium than the background medium. The method was first used to study electron in disordered metals [77] and later applied to systems with short-range correlations by making use of QCA [78, 79]. QCA-CP was first applied to electromagnetic scattering by Tsang and Kong [7].

We start with Eq. (4.18) for the N-particle Green's function, which can be re-expressed as

$$\left[\overline{\overline{G}}_o^{-1} - \sum_{j=1}^{N}\overline{\overline{U}}_j\right]\overline{\overline{G}} = \overline{\overline{I}} \tag{4.41}$$

The coherent potential operator $\overline{\overline{w}}$ is introduced such that

$$\overline{\overline{\widehat{G}}}_o^{-1} = \overline{\overline{G}}_o^{-1} - n_o\overline{\overline{w}} \tag{4.42}$$

$$\overline{\overline{\widehat{U}}}_j = \overline{\overline{U}}_j - \frac{1}{V}\overline{\overline{w}} \tag{4.43}$$

Then Eq. (4.41) takes the form

$$\left[\overline{\overline{\widehat{G}}}_o^{-1} - \sum_{j=1}^{N}\overline{\overline{\widehat{U}}}_j\right]\overline{\overline{G}} = \overline{\overline{I}} \tag{4.44}$$

which is the same as in (4.41) except that $\overline{\overline{G}}_o^{-1} \to \overline{\overline{\widehat{G}}}_o^{-1}$ and $\overline{\overline{U}}_j \to \overline{\overline{\widehat{U}}}_j$. Thus much of the derivation shown in the previous section can be repeated with the modified background Green's function and modified scattering potential. The CP operator $\overline{\overline{w}}$ is chosen from the self-consistent condition that

$$E(\overline{\overline{G}}) = \overline{\overline{\widehat{G}}}_o \tag{4.45}$$

If we now apply QCA to the modified multiple scattering equations, the average Green's function takes the form

$$\overline{\overline{G}}(\overline{p}) = \left[\overline{\overline{G}}_o^{-1}(\overline{p}) - n_o\overline{\overline{\widehat{C}}}(\overline{p},\overline{p})\right]^{-1} \tag{4.46}$$

where the mass term $n_o\overline{\overline{\widehat{C}}}(\overline{p},\overline{p})$ now depends on the average Green's function. It can be shown that [75, 14]

$$\overline{\overline{\widehat{C}}}(\overline{p},\overline{p}') = \overline{\overline{\hat{t}}}_j(\overline{p},\overline{p}') + n_o \int \frac{d\overline{p}''}{(2\pi)^3} H(\overline{p}''-\overline{p}')\overline{\overline{\hat{t}}}(\overline{p},\overline{p}'')\overline{\overline{G}}(\overline{p}'')\overline{\overline{\widehat{C}}}(\overline{p}'',\overline{p}') \tag{4.47}$$

Single-particle scattering in the renormalized medium is characterized by the modified transition operator $\overline{\overline{\hat{t}}}_j$, which obeys the modified Lippmann-Schwinger equation:

$$\overline{\overline{\hat{t}}}_j = \overline{\overline{U}}_j + \overline{\overline{U}}_j E(\overline{\overline{G}})\overline{\overline{\hat{t}}}_j \tag{4.48}$$

Eqs. (4.46)–(4.48) represent coupled nonlinear equations with which the average Green's function can be solved.

4.4 Low-Frequency Dispersion Relation

The derivation above shows that even with QCA and QCA-CP, an integral equation for the mass term must be solved in order to find the average Green's function. In general, this must be done numerically. However, in the low-frequency limit, it is possible to obtain closed-form solutions for both QCA and QCA-CP.

The solution strategy proceeds as follows. For QCA, we first obtain the transition operator for a single spheroid using the Lippmann-Schwinger equation of Eq. (4.16). Then the mass term $n_o\overline{\overline{C}}(\overline{p}, \overline{p}')$ is solved using (4.36). The average Green's function is deduced from (4.38). For QCA-CP, we obtain the modified transition operator from Eq. (4.48) and the mass term in terms of the average Green's function from Eq. (4.47). This results in a nonlinear algebraic equation for the average Green's function.

4.4.1 QCA

To find the transition operator, consider a single spheroid with its center at the origin. Consider a mixed representation of $\overline{\overline{T}}$ [80]. Let

$$\overline{\overline{T}}_m(\overline{r}, \overline{p}) = \langle \overline{r} | \overline{\overline{T}} | \overline{p} \rangle \tag{4.49}$$

In the low-frequency limit, $\overline{p} \to 0$ so let $\overline{\overline{T}}_m(\overline{r}) = \overline{\overline{T}}_m(\overline{r}, \overline{p} = 0)$. Then taking the mixed representation of (4.16) gives

$$\overline{\overline{T}}_m(\overline{r}) = U(\overline{r})\overline{\overline{I}} + U(\overline{r}) \int d\overline{r}' \overline{\overline{G}}_o(\overline{r}, \overline{r}') \overline{\overline{T}}_m(\overline{r}') \tag{4.50}$$

The dyadic Green's function can be written with its singularity at $\overline{r} = \overline{r}'$ extracted based on an exclusion volume of spheroidal shape [59]. In the low-frequency limit, keeping the leading real and imaginary parts gives [9]

$$\overline{\overline{G}}_o(\overline{r}, \overline{r}') = -\frac{\overline{\overline{L}}}{k^2} \delta(\overline{r} - \overline{r}') + \frac{ik}{6\pi} \overline{\overline{I}} \tag{4.51}$$

where

$$\overline{\overline{L}} = L_a \hat{x}\hat{x} + L_a \hat{x}\hat{x} + L_c \hat{z}\hat{z} \tag{4.52}$$

The depolarization factors L_a and L_c for prolate spheroids are given in conventional form as follows [44, 28]:

$$L_c = -\frac{(1-\tilde{e}^2)}{\tilde{e}^2}\left[1+\frac{1}{2\tilde{e}}\ln\left(\frac{1-\tilde{e}}{1+\tilde{e}}\right)\right] \tag{4.53}$$

$$L_a = \frac{1}{2}(1-L_c) \tag{4.54}$$

where

$$\tilde{e} = \sqrt{1-\frac{a^2}{c^2}} \tag{4.55}$$

is the eccentricity. (The notation $\tilde{e}$ is used to distinguish the eccentricity from the elongation ratio $e = c/a$.) In fact, we have already derived the depolarization factors in Chapter 3 under the disguise of self-patch coefficient for dipoles [cf. real parts of Eqs. (B.21) and (B.22) without the factor $(\varepsilon_s - 1)$ and with the substitution $\xi_o = 1/\tilde{e}$].

Putting Eq. (4.51) into (4.50) and letting

$$\overline{\overline{T}}_m(\overline{r}) = \begin{cases} \overline{\overline{T}}_o, & \overline{r} \text{ inside spheroid} \\ 0, & \overline{r} \text{ outside spheroid} \end{cases} \tag{4.56}$$

where $\overline{\overline{T}}_o$ is a constant dyad, we obtain

$$\overline{\overline{T}}_o = \left[\left(\frac{1}{k_s^2-k^2}\overline{\overline{I}} + \frac{1}{k^2}\overline{\overline{L}}\right) - \frac{ikv}{6\pi}\overline{\overline{I}}\right]^{-1} \tag{4.57}$$

with

$$\overline{\overline{\eta}} = \frac{1}{3}(k_s^2-k^2)\left[k^2\overline{\overline{I}} + (k_s^2-k^2)\overline{\overline{L}}\right]^{-1} \tag{4.58}$$

Then to leading order in real and imaginary parts,

$$\overline{\overline{T}}_o = 3k^2\overline{\overline{\eta}}\left[\overline{\overline{I}} + \frac{ik^3v}{2\pi}\overline{\overline{\eta}}\right] \tag{4.59}$$

The momentum representation of the transition operator is given by

$$\overline{\overline{T}}(\overline{p},\overline{p}') = \int d\overline{r} e^{-i\overline{p}\cdot\overline{r}} \overline{\overline{T}}_m(\overline{r},\overline{p}') \approx v\overline{\overline{T}}_o \tag{4.60}$$

where the last relation follows in the low-frequency limit.

Using (4.60) in (4.36), we get

$$\overline{\overline{C}}(\overline{p},\overline{p}') = v_o\overline{\overline{T}}_o + f_v\overline{\overline{T}}_o \int \frac{d\overline{p}''}{(2\pi)^3} H(\overline{p}''-\overline{p}')\overline{\overline{G}}_o(\overline{p}'')\overline{\overline{C}}(\overline{p}'',\overline{p}') \tag{4.61}$$

We solve for (4.61) by letting

$$\overline{\overline{C}}(\overline{p},\overline{p}') = \overline{\overline{C}}_o \tag{4.62}$$

where $\overline{\overline{C}}_o$ is independent of $\overline{p},\overline{p}'$ in the low-frequency limit. Then (4.61) becomes

$$\overline{\overline{C}}_o(\overline{p}') = \left[\overline{\overline{I}} - f_v\overline{\overline{T}}_o \int \frac{d\overline{p}''}{(2\pi)^3} H(\overline{p}'')\overline{\overline{G}}_o(\overline{p}'')\right]^{-1} v\overline{\overline{T}}_o \tag{4.63}$$

Using (4.51), it follows that

$$\int \frac{d\overline{p}''}{(2\pi)^3} H(\overline{p}'')\overline{\overline{G}}_o(\overline{p}'') = \frac{1}{k^2}\overline{\overline{L}} + \frac{ik}{6\pi}H_o\overline{\overline{I}} \tag{4.64}$$

where $H_o = H(p=0)$. Thus

$$\overline{\overline{C}}_o = \left\{\overline{\overline{I}} - f_v\overline{\overline{T}}_o\left[\frac{\overline{\overline{L}}}{k^2} + \overline{\overline{I}}\frac{ik}{6\pi}H_o\right]\right\}^{-1} v\overline{\overline{T}}_o \tag{4.65}$$

Keeping only the leading order in the real and imaginary parts, we get

$$\overline{\overline{C}}_o = 3k^2 v\overline{\overline{D}}\,\overline{\overline{\eta}}\left\{1 + i\overline{\overline{D}}\,\overline{\overline{\eta}}\frac{k^3 v}{2\pi}S_o\right\} \tag{4.66}$$

where $S_o = 1 + n_o H_o$ is the static structure factor given in (4.11) and

$$\overline{\overline{D}} = \left[1 - 3f_v \overline{\overline{\eta}}\,\overline{\overline{L}}\right]^{-1} \tag{4.67}$$

From (4.38) and (4.40), the inverse average Green's function is

$$\overline{\overline{G}}^{-1}(\overline{p}) = (p^2 - k^2)\overline{\overline{I}} - \overline{p}\,\overline{p} - n_o \overline{\overline{C}}_o \tag{4.68}$$

From Appendix C, we see that the Green's function for the uniaxial medium has the following spectral representation:

$$\overline{\overline{G}}_{\text{ua}}^{-1}(\overline{p}) = p^2\overline{\overline{I}} - \overline{p}\,\overline{p} - k^2\overline{\overline{\varepsilon}} \tag{4.69}$$

where

$$\overline{\overline{\varepsilon}} = \varepsilon_a \hat{x}\hat{x} + \varepsilon_a \hat{y}\hat{y} + \varepsilon_c \hat{z}\hat{z} \tag{4.70}$$

is the relative permittivity tensor.

Comparison of (4.68) and (4.69) implies that the effective medium is uniaxial with relative permittivity tensor given by

$$\overline{\overline{\varepsilon}}^{(\text{eff})} = \overline{\overline{I}} + \frac{1}{k^2} n_o \overline{\overline{C}}_o \tag{4.71}$$

$$= \left\{\overline{\overline{I}} + 3f_v \overline{\overline{D}}\,\overline{\overline{\eta}}\right\} + i\left(\overline{\overline{D}}\,\overline{\overline{\eta}}\right)^2 \frac{3f_v k^3 v}{2\pi} S_o \tag{4.72}$$

Let $\overline{\overline{\varepsilon}}^{(\text{eff})} = \overline{\overline{\varepsilon}}^{(\text{eff})'} + i\overline{\overline{\varepsilon}}^{(\text{eff})''}$ where

$$\varepsilon_\mu^{(\text{eff})'} = 1 + \frac{f_v(\varepsilon_s - 1)}{1 + (1 - f_v)(\varepsilon_s - 1)L_\mu} \tag{4.73}$$

$$\varepsilon_\mu^{(\text{eff})''} = \frac{k^3 v}{6\pi} S_o \frac{f_v(\varepsilon_s - 1)^2}{[1 + (1 - f_v)(\varepsilon_s - 1)L_\mu]^2} \tag{4.74}$$

with $\mu = a, c$. Note that in the low-frequency limit, $\varepsilon_\mu^{(\text{eff})''} \ll \varepsilon_\mu^{(\text{eff})'}$ but generally nonzero. Thus even when the background and spheroid permittivity are purely real, the scattering loss gives rise to an imaginary part in the effective permittivity that is proportional to the structure factor S_o.

Since the effective medium is uniaxial, the characteristic waves correspond to the familiar ordinary and extraordinary waves of the uniaxial crystal, with dispersion relations given respectively by [Appendix C]

$$\frac{1}{\varepsilon_a} K^2 = k^2 \tag{4.75}$$

$$\frac{1}{\varepsilon_c}(K_x^2 + K_y^2) + \frac{1}{\varepsilon_a} K_z^2 = k^2 \tag{4.76}$$

where $\overline{K}$ is the effective wavevector.

4.4.2 QCA–CP

The modified transition operator satisfies the equation

$$\overline{\overline{\hat{t}}} = \overline{\overline{U}} + \overline{\overline{U}}\, E(\overline{\overline{G}})\, \overline{\overline{\hat{t}}} \tag{4.77}$$

with $E(\overline{\overline{G}})$ being the *average* Green's function, which is unknown. Based on the QCA result as well as physical intuition, it is reasonable to assume *a priori* that the average Green's function corresponds to that of an uniaxial medium with spectral representation given in the form of Eq. (4.69). Let

$$\overline{\overline{G}}^{-1}(\overline{p}) = p^2 \overline{\overline{I}} - \overline{p}\,\overline{p} - k^2 \overline{\overline{\varepsilon}}^{(\text{eff})} \tag{4.78}$$

where $\overline{\overline{\varepsilon}}^{(\text{eff})} = \varepsilon_a \hat{x}\hat{x} + \varepsilon_a \hat{y}\hat{y} + \varepsilon_c \hat{z}\hat{z}$ is still to be determined.

Much of the subsequent derivation parallels that of QCA. One notable difference is that we need the low-frequency expansion of the uniaxial Green's function in spatial domain. This is done in Appendix C. We have

$$\overline{\overline{G}}(\overline{r}, \overline{r}') = -\overline{\overline{K}}^{-2} \overline{\overline{N}} \delta(\overline{r} - \overline{r}') + \frac{i}{6\pi} \overline{\overline{K}}\, \overline{\overline{M}} \tag{4.79}$$

where

$$\overline{\overline{K}} = k^2\sqrt{\overline{\overline{\varepsilon}}^{(\text{eff})}} \tag{4.80}$$

Expressions for the tensors $\overline{\overline{N}}$ and $\overline{\overline{M}}$ are given in Appendix C. They depend on the ratio of the axial and transverse components of the effective permittivity:

$$\alpha = \frac{\varepsilon_c}{\varepsilon_a} \tag{4.81}$$

In comparison with the low-frequency expansion of the isotropic Green's function in Eq. (4.51), the uniaxial Green's function gives rise to depolarization factors that correspond to a less elongated spheroid (when $\alpha > 1$). Moreover, the radiative correction factor, i.e., the imaginary part in (4.79), is now anisotropic.

Analogous to (4.60), the modified transition operator in the low-frequency limit is

$$\overline{\overline{\hat{t}}}(\overline{p}, \overline{p}') = v\overline{\overline{\hat{t}}}_o \tag{4.82}$$

with

$$\overline{\overline{\hat{t}}}_o = \left[\left(\frac{1}{k_s^2 - k^2}\overline{\overline{I}} + \overline{\overline{K}}^{-2}\overline{\overline{N}}\right) - \frac{iv}{6\pi}\overline{\overline{K}}\,\overline{\overline{M}}\right]^{-1} \tag{4.83}$$

Keeping leading real and imaginary parts, we have

$$\overline{\overline{\hat{t}}}_o = 3\overline{\overline{K}}^2\,\overline{\overline{\hat{\eta}}}\left[\overline{\overline{I}} + \frac{iv}{2\pi}\overline{\overline{K}}^3\,\overline{\overline{\hat{\eta}}}\right] \tag{4.84}$$

where

$$\overline{\overline{\hat{\eta}}}_\mu = \frac{1}{3}(k_s^2 - k^2)\left[\overline{\overline{K}}^2 + (k_s^2 - k^2)\overline{\overline{N}}\right]^{-1} \tag{4.85}$$

Solving Eq. (4.47) gives

$$\overline{\overline{\hat{C}}}_o = \left\{\overline{\overline{I}} - f_v\overline{\overline{\hat{t}}}_o\left[\overline{\overline{K}}^{-2}\overline{\overline{N}} + \overline{\overline{K}}\,\overline{\overline{M}}\frac{i}{6\pi}H_o\right]\right\}^{-1} v\overline{\overline{\hat{t}}}_o \tag{4.86}$$

Keeping the leading real and imaginary parts, we get

$$\overline{\overline{\hat{C}}}_o = 3v\overline{\overline{K}}^2\,\overline{\overline{\hat{D}}}\,\overline{\overline{\hat{\eta}}}\left\{\overline{\overline{I}} + i\overline{\overline{\hat{D}}}\,\overline{\overline{\hat{\eta}}}\,\overline{\overline{M}}\,\overline{\overline{K}}^3\,\frac{v}{2\pi}S_o\right\} \tag{4.87}$$

where

$$\overline{\overline{\hat{D}}} = \left[\overline{\overline{I}} - 3f_v\,\overline{\overline{\hat{\eta}}}\,\overline{\overline{N}}\right]^{-1} \tag{4.88}$$

Then Eq. (4.46) implies a relative effective permittivity tensor of

$$\begin{aligned}\overline{\overline{\varepsilon}}^{(\text{eff})} &= \overline{\overline{I}} + \frac{1}{k^2}n_o\overline{\overline{\hat{C}}}_o \\ &= \left\{\overline{\overline{I}} + 3f_v\overline{\overline{\varepsilon}}^{(\text{eff})}\,\overline{\overline{\hat{D}}}\,\overline{\overline{\hat{\eta}}}\right\} + i\frac{3f_vk^3v}{2\pi}(\overline{\overline{\varepsilon}}^{(\text{eff})})^{\frac{5}{2}}\left(\overline{\overline{\hat{D}}}\,\overline{\overline{\hat{\eta}}}\right)^2\overline{\overline{M}}\,S_o\end{aligned} \tag{4.89}$$

Let $\overline{\overline{\varepsilon}}^{(\text{eff})} = \overline{\overline{\varepsilon}}^{(\text{eff})'} + i\overline{\overline{\varepsilon}}^{(\text{eff})''}$. Then

$$\varepsilon_\mu^{(\text{eff})'} = 1 + \frac{\varepsilon_\mu^{(\text{eff})}f_v(\varepsilon_s - 1)}{\varepsilon_\mu^{(\text{eff})} + (1-f_v)(\varepsilon_s - 1)N_\mu} \tag{4.90}$$

$$\varepsilon_\mu^{(\text{eff})''} = \frac{k^3v}{6\pi}S_oM_\mu(\varepsilon_\mu^{(\text{eff})})^{\frac{5}{2}}\frac{f_v(\varepsilon_s - 1)^2}{[\varepsilon_\mu^{(\text{eff})} + (1-f_v)(\varepsilon_s - 1)N_\mu]^2} \tag{4.91}$$

where $\mu = a, c$. Eqs. (4.90) and (4.91) provide a set of coupled nonlinear equations with which to solve for the unknowns $\varepsilon_a^{(\text{eff})}$ and $\varepsilon_c^{(\text{eff})}$. Since $\varepsilon_\mu^{(\text{eff})'} \gg \varepsilon_\mu^{(\text{eff})''}$, we can set $\varepsilon_\mu^{(\text{eff})} = \varepsilon_\mu^{(\text{eff})'}$ on the right-hand side of (4.90) and (4.91):

$$\varepsilon_\mu^{(\text{eff})'} = 1 + \frac{\varepsilon_\mu^{(\text{eff})'}f_v(\varepsilon_s - 1)}{\varepsilon_\mu^{(\text{eff})'} + (1-f_v)(\varepsilon_s - 1)N_\mu} \tag{4.92}$$

$$\varepsilon_\mu^{(\text{eff})''} = \frac{k^3v}{6\pi}S_oM_\mu(\varepsilon_\mu^{(\text{eff})'})^{\frac{5}{2}}\frac{f_v(\varepsilon_s - 1)^2}{[\varepsilon_\mu^{(\text{eff})'} + (1-f_v)(\varepsilon_s - 1)N_\mu]^2} \tag{4.93}$$

Then (4.92) is used to solve for $\varepsilon_\mu^{(\text{eff})'}$. Once this is found, its value is used in (4.93) to compute $\varepsilon_\mu^{(\text{eff})''}$.

4.5 Comparison with Mixing Formula

In composite material modeling and homogenization study, various expressions exist that allows one to calculate the effective permittivity of a medium consisting of many small dielectric particles [81]. The aligned spheroids provide a way to construct a macroscopically uniaxial medium from small isotropic particles [82]. One of the most widely used expressions in calculating the effective permittivity of a dielectric mixture is the Maxwell-Garnett formula, which is derived using electrostatics. As such, the effective permittivity only depends on the shape and permittivity of the small particles and the fractional volume, but not on frequency. However, we have already found that the effective permittivity has a frequency-dependent imaginary part which is due to scattering loss even when the constituent particles are not absorptive. Even without the scattering loss, the effective permittivity obtained using mixing formula and multiple scattering theories might still differ. In this section, we compare the multiple scattering results of QCA and QCA-CP with the Maxwell-Garnett mixing formula for spheroids. We shall not consider the scattering loss term (i.e., only $\overline{\overline{\varepsilon}}^{(\mathrm{eff})\prime}$ is used for comparison).

For aligned prolate spheroids, the Maxwell-Garnett mixing formula gives an effective permittivity of [83]

$$\varepsilon_\mu^{(\mathrm{eff})(\mathrm{MG})} = 1 + \frac{f_v(\varepsilon_s - 1)}{1 + (1 - f_v)(\varepsilon_s - 1)L_\mu} \tag{4.94}$$

where $\mu = a, c$. This is identical to Eq. (4.73) for the low-frequency QCA result. The QCA-CP result as shown in (4.92), however, differs from QCA and hence the Maxwell-Garnett formula.

Consider lossless spheroids with $\varepsilon_s = 3.2$. Fig. 4-2 shows the effective permittivity as a function of fractional volume for spheroids with $e = 2$. The relative effective permittivity increases from 1 (the background value) when $f_v = 0$ to 3.2 (the spheroid value) when $f_v = 1$. The QCA-CP curves are quite similar to QCA except that, as a result of the background renormalization, they have slightly larger values for both the axial (ε_a) and transverse (ε_c) components. Moreover, under the CP treatment, the depolarization tensor correspond to that of a slightly flattened spheroid. Thus the axial component is depressed relative to the transverse component for QCA-CP. Hence we see that the difference between QCA-CP and QCA is larger for the transverse component.

Fig. 4-3 shows the effective permittivity as a function of elongation for spheroids with $f_v = 0.2$. Again, the QCA and QCA-CP results are quite similar, with QCA-CP yielding larger values. As the spheroids become more elongated, the axial permittivity increases while the transverse permittivity decreases. One notable feature is that the gap between results from the two methods narrows as e increases for the axial component due to the flattening effect of QCA-CP. On the other hand, the gap for the transverse component stays constant.

The effective permittivity can be calculated from Monte Carlo simulations by comparing the simulated coherent field with the scattered field of a homogeneous medium of the same shape [84]. It is interesting to note that results from Monte Carlo simulations agree quite well with the Maxwell-Garnett mixing formula (or QCA) in the case of randomly oriented spheroids. In multiple scattering simulation of dielectric spheres, it has also been observed that the simulated effective permittivity agrees better with QCA than QCA-CP [42].

4.6 Comparison with Monte Carlo Simulations

The analytical theories of QCA and QCA-CP involve approximations whose validity can be difficult to assess. Numerical simulations such as those presented in the Chapter 3 provide extremely useful tools for checking such theories. In this section, we compare the extinction coefficients obtained using the analytical results of QCA and QCA-CP with Monte Carlo simulations. The extinction coefficient κ_e from Monte

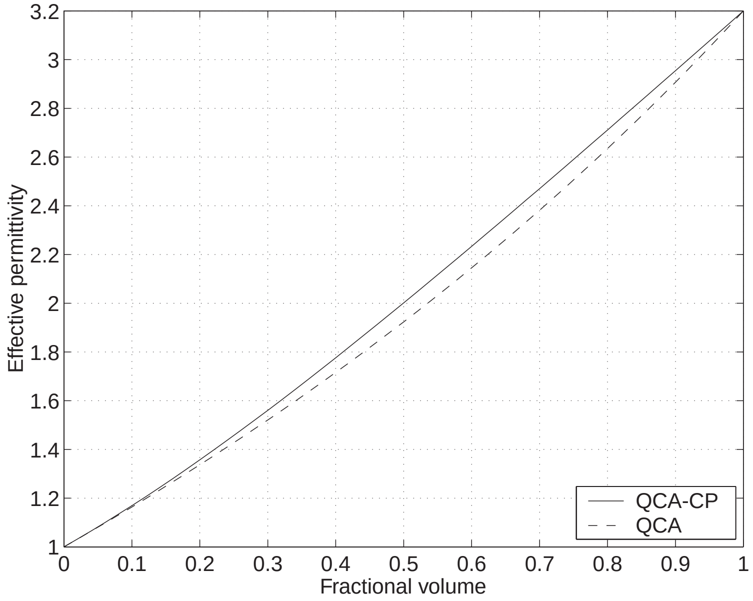

(a) Axial.

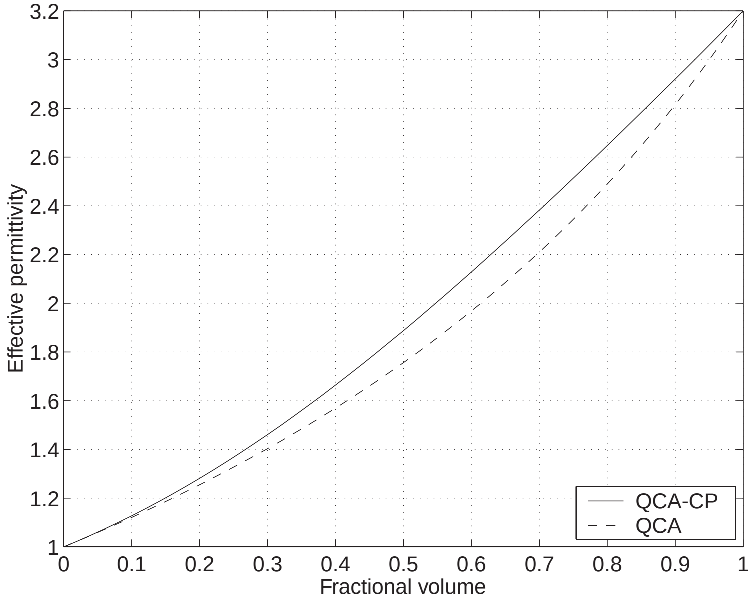

(b) Transverse.

Figure 4-2: Effective permittivity as a function of fractional volume f_v. Comparison between QCA and QCA-CP. $e = 2$ and $\varepsilon_s = 3.2$.

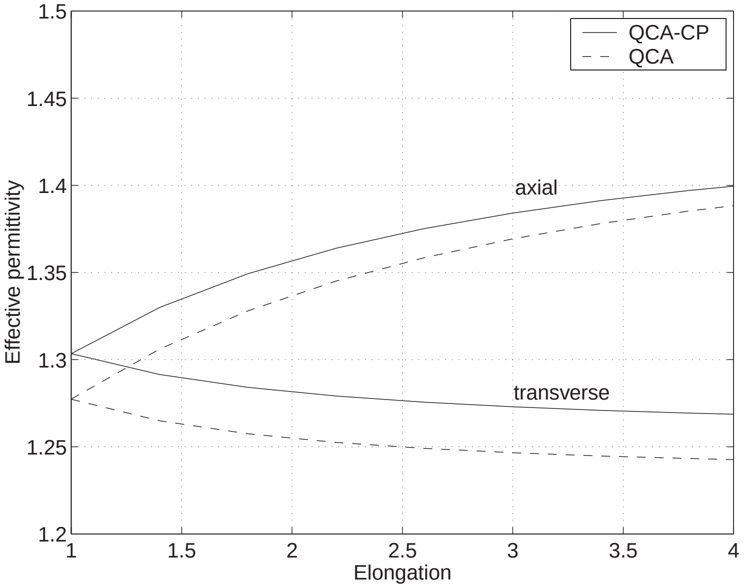

Figure 4-3: Effective permittivity as a function of elongation ratio $e = b/a$. Comparison between QCA and QCA-CP. $f_v = 0.2$ and $\varepsilon_s = 3.2$.

Carlo simulations is calculated using the methods described in Chapter 3 with dipole basis functions and point interactions. For lossless particles, $\kappa_e = \kappa_s$. For lossy particles, $\kappa_e = \kappa_s + \kappa_a$. The analytical extinction coefficient is computed as $\kappa_e = 2K''$, where $K = K' + iK''$ is the effective propagation constant. Suppose that the coherent wave propagates in a direction perpendicular to the $\hat{z}$-axis. Then vertical polarization corresponds to axial excitation and horizontal polarization corresponds to transverse excitation. In this case $K_v/k = \sqrt{\varepsilon_c^{(\text{eff})}}$ and $K_h/k = \sqrt{\varepsilon_a^{(\text{eff})}}$.

In Fig 4-4, we show the normalized extinction coefficient κ_e/k as a function of fractional volume obtained using Monte Carlo simulation, QCA, and QCA-CP. The particle size is such that $ka = 0.2$ with elongation $e = 2$. Results from independent scattering approximation are also shown for reference. It can be seen that for $f_v \lesssim 0.2$, the QCA-CP gives excellent agreement with Monte Carlo simulations. At higher fractional volume, both QCA and QCA-CP show a much stronger decrease with the fractional volume than the simulation results. It is possible that higher order particle correlation effects, which are neglected in QCA and QCA-CP, becomes more important at such high fractional volumes. Nevertheless, even though some dis-

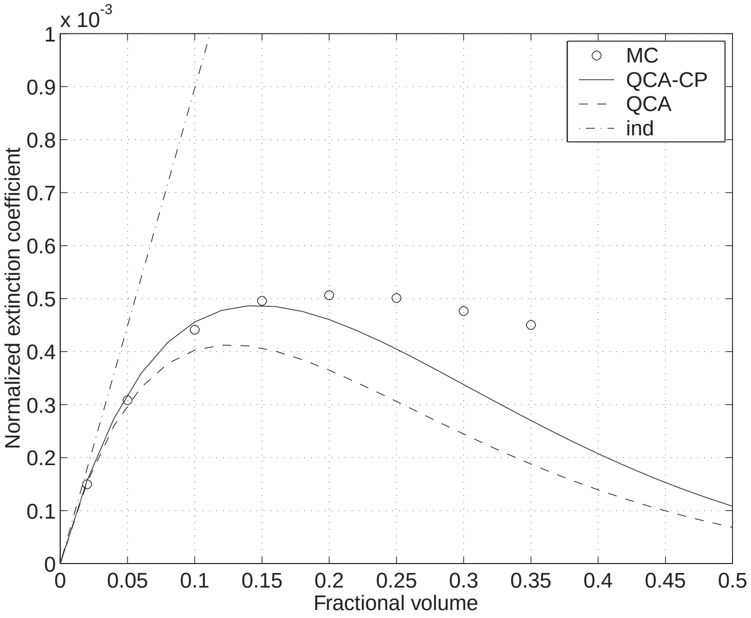

(a) Vertical polarization.

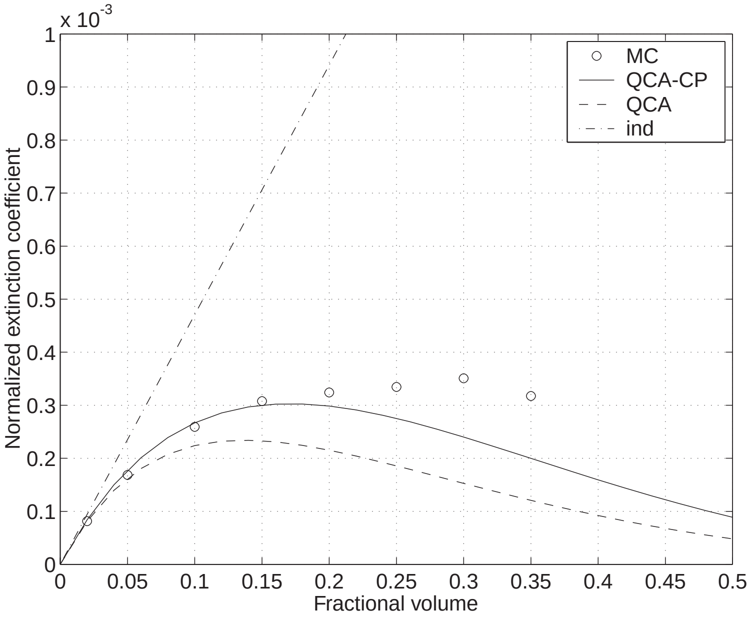

(b) Horizontal polarization.

Figure 4-4: Normalized extinction coefficient κ_e/k as a function of fractional volume f_v. Comparison between different methods. $ka = 0.2$, $e = 2$, and $\varepsilon_s = 3.2$.

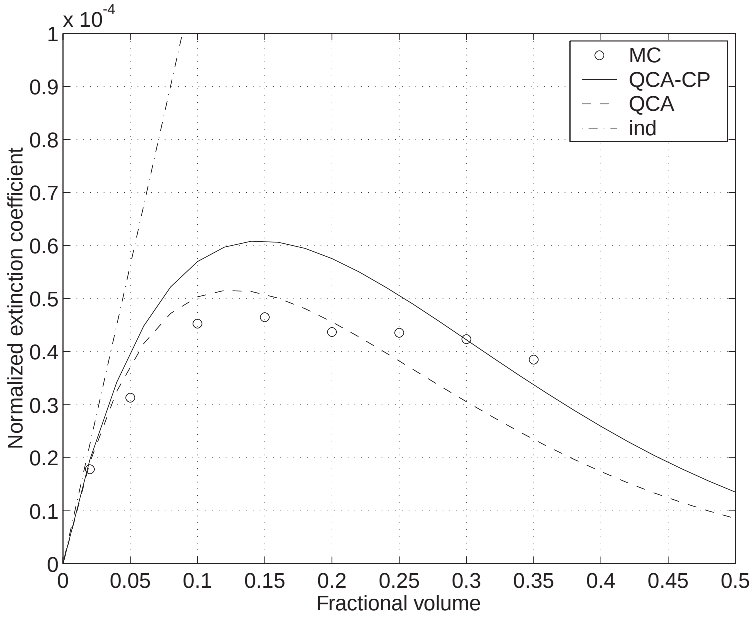

(a) Vertical polarization.

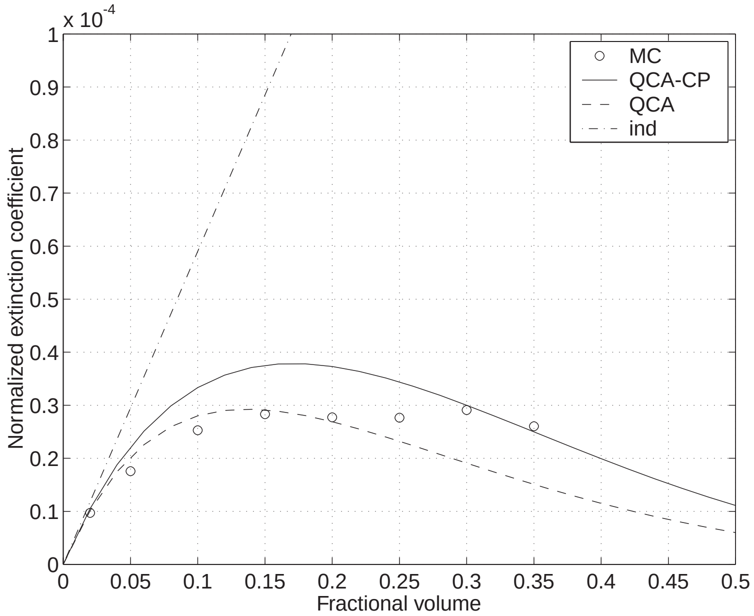

(b) Horizontal polarization.

Figure 4-5: Normalized extinction coefficient κ_e/k as a function of fractional volume f_v. Comparison between different methods. $ka = 0.1$, $e = 2$, and $\varepsilon_s = 3.2$.

crepancy exists, QCA and QCA-CP still outperform independent scattering, which grossly overestimates the scattering coefficient. In Fig. 4-5, the results for smaller particles with $ka = 0.1$ are presented. In this case, QCA seems to give better agreement with Monte Carlo simulations at lower fractional volumes while QCA-CP is better at higher fractional volumes.

Fig. 4-6 shows the normalized extinction coefficient as a function of fractional volume for lossy spheroids with size parameter $ka = 0.2$. For lossy particles, the extinction coefficient increases monotonously with f_v. Again, QCA-CP gives very good results compared with Monte Carlo simulations. Next we examine the dependence of the extinction coefficient on the elongation ratio for $ka = 0.2$. Fig. 4-7 shows that overall, QCA-CP agrees quite well with Monte Carlo simulations, especially at smaller elongations. The Monte Carlo simulation results show a slightly steeper increase with elongation.

4.7 Conclusions

In this chapter, we study multiple scattering of dielectric spheroids using approximations that are based on analytic wave theory. The spheroids have aligned orientation but are uniformly distributed in space, subject only to the condition of no overlaps. The Percus-Yevick pair distribution is available in closed form for such a system. The Foldy-Lax multiple scattering equations are obtained and the procedure of conditional averaging is applied. To obtain simple analytical expressions, the hierarchy of averaged equations is truncated at second order by making use of the quasi-crystalline approximation (QCA) and the quasi-crystalline approximation with coherent potential (QCA-CP).

The QCA and QCA-CP equations can be solved in the low-frequency limit. We present expressions for the transition operator and the mass operator in such a limit. The average Green's function, which is uniaxial, follows directly. For QCA-CP, a low-

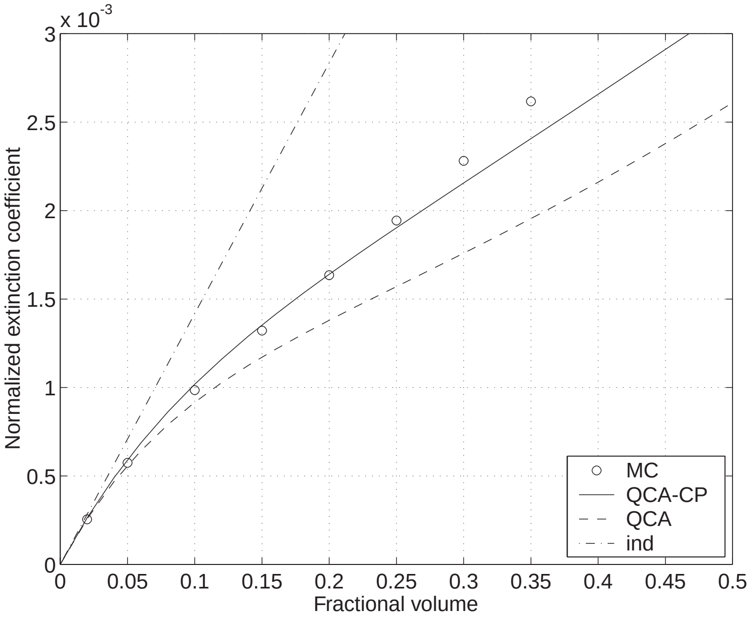

(a) Vertical polarization.

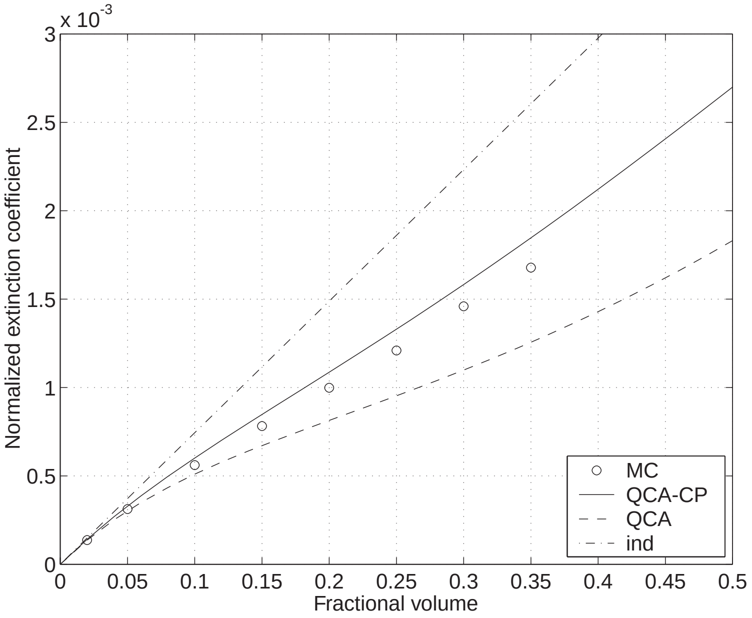

(b) Horizontal polarization.

Figure 4-6: Normalized extinction coefficient κ_e/k as a function of fractional volume f_v for lossy particles. Comparison between different methods. $ka = 0.2$, $e = 2$, and $\varepsilon_s = 3.2 + i0.01$.

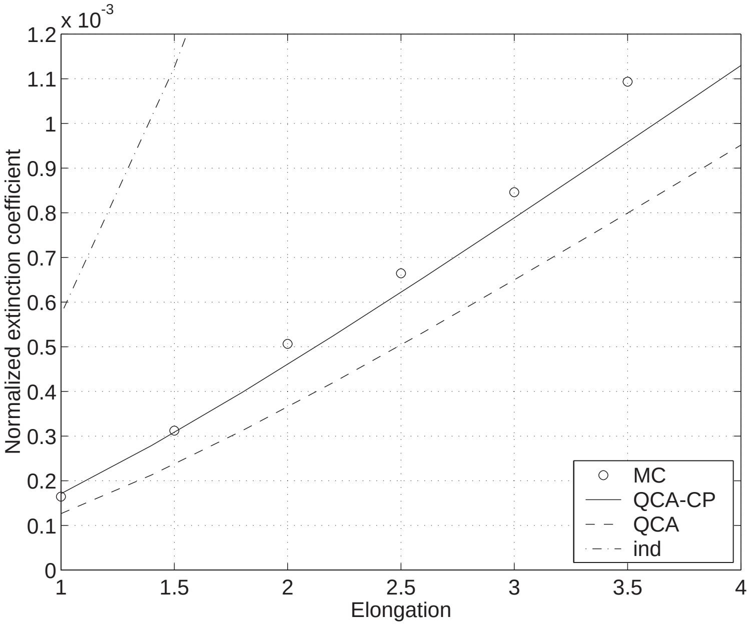

(a) Vertical polarization.

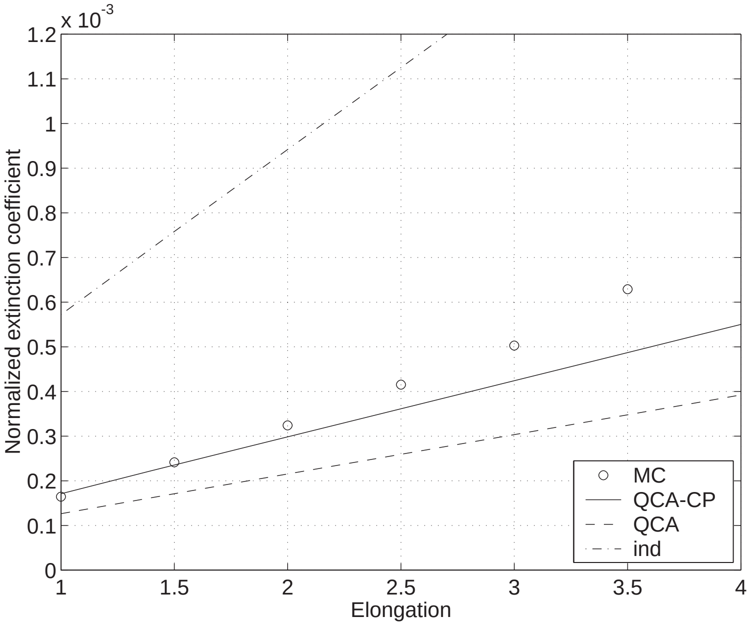

(b) Horizontal polarization.

Figure 4-7: Normalized extinction coefficient κ_e/k as a function of elongation ratio $e = b/a$. Comparison between different methods. $ka = 0.2$, $e = 2$, and $\varepsilon_s = 3.2$.

frequency expansion of the uniaxial dyadic Green's function is required. Interesting differences from the low-frequency expansion of the isotropic Green's function include: (*i*) the depolarization factors are present with a modified eccentricity and (*ii*) The radiative loss term becomes anisotropic.

Using the low-frequency solutions of QCA and QCA-CP, we compare the effective permittivity with the Maxwell-Garnett mixing formula. We find that by neglecting the radiative loss term, QCA gives an identical expression to the mixing formula. However, QCA-CP gives a slightly larger value due to the renormalization of the background medium. The difference between QCA and QCA-CP is larger in the transverse component than the axial component due to the flattening effect of the uniaxial Green's function in the case of QCA-CP.

We also compare the extinction coefficients obtained using QCA and QCA-CP with those of Monte Carlo simulations computed using the methods discussed in Chapter 3. It is found that both methods perform quite well, especially for smaller fractional volumes. At larger fractional volumes, higher order statistics of particle positions, which are not taken into account in QCA and QCA-CP, might become more important.

Chapter 5

Dense Medium Model of Polarimetric Thermal Emission from Sea Foam

5.1 Introduction

It has long been known that the presence of sea foam greatly enhances the microwave emissivity from the ocean surface [85, 86, 87, 88]. However, little theoretical progress has been made on the accurate modeling and understanding of sea foam emission since the 1970s. Important early contributions include the work by Droppleman [89], who modeled the foam as a homogeneous effective medium with mixture of air and water and found that the emissivity approached one for high air fraction. Rosenkranz and Staelin [90] constructed a more elaborate model where the foam layer is approximated by thin parallel layers of water separated by air. Even though these models could explain the high emissivity from sea foam, they were rather idealized and did not relate to the underlying physical parameters of the foam. On the other hand, recent studies of thermal emission from the ocean surface have focused on incorporating rough surface effects [91, 92]. To take into account of emission from foam, one usually

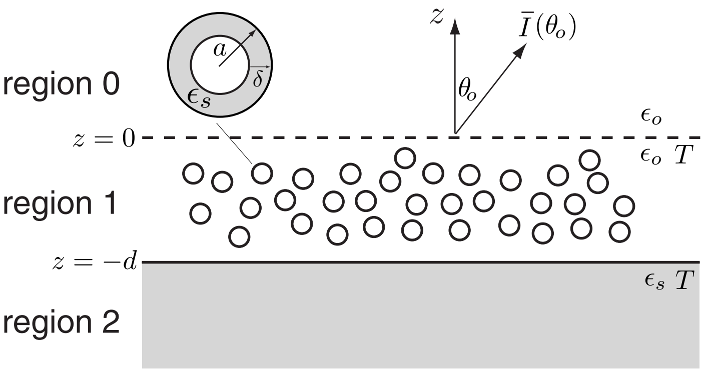

Figure 5-1: Thermal emission from a layer of air bubbles with thin water shells overlying the flat ocean surface.

has to resort to an empirical formula [93].

In this chapter, we model the foam as a layer of randomly distributed air bubbles overlying a flat ocean surface (Fig. 5-1). The bubbles are assumed to be spherical and covered with an outer layer of sea water. The permittivity of the lower half-space and the water shell is taken to be ϵ_s, while the permittivity inside and outside the shell is ϵ_o. The shell thickness (δ) of the bubble is small compared to its outer radius (a) so that a high void fraction is implicit in this model. Let f_v be the fractional volume of the bubbles. The fractional volume occupied by the water shells is then $f_w \approx f_v(3\delta/a) \ll 1$. It should be noted that such a foam model has been considered previously [94], but Rayleigh scattering and the independent scattering approximation were used. Thus its validity is limited to small bubbles that are sparsely distributed. Since sea foam bubbles are likely to come in a variety of sizes as well as densities depending on wind speeds and the stages of development, we prefer to consider the general situation where the bubbles can be closely packed with sizes comparable to the wavelength. To this end, we employ the quasi-crystalline approximation (QCA) to incorporate coherent multiple scattering effects among the bubbles. The brightness temperature is obtained by numerically solving the dense medium radiative transfer (DMRT) equation. The QCA-based DMRT approach was first developed by Tsang *et al.* [14, 95] and applied to the remote sensing of snow.

In Sec. 5.2, we summarize the T-matrix formulation of QCA. The method is applied to densely packed, coated spheres of moderate size. We examine the dispersion relation for bubble scatterers and compare with low-frequency QCA approximations. In Sec. 5.3, the absorption coefficient and scattering coefficient are obtained from the QCA solution. These parameters are used as inputs for radiative transfer calculations and applied to the passive remote sensing of sea foam.

The flat ocean surface considered in most of this chapter is a convenient assumption. However, one might question how well this approximation works in practice since the actual wind-driven ocean surface can be far from flat. In Sec. 5.4, we take into account of the large-scale roughness in the ocean surface by using a geometric tilting model where emission from a tilted foam layer is related to emission from a flat foam layer through simple angle and polarization transformations. The Cox-Munk slope distribution is used to obtain the average brightness temperatures from foam-covered rough ocean surface.

Since our focus is on sea foam emission, atmospheric effects, though important in passive remote sensing of the ocean, are neglected in the present study.

5.2 T-matrix Formulation of the Quasi-Crystalline Approximation (QCA)

In Chapter 4, we discuss the quasi-crystalline approximation for multiple scattering in the operator formalism. Low-frequency solutions for dielectric spheroids in aligned orientation are derived. However, in many applications, the particle size is not small compared with the wavelength so that low-frequency formulae will not be applicable. To deploy QCA for moderate size particles, it is most convenient to formulate the multiple scattering problem in a slightly different way by using the Foldy-Lax multiple scattering equations with the T-matrix coefficients [9]. For spherical scatterers, the

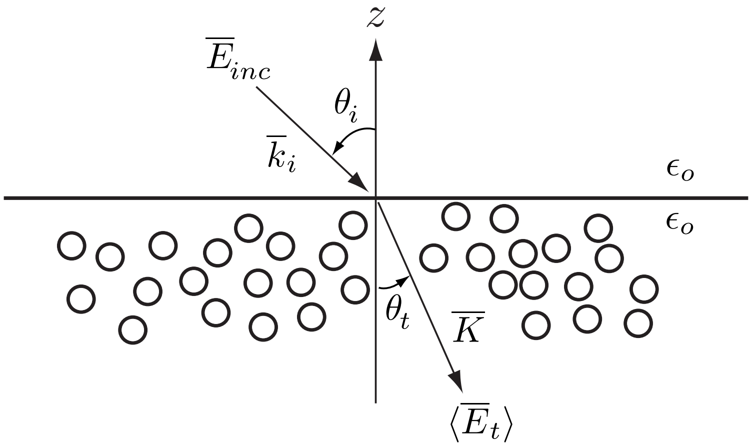

Figure 5-2: An incident wave impinges on a half-space of densely distributed spherical scatterers.

T-matrix coefficients give the Mie scattering solution, in which case this formulation is known as QCA-Mie theory. The QCA-Mie theory has been applied to dielectric spheres [41, 96] and coated spheres [80]. The latter is appropriate for the bubbles. We summarize the results below. Derivation as well as detailed expressions can be found in the literature [14, 95].

5.2.1 Generalized Lorentz-Lorenz Law and Ewald-Oseen Theorem

Consider a plane wave incident on a half-space of spherical scatterers (Fig. 5-2). The spherical scatterers can be inhomogeneous, e.g., with multilayered structure. Let

$$\overline{E}_{inc}(\overline{r}) = \hat{e}_i \, e^{i\overline{k}_i\cdot\overline{r}} \tag{5.1}$$

where

$$\overline{k}_i = k(\sin\theta_i\cos\phi_i\hat{x} + \sin\theta_i\sin\phi_i\hat{y} - \cos\theta_i\hat{z}) \tag{5.2}$$

A coherent transmitted field $\langle \overline{E}_t \rangle$ propagates downward with effective wavevector

$$\overline{K} = K(\sin\theta_t \cos\phi_t \hat{x} + \sin\theta_t \sin\phi_t \hat{y} - \cos\theta_t \hat{z}) \tag{5.3}$$

where $\phi_t = \phi_i$ and $K \sin\theta_t = k \sin\theta_i$. The effective wavenumber K is to be determined.

As a result of multiple scattering, the final exciting field on each scatterer is different from the incident field. The Foldy-Lax multiple scattering equations relate the exciting fields from all the scatterers. In the T-matrix formulation, the exciting fields are expanded in terms of vector spherical wavefunctions. Applying QCA to the Foldy-Lax equations gives rise to two sets of equations for the unknown exciting field coefficients $Y_n^{(M)}$ and $Y_n^{(N)}$, where n is the spherical wave multipole index ($n = 1$ denotes dipoles, $n = 2$ denotes quadrupoles, etc.) and $(M), (N)$ specify the two polarization states of the vector spherical waves. The two sets of equations are generalized versions of the Lorentz-Lorenz law and Ewald-Oseen theorem derived for point dipoles [97].

The generalized Lorentz-Lorenz law is

$$\begin{aligned} Y_n^{(M)} = 4\pi n_o \sum_{\nu=1}^{\infty} \sum_{p=1}^{\infty} S_p(K) \Big\{ & -T_\nu^{(M)} Y_\nu^{(M)} A_c(\nu, n, p) \\ & + T_\nu^{(N)} Y_\nu^{(N)} A_x(\nu, n, p) \Big\} \end{aligned} \tag{5.4}$$

$$\begin{aligned} Y_n^{(N)} = 4\pi n_o \sum_{\nu=1}^{\infty} \sum_{p=1}^{\infty} S_p(K) \Big\{ & T_\nu^{(M)} Y_\nu^{(M)} A_x(\nu, n, p) \\ & - T_\nu^{(N)} Y_\nu^{(N)} A_c(\nu, n, p) \Big\} \end{aligned} \tag{5.5}$$

where n_o is the number density of the scatterers and

$$A_c(\nu, n, p) = \frac{(2\nu + 1)}{\nu(\nu + 1)} \frac{n(n + 1)}{(2n + 1)} i^{\nu - n - p} a(1, \nu | -1, n | p) a(\nu, n, p) \tag{5.6}$$

$$A_x(\nu, n, p) = \frac{(2\nu + 1)}{\nu(\nu + 1)} \frac{n(n + 1)}{(2n + 1)} i^{\nu - n - p} a(1, \nu | -1, n | p, p - 1) b(\nu, n, p) \tag{5.7}$$

Expressions for the coefficients $a(\ )$ and $b(\ )$ as well as $S_p(K)$ are given in [14].

The generalized Lorentz-Lorenz law gives a homogeneous system of equations for $Y_n^{(M)}$ and $Y_n^{(N)}$. Non-trivial solutions only exist when the determinant of the matrix is zero. This imposes a condition on K that determines the dispersion relation and characteristic waves in the effective medium. Two main ingredients are needed in Eqs. (5.4) and (5.5). The first is the T-matrix coefficients $T_\nu^{(M)}$ and $T_\nu^{(N)}$ that characterize scattering by a single spherical scatterer. The second is the function $S_p(K)$, which depends on the pair distribution function $g(r)$ and hence the correlation of scatterer positions. However, the generalized Lorentz-Lorenz law is independent of the incident angles or polarization.

The excitation amplitude for the characteristic waves can be obtained using the generalized Ewald-Oseen theorem, which is given as:

$$\begin{aligned}-\frac{(K_z - k_{iz})k_{iz}k}{2\pi} &= -in_o \sum_{\nu=1}^{\infty} T_\nu^{(M)} Y_\nu^{(M)} B_\nu^{(M)}(\theta_i, \theta_t) \\ &\quad + in_o \sum_{\nu=1}^{\infty} T_\nu^{(N)} Y_\nu^{(N)} B_\nu^{(N)}(\theta_i, \theta_t) \qquad (5.8)\end{aligned}$$

where

$$B_\nu^{(M)}(\theta_i, \theta_t) = \frac{2\nu+1}{\nu(\nu+1)} \frac{P_\nu^1(\cos(\theta_i - \theta_t))}{|\sin(\theta_i - \theta_t)|} \qquad (5.9)$$

$$\begin{aligned}B_\nu^{(N)}(\theta_i, \theta_t) &= \frac{2\nu+1}{\nu(\nu+1)} \left\{ \frac{\cos(\theta_i - \theta_t)}{|\sin(\theta_i - \theta_t)|} P_\nu^1(\cos(\theta_i - \theta_t)) \right. \\ &\quad \left. + \nu(\nu+1) P_\nu(\cos(\theta_i - \theta_t)) \right\} \qquad (5.10)\end{aligned}$$

with P_ν and P_ν^1 being the Legendre functions.

5.2.2 Dispersion Relation for Bubbles

The dispersion relation for the dense medium of spherical scatterers is determined by the generalized Lorentz-Lorenz law. In this section, we solve Eqs. (5.4) and (5.5) for the bubble scatterers that are used to model the foam. We assume that the scatterers are non-interpenetrable but otherwise non-interacting so that the Percus-Yevick pair-distribution function for hard spheres can be used [9]. The multipoles are truncated at $N_{\max} = 4$.

The bubble scatterer is a special case of a two-layered dielectric sphere. The T-matrix elements for a two-layered dielectric sphere are well-known [4]. Let a be the outer radius, k_a be the wavenumber of the outer layer, b be the inner radius, and k_b be the wavenumber of the inner layer. Then

$$T_n^{(M)} = \frac{[\rho j_n(\rho)]'[j_n(\zeta) + B_n y_n(\zeta)] - \{[\zeta j_n(\zeta)]' + B_n[\zeta y_n(\zeta)]'\} j_n(\rho)}{[\rho h_n(\rho)]'[j_n(\zeta) + B_n y_n(\zeta)] - \{[\zeta j_n(\zeta)]' + B_n[\zeta y_n(\zeta)]'\} h_n(\rho)} \tag{5.11}$$

$$T_n^{(N)} = -\frac{[\rho j_n(\rho)]'\zeta^2[j_n(\zeta) + A_n y_n(\zeta)] - \{[\zeta j_n(\zeta)]' + A_n[\zeta y_n(\zeta)]'\}\rho^2 j_n(\rho)}{[\rho h_n(\rho)]'\zeta^2[j_n(\zeta) + A_n y_n(\zeta)] - \{[\zeta j_n(\zeta)]' + A_n[\zeta y_n(\zeta)]'\}\rho^2 h_n(\rho)} \tag{5.12}$$

where

$$\rho = ka, \qquad \zeta = k_a a, \qquad \xi = k_a b, \qquad \eta = k_b b \tag{5.13}$$

The functions j_n and y_n are the spherical Bessel and Neumann functions, respectively. The notation $[xF(x)]'$ denotes differentiation of $xF(x)$ with respect to x, and

$$A_n = -\frac{[\xi j_n(\xi)]'\eta^2 j_n(\eta) - [\eta j_n(\eta)]'\xi^2 j_n(\xi)}{[\xi y_n(\xi)]'\eta^2 j_n(\eta) - [\eta j_n(\eta)]'\xi^2 y_n(\xi)} \tag{5.14}$$

$$B_n = -\frac{[\xi j_n(\xi)]' j_n(\eta) - [\eta j_n(\eta)]' j_n(\xi)}{[\xi y_n(\xi)]' j_n(\eta) - [\eta j_n(\eta)]' y_n(\xi)} \tag{5.15}$$

For the special case of coated bubbles (Fig. 5-1), $b = a - \delta$, $k_a = k_s$ and $k_b = k$. Equipped with the general QCA-Mie solution which is applicable for large particles, it is interesting to compare it with the low-frequency QCA result. The low-frequency approximation gives the following relation for the effective wavenumber K [80]

$$K^2 = k^2 + \frac{3k^2 f_v \eta}{1 - f_v \eta}\left\{1 + i\frac{2k^3 a^3 y}{3(1 - f_v \eta)} S_o\right\} \tag{5.16}$$

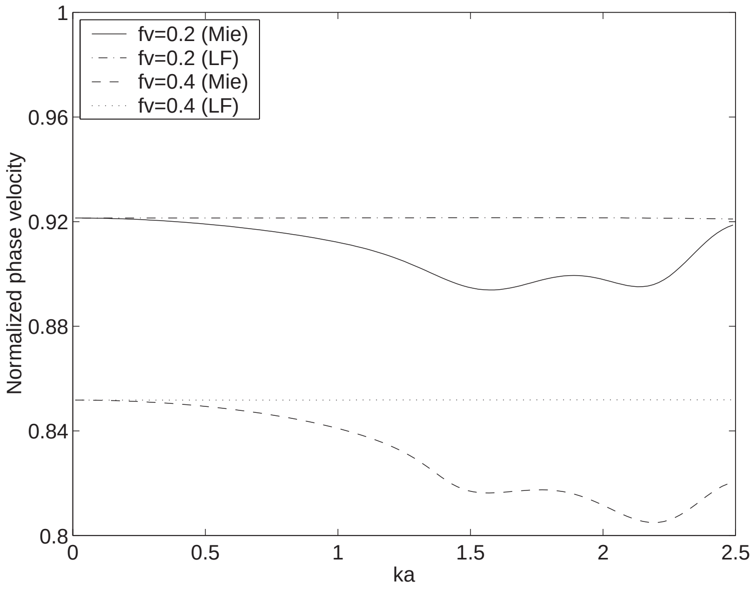

(a) Normalized phase velocity k/K_r.

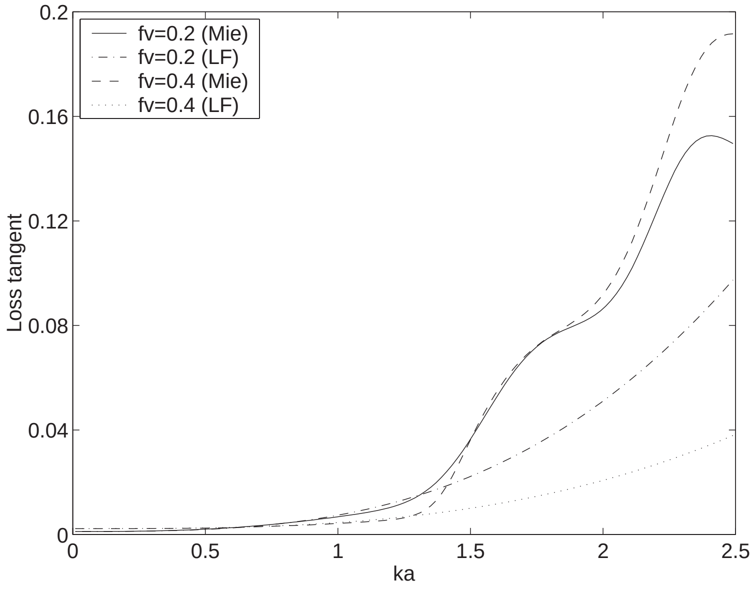

(b) Loss tangent $2K_i/K_r$.

Figure 5-3: Dispersion characteristics for bubbles with $\varepsilon_s = 20 + i0.2$ and $\delta/a = 0.03$.

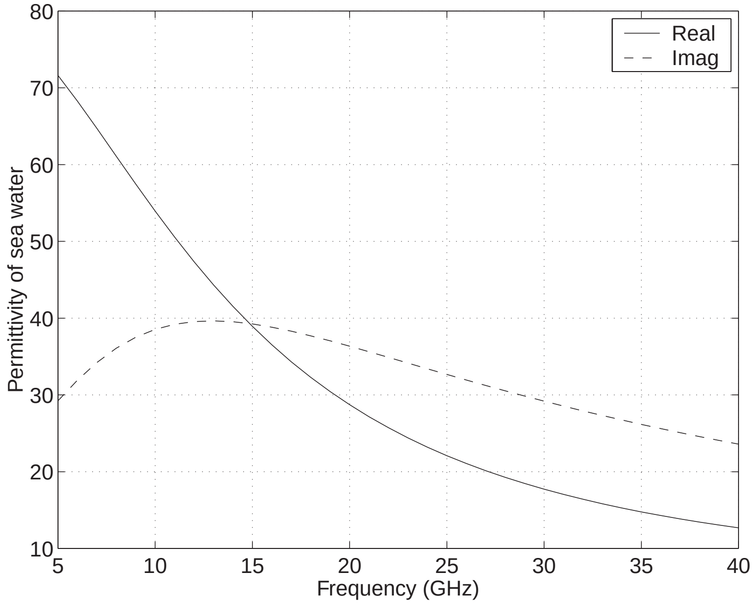

Figure 5-4: Relative permittivity of sea water at temperature 285 K and salinity content equal to 10 parts per thousand.

where

$$\eta = \frac{(\varepsilon_s - 1)(2\varepsilon_s + 1)(1 - q^3)}{(\varepsilon_s + 2)(2\varepsilon_s + 1) - 2q^3(\varepsilon_s - 1)^2} \tag{5.17}$$

with $q = 1 - (\delta/a)$.

Let K_r and K_i be the real and imaginary parts of K, respectively. The dispersion characteristics will be presented in terms of the normalized phase velocity $v_p = k/K_r$ and loss tangent $L = 2K_i/K_r$ [96]. Fig. 5-3 shows the dispersion characteristics for scatterers with small loss ($\varepsilon_s = 20 + i0.2$). The thickness of the shell is $\delta = 0.03a$. The low frequency results agree with the QCA-Mie solution for $ka \lesssim 0.5$ and indeed provides reasonably good approximations up to $ka \approx 1$. However, as ka increases, the QCA-Mie solution displays oscillations due to resonant scattering, which is not captured in the low-frequency approximation. Comparing the results for $f_v = 0.2$ and $f_v = 0.4$, we observe that the increased multiple scattering at the higher fractional volume causes v_p to be smaller for $f_v = 0.4$.

The small-loss case does not correspond to sea foam bubble at microwave frequencies. Fig. 5-4 shows the relative permittivity of sea water [98]. Both the real and imaginary parts of the sea water permittivity are quite large. Fig. 5-5 shows the dispersion characteristics for scatterers with high loss, which is more representative of sea foam at microwave frequencies. In this case, the scattering resonance features disappear as a result of the strong absorption by the scatterers. It is also notable that v_p increases with ka, especially when $ka > 1$. This is a direct consequence of the large imaginary part in the scatterer permittivity.

5.3 Thermal Emission from Sea Foam

In this section, the brightness temperatures from a layer of sea foam overlying the ocean surface are computed (Fig. 5-1) using the radiative transfer (RT) equation. We first describe how to calculate the RT input parameters from the QCA-Mie solution. The extinction behavior of the sea foam is studied. The RT equation is then solved with these inputs and the appropriate boundary conditions at the upper and lower interfaces of the foam layer. It is important to note that the RT equation used here differs from the conventional RT equation in that the RT input parameters incorporates coherent multiple scattering effects. In contrast, the conventional RT equation assumes independent scattering and is not valid when the scatterers are densely packed. To distinguish it from the conventional approach, the RT theory used here is often referred to as the dense medium radiative transfer (DMRT) theory.

5.3.1 Extinction Behavior

Radiative transfer equations use the scattering coefficient, absorption coefficient, and scattering phase matrix, to characterize the transport of specific intensity in a random medium. These quantities can be calculated directly from the QCA solution.

After K and $Y_n^{(M,N)}$ are solved using the generalized Lorentz-Lorenz law and

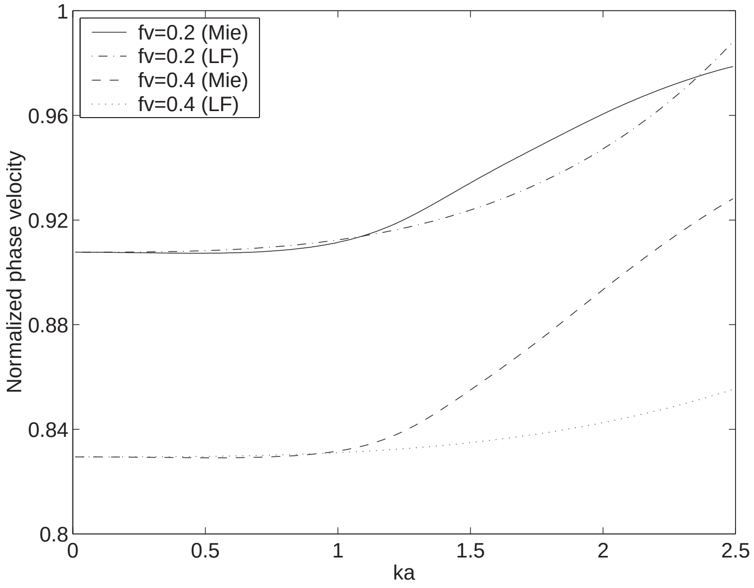

(a) Normalized phase velocity k/K_r.

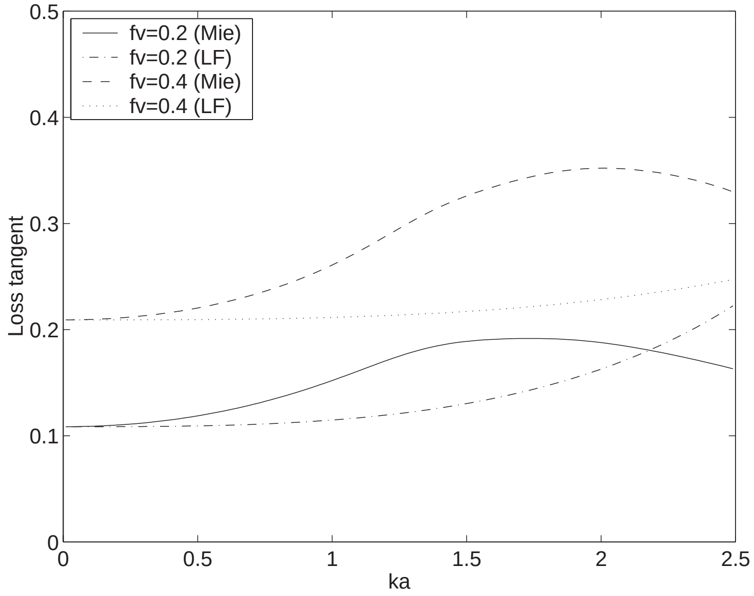

(b) Loss tangent $2K_i/K_r$.

Figure 5-5: Dispersion characteristics for bubbles with $\varepsilon_s = 20 + i20$ and $\delta/a = 0.03$.

Ewald-Oseen theorem [Eqs. (5.4)–(5.8)], the absorption coefficient κ_a is computed as

$$\kappa_a = \frac{2\pi}{k^2|1-R_v|^2} \sum_{n=1}^{N_{\max}} (2n+1) \left\{ |Y_n^{(M)}|^2 \left[-\mathrm{Re}T_n^{(M)} - |T_n^{(M)}|^2 \right] \right. \\ \left. + |Y_n^{(N)}|^2 \left[-\mathrm{Re}T_n^{(N)} - |T_n^{(N)}|^2 \right] \right\} \tag{5.18}$$

where $N_{\max}$ is the maximum order of multipoles used and R_v is the TM Fresnel reflection coefficient for the effective layer at normal incidence.

The scattering phase matrix $P_{\alpha\beta}$, which is defined as the bistatic scattering cross section per unit volume, can be obtained from the average excitation coefficients with the distorted Born approximation. Explicit expressions for the phase matrix can be found elsewhere [14, 95]. Since the scattering medium is azimuthally symmetric, we integrate over the azimuthal angle to obtain the phase functions

$$p_{\alpha\beta}(\theta, \theta') = \int_0^{2\pi} d\phi P_{\alpha\beta}(\theta, \phi; \theta', \phi' = 0) \tag{5.19}$$

where $\alpha, \beta = v, h$.

The scattering coefficient can be obtained by integrating the phase function over all scattered angles:

$$\kappa_s = \int_0^{\pi} d\theta \sin\theta \left[p_{\alpha\alpha}(\theta, \theta') + p_{\beta\alpha}(\theta, \theta') \right] \tag{5.20}$$

where $\alpha = v, \beta = h$ or vice versa. Like the absorption coefficient κ_a, the scattering coefficient is independent of polarization and incident angle θ'. Thus the extinction coefficient $\kappa_e = \kappa_s + \kappa_a$ is also independent of incident angle and polarization.

We now examine the extinction behavior of sea foam as a function of frequency. The permittivity for the sea water shell is shown in Fig. 5-4. In Fig. 5-6, the foam bubble size is taken to be $a = 1$ mm with fractional thickness $\delta/a = 0.03$. The fractional volume is 0.2. In Fig. 5-6(a), the normalized extinction coefficient is shown.

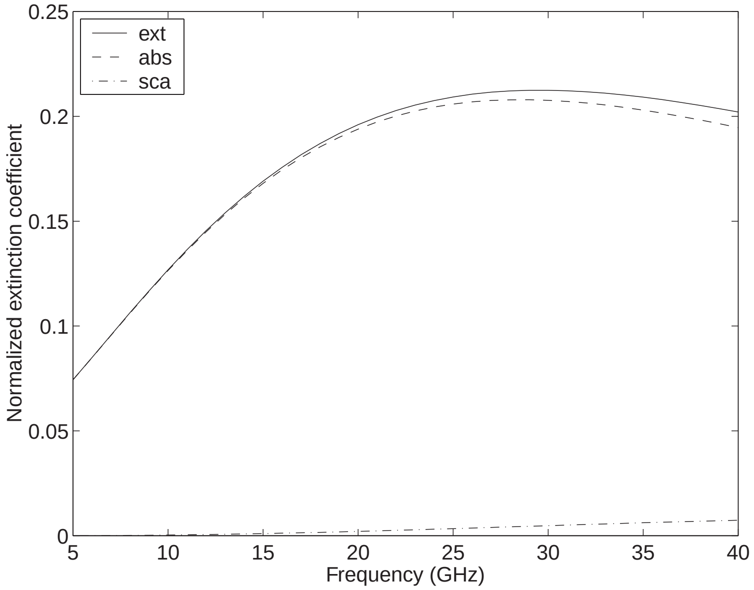

(a) Normalized extinction coefficient κ_e/k.

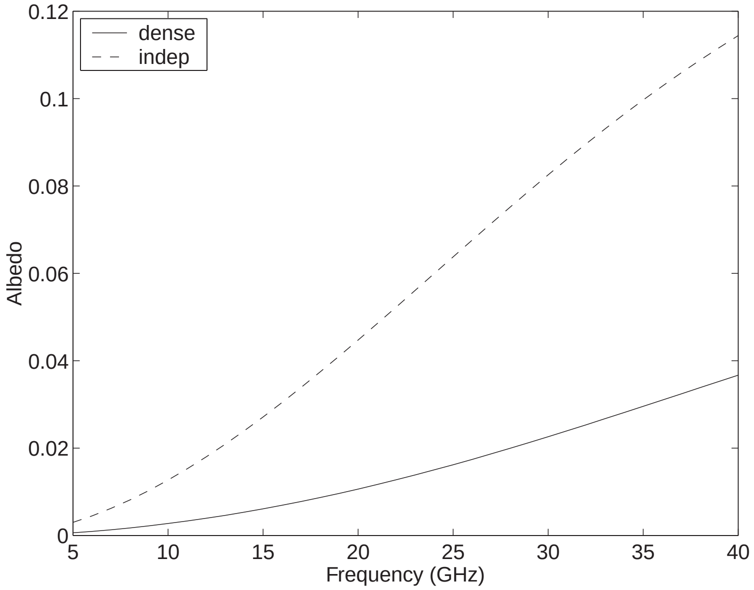

(b) Albedo $\tilde{\omega} = \kappa_s/\kappa_e$.

Figure 5-6: Extinction behavior of sea foam for $a = 1$ mm, $\delta/a = 0.03$, and fractional volume of 0.2.

It can be seen that the scattering coefficient is quite small, and absorption contributes to nearly all the extinction in the foam. This fact is quantified in Fig. 5-6(b), where the albedo $\tilde{\omega} = \kappa_s/\kappa_e$ is displayed and shown to be less than 4%. We also show the albedo calculated using independent scattering. Since independent scattering overestimates the scattering coefficient and underestimates the absorption coefficient, it predicts a much larger albedo.

Fig. 5-7 shows the extinction behavior for a larger bubble with $a = 2$ mm. Other parameters are same as in Fig. 5-6. In this case, even though the absorption still dominates, scattering effects are not negligible. The albedo has increased from under 4% in the case of $a = 1$ mm to about 15% at 37 GHz.

Besides the extinction coefficient, which is related to the imaginary part of the effective wavenumber K, the RT equation also requires the real part of K, which comes in through the boundary conditions (see Sec. 5.3.2). Thus for later reference, we show in Fig. 5-8 the solution for K_r/k as a function of frequency for bubble radius of $a = 1$ mm and $a = 2$ mm. Other parameters are the same as in Figs. 5-6 and 5-7. Note that K_r/k decreases with f, which is consistent with the fact that v_p increases with ka for lossy particles, as discussed earlier (cf. Fig. 5-5).

5.3.2 Solutions of Dense Medium Radiative Transfer Equation

The QCA-based quantities of (5.18)–(5.20) are used as inputs to the DMRT equation:

$$\cos\theta \frac{dI_v(z,\theta)}{dz} = -\kappa_e I_v(z,\theta) + \kappa_a CT + \int_0^\pi d\theta' \sin\theta' [p_{vv}(\theta,\theta') I_v(z,\theta') + p_{vh}(\theta,\theta') I_h(z,\theta')] \tag{5.21}$$

$$\cos\theta \frac{dI_h(z,\theta)}{dz} = -\kappa_e I_h(z,\theta) + \kappa_a CT + \int_0^\pi d\theta' \sin\theta' [p_{hh}(\theta,\theta') I_h(z,\theta') + p_{hv}(\theta,\theta') I_v(z,\theta')] \tag{5.22}$$

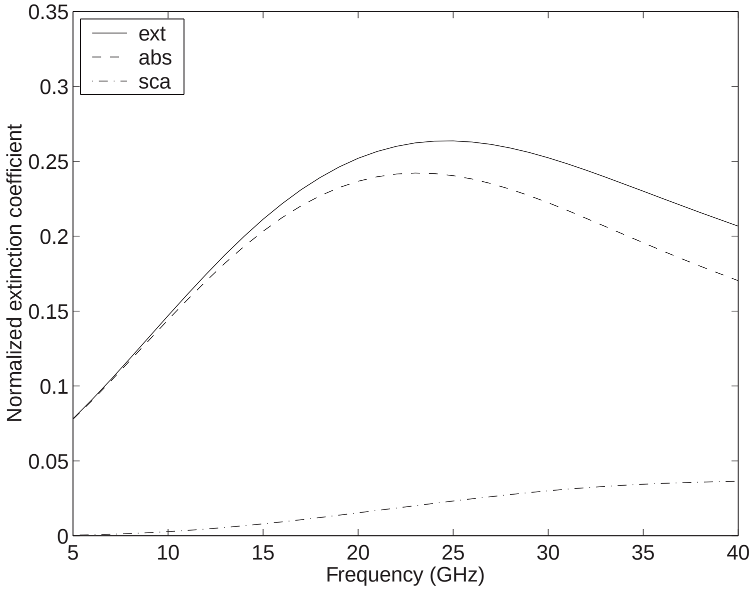

(a) Normalized extinction coefficient κ_e/k.

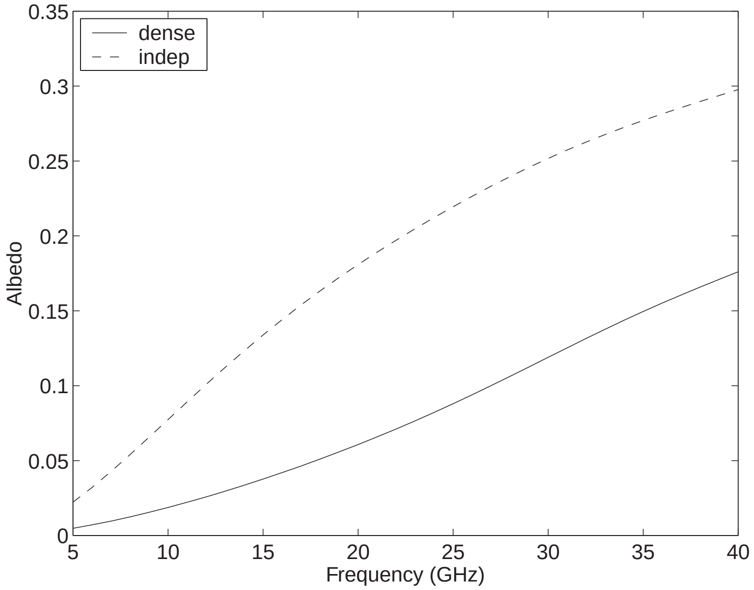

(b) Albedo $\tilde{\omega} = \kappa_s/\kappa_e$.

Figure 5-7: Extinction behavior of sea foam for $a = 2$ mm, $\delta/a = 0.03$, and fractional volume of 0.2.

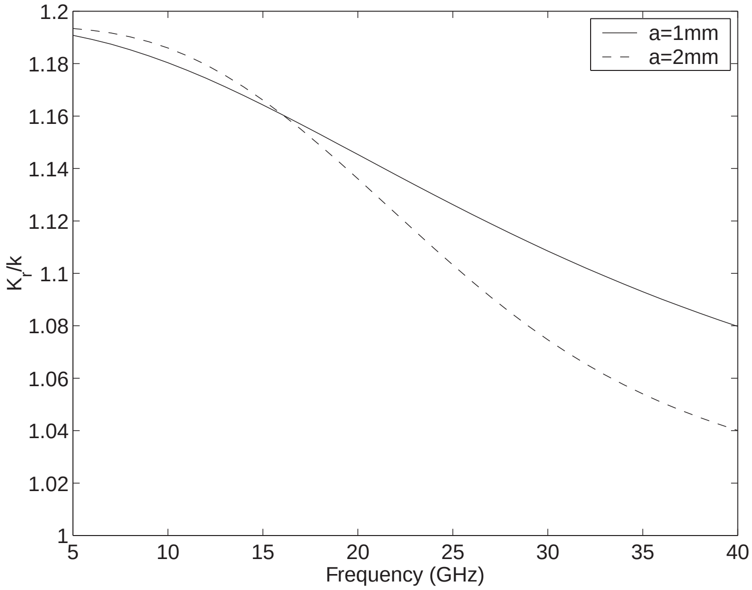

Figure 5-8: Real part of effective wavenumber as a function of frequency.

In the above equations, $C = k_B/\lambda_1^2$ with k_B being the Boltzmann constant and $\lambda_1 = 2\pi/K_r$.

The boundary conditions at the two interfaces $z = 0$ and $z = -d$ are obtained by treating the foam layer as an effective medium with wavenumber equal to K_r, the real part of the effective wavenumber. Let $r_{10,\alpha}$ and $r_{12,\alpha}$ $(\alpha = v, h)$ be the Fresnel reflectivity for the interfaces $z = 0$ and $z = -d$, respectively. Then the upgoing and downgoing intensities at the interfaces are related as follows:

$$I_\alpha(z = 0, \pi - \theta) = r_{10,\alpha}(\theta) I_\alpha(z = 0, \theta) \tag{5.23}$$

$$I_\alpha(z = -d, \theta) = r_{12,\alpha}(\theta) I_\alpha(z = -d, \pi - \theta) + (1 - r_{12,\alpha}(\theta))CT \tag{5.24}$$

After the specific intensity is solved, the brightness temperature at observation angle θ_o is obtained by

$$T_\alpha(\theta_o) = \frac{1}{C_o}(1 - r_{10,\alpha}(\theta)) I_\alpha(z = 0, \theta) \tag{5.25}$$

where $C_o = k_B/\lambda_o^2$ with λ_o being the free-space wavelength. The angles θ_o and θ are related through Snell's law: $k \sin\theta_o = K_r \sin\theta$. Instead of the brightness temperature, one can also use the emissivity $e_\alpha = T_\alpha/T$.

The RT equation is an integro-differential equation and is difficult to solve analytically. However, when the albedo is small, the integral that contains the phase functions can be ignored or treated perturbatively. As we have seen in Sec. 5.3.1, for sea foam that consists of small bubbles or is being observed at the lower frequencies, the albedo is indeed quite small. In this case, one can derive the following simple closed-form expression for the brightness temperature:

$$T_\alpha(\theta_o) = T\frac{(1 - r_{01,\alpha})(1 - r_{12,\alpha}e^{-2\kappa_a d \sec\theta})}{1 - r_{01,\alpha}r_{12,\alpha}e^{-2\kappa_a d \sec\theta}} \tag{5.26}$$

For general albedo, the RT integro-differential equation can be solved numerically using the quadrature method (also known as the discrete ordinate eigenanalysis approach) [4, 10]. In the quadrature method, the angles of propagation are discretized into a finite number of values θ_j, $j = 1, \ldots, N_q$, using Gauss-Legendre quadrature rule. The z dependence is handled by setting $I_\alpha(z, \theta_j) = I_{\alpha j}e^{\lambda z}$. A set of homogeneous equations for $I_{\alpha j}$ can be derived and used to determine the eigenvalues λ and the associated eigenvectors. The arbitrary constants in the eigenvectors are fixed with the boundary conditions (5.23) and (5.24).

5.3.3 Numerical Results of Brightness Temperature

In this section, we present numerical results for the brightness temperatures from a layer of foam overlying the flat ocean surface. The results presented here are based on the following parameters: physical temperature $T = 285$ K, fractional shell thickness $\delta/a = 0.03$, and fractional volume $f_v = 0.2$.

In Figs. 5-9(a) and 5-9(b), we show the brightness temperatures (T_v and T_h) as a function of observation angle at frequencies 19 GHz and 37 GHz, respectively. For these results, the radius of the bubble is $a = 1$ mm, and the thickness of the foam layer is $d = 1$ cm. As shown in Fig. 5-6, the albedo for this choice of parameters is very small, and we can use Eq. (5.26) to compute the brightness temperatures. The radiative transfer parameters, which can be obtained from Fig. 5-4, Fig. 5-6, and Fig. 5-8, are listed in Table 5.1 for easy reference. Also shown for comparison in Fig. 5-9 are the brightness temperatures for the plain ocean surface (i.e., without the foam coverage). Compared with the emission from plain ocean surface, the foam emission (*i*) has much larger emissivities and (*ii*) has smaller polarization differences. The main reason for these characteristics is that the foam, due to its porous nature, reflects microwave radiation weakly and hence absorbs (and emits) much more than the plain ocean surface.

Fig. 5-10 shows the brightness temperature at normal observation angle as a function of frequency. The vertical and horizontal polarizations have the same value due to azimuthal symmetry. For the foam, we illustrate with four sets of parameters corresponding to different combinations of bubble radius ($a = 1$ mm and $a = 2$ mm) and layer thickness ($d = 5$ mm and $d = 1$ cm). The four curves show very similar frequency dependence, with thicker layer giving larger brightness temperature. The brightness temperature increases monotonously with frequency and appears to saturate at higher frequencies. Also shown for comparison are the brightness temperatures from the plain ocean surface and from Stogryn's empirical formula for foam emission [93]. Curiously, the plain ocean and the empirical formula for foam both display a linear dependence on frequency. This is not the case from the foam emission model.

f (GHz)	K_r/k	κ_a/k	ε_s
19	1.149	0.190	$30.43 + i77.04$
37	1.087	0.200	$13.85 + i25.08$

Table 5.1: Radiative transfer parameters at 19 and 37 GHz for $a = 1$ mm and $f_v = 0.2$.

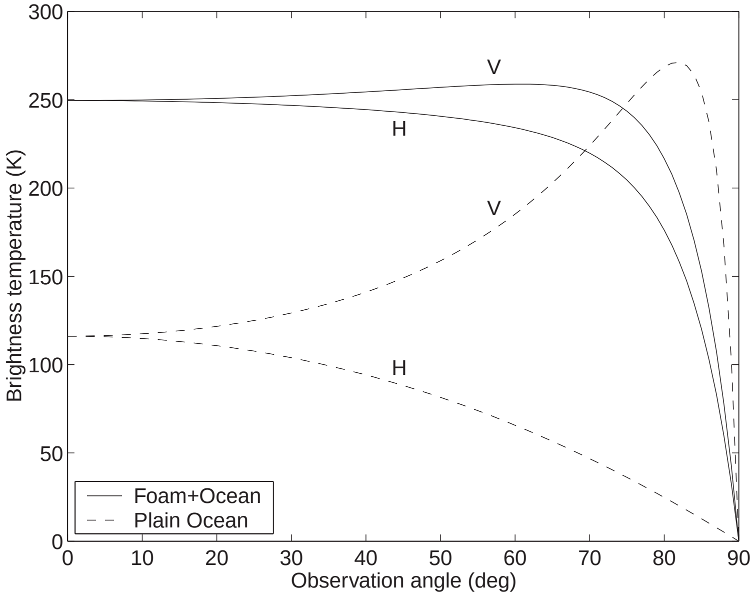

(a) $f = 19$ GHz.

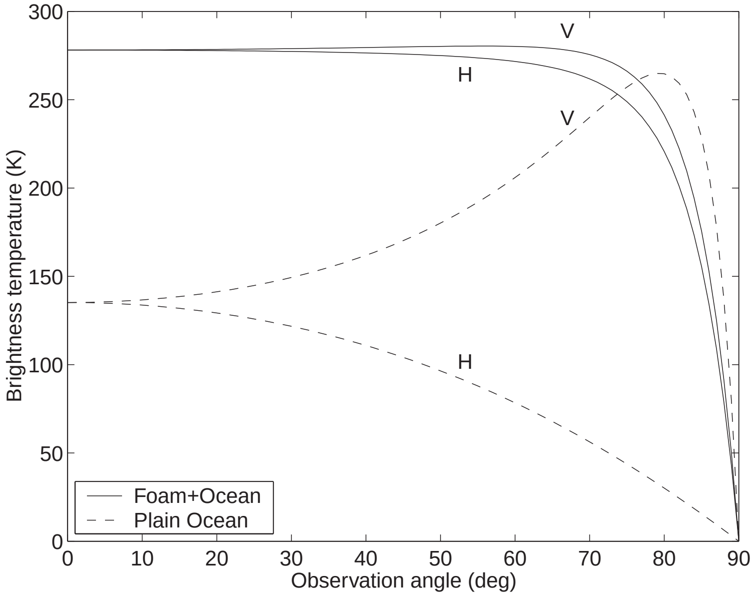

(b) $f = 37$ GHz.

Figure 5-9: Brightness temperatures as a function of observation angle.

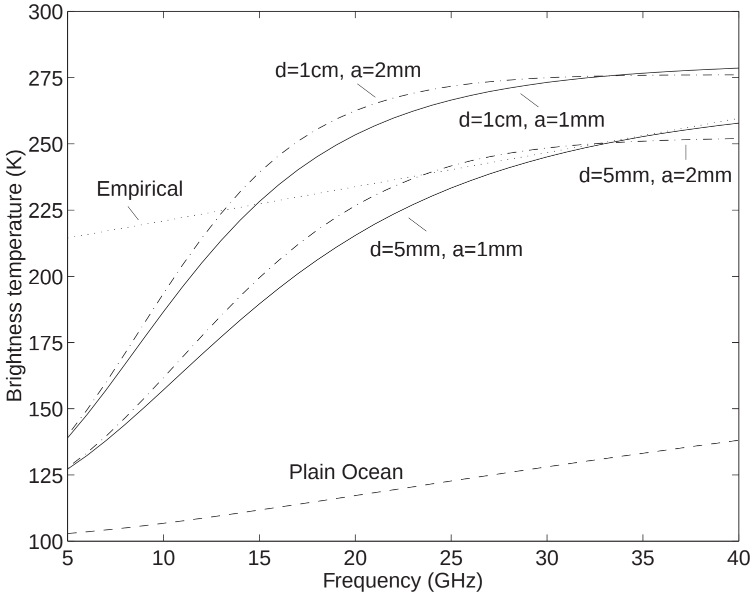

Figure 5-10: Brightness temperature at nadir as a function of frequency.

5.4 Effects of Large-Scale Ocean Waves

So far, the foam emission has been calculated by assuming that the underlying ocean surface is flat. However, the actual wind-driven ocean surface contains multiscale roughness that can affect the scattering and emission processes significantly. In this section, we take into account the rough ocean surface partially by incorporating the geometric tilting effects of the large-scale ocean waves. By large-scale roughness, we refer to the case where the the ocean surface height varies only by a small amount over the distance of the electromagnetic wavelength. This means that locally, we can approximate the rough surface with a tangent plane at that location (Fig. 5-11). Now, since the tangent plane is a flat, the problem has already been solved in the local coordinates with respect to the tangent plane. Thus the only remaining task is to transform the solution in local coordinates to the global (radiometer) coordinates. The geometric tilting approach is the basic idea behind the widely used two-scale model for rough surface scattering and emission [92, 99].

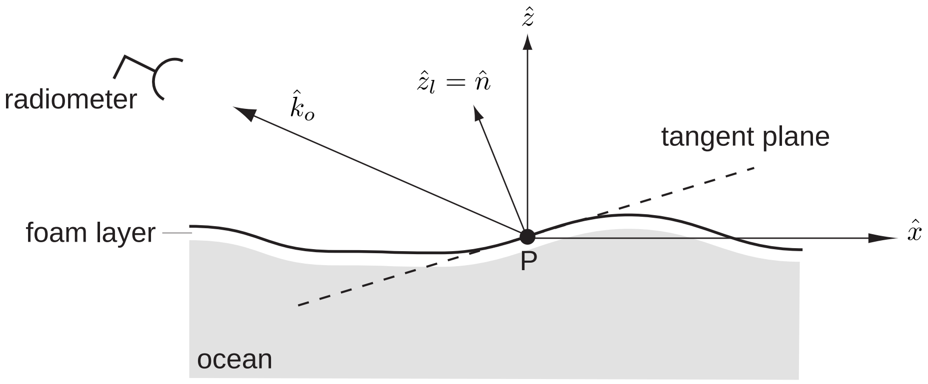

Figure 5-11: Foam layer on large-scale rough ocean surface. Locally (say point P), the foam layer can be considered to be flat on the tangent plane with local zenith direction $\hat{z}_l$ equal to the surface normal $\hat{n}$.

Single tilted facet

Let us first consider a single facet with slopes s_x and s_y. Let $\hat{n}$ be the the unit vector normal to the surface. The transformation from local to global coordinates consists of two parts. The first is to relate global observation angles to local angles. The second is to relate the global polarization vectors to local polarization vectors.

We set up the local coordinate system $(\hat{x}_l, \hat{y}_l, \hat{z}_l)$ with $\hat{z}_l = \hat{n}$ and $\hat{x}_l$ in the $\hat{x}$-$\hat{z}$ plane. Then

$$\hat{z}_l = \hat{n} = \frac{-s_x\hat{x} - s_y\hat{y} + \hat{z}}{\sqrt{1 + s_x^2 + s_y^2}} \tag{5.27}$$

$$\hat{x}_l = \frac{\hat{y} \times \hat{z}_l}{|\hat{y} \times \hat{z}_l|} \tag{5.28}$$

$$\hat{y}_l = \hat{z}_l \times \hat{x}_l \tag{5.29}$$

Let $\hat{k}_o$ be the emission or observation direction. One can write

$$\hat{k}_o = \sin\theta_o \cos\phi_o \hat{x} + \sin\theta_o \sin\phi_o \hat{y} + \cos\theta_o \hat{z} \tag{5.30}$$

$$= \sin\theta_l \cos\phi_l \hat{x}_l + \sin\theta_l \sin\phi_l \hat{y}_l + \cos\theta_l \hat{z}_l \tag{5.31}$$

where θ_o and ϕ_o denote the angles in the global coordinate system while θ_l and ϕ_l denote the angles in the local coordinates. Using (5.27)–(5.29) in (5.31) and matching the components with (5.30) allow us to relate the angles in the two coordinate systems.

The polarization vectors are defined as

$$\hat{h} = \frac{\hat{z} \times \hat{k}_o}{|\hat{z} \times \hat{k}_o|} \tag{5.32}$$

$$\hat{v} = \hat{h}_o \times \hat{k}_o \tag{5.33}$$

for the global coordinates. For local coordinates, the polarization vectors $\hat{h}_l$ and $\hat{v}_l$ are defined similarly with $\hat{z} \to \hat{z}_l$ and $\hat{k}_o \to \hat{k}_l$. Thus the electric field is $\overline{E} = E_v \hat{v} + E_h \hat{h} = E_{vl} \hat{v}_l + E_{hl} \hat{h}_l$. Let $\cos\alpha = \hat{h} \cdot \hat{h}_l$ and $\sin\alpha = \hat{v} \cdot \hat{h}_l$. Then

$$\begin{bmatrix} E_v \\ E_h \end{bmatrix} = \begin{bmatrix} \cos\alpha & \sin\alpha \\ -\sin\alpha & \cos\alpha \end{bmatrix} \begin{bmatrix} E_{vl} \\ E_{hl} \end{bmatrix} \tag{5.34}$$

Using (5.34), the Stokes vector transform as follows:

$$\overline{I}(\hat{k}_o; s_x, s_y) = \begin{bmatrix} T_v \\ T_h \\ U \\ V \end{bmatrix} = \begin{bmatrix} \cos^2\alpha & \sin^2\alpha & \cos\alpha\sin\alpha & 0 \\ \sin^2\alpha & \cos^2\alpha & -\cos\alpha\sin\alpha & 0 \\ -\sin 2\alpha & \sin 2\alpha & \cos 2\alpha & 0 \\ 0 & 0 & 0 & 1 \end{bmatrix} \begin{bmatrix} T_{vl} \\ T_{hl} \\ U_l \\ V_l \end{bmatrix} \tag{5.35}$$

For foam-covered ocean, $U_l = V_l = 0$. It is interesting to note that even though $U_l = 0$, the third Stokes parameter can become nonzero in the tilted system when $T_{vl} \neq T_{hl}$. On the other hand, it is impossible to produce a nonzero fourth Stokes parameter V upon a coordinate transformation. This is because V is related to circularly polarized waves [4], which cannot be obtained from coordinate transformation of linearly polarized waves.

Averaging over slope distribution

When facets of different slopes are present with probability distribution $p(s_x, s_y)$, the final observed Stokes vector is an average of contributions from all possible slopes.

$$\overline{I}_o(\hat{k}_o) = \int ds_y \int ds_x \Lambda(\hat{k}_o; s_x, s_y) p(s_x, s_y) \overline{I}(\hat{k}_o; s_x, s_y) \tag{5.36}$$

The extra factor Λ accounts for shadowing and area projection effects. The latter is needed because a facet presented face on towards the observation direction is more likely to be observed than a facet being presented edge-on. It is straightforward to show that [99]

$$\Lambda(\hat{k}_o; s_x, s_y) = \begin{cases} 1 - L & \text{if } L < 1 \\ 0 & \text{otherwise} \end{cases} \tag{5.37}$$

where $L = \tan\theta_o(s_x \cos\phi_o + s_y \sin\phi_o)$.

For $p(s_x, s_y)$, we use the Cox-Munk slope distribution [100] for a wind-driven ocean surface, which is determined empirically from optical measurements of the Sun's reflection off the sea surface. We use $\hat{x}$ to denote the wind vector direction and $\hat{y}$ to denote the crosswind direction. Let σ_x and σ_y be the rms slopes. Then the slope probability distribution is given as

$$\begin{aligned} p(s_x, s_y) = & \frac{1}{2\pi\sigma_x\sigma_y} \exp\left[-\frac{1}{2}(\tilde{s}_x^2 + \tilde{s}_y^2)\right] \\ & \times \left[1 - \frac{1}{2}c_{21}(\tilde{s}_y^2 - 1)\tilde{s}_x - \frac{1}{6}c_{03}(\tilde{s}_x^2 - 3)\tilde{s}_x + \frac{1}{24}c_{40}(\tilde{s}_y^4 - 6\tilde{s}_y^2 + 3)\right. \\ & \left. + \frac{1}{4}c_{22}(\tilde{s}_y^2 - 1)(\tilde{s}_x^2 - 1) + \frac{1}{24}c_{04}(\tilde{s}_x^4 - 6\tilde{s}_x^2 + 3) + \cdots\right] \end{aligned} \tag{5.38}$$

where $\tilde{s}_x = s_x/\sigma_x$ and $\tilde{s}_y = s_y/\sigma_y$. The rms slopes are related to the wind speed through the formulae $\sigma_x^2 = 0.00316w$ and $\sigma_y^2 = 0.003 + 0.00192w$, where w is wind speed (in m/s) at a height of 12.7 m above the mean surface. The c coefficients are: $c_{21} = 0.01 - 0.0086w$, $c_{03} = 0.04 - 0.033w$, $c_{40} = 0.40$, $c_{22} = 0.12$, $c_{04} = 0.23$. The Cox-Munk distribution is anisotropic. Moreover, it is asymmetric in the upwind-downwind direction, i.e., $p(s_x, s_y) \neq p(-s_x, s_y)$. The amount of asymmetry is indicated by the skewness coefficients c_{21} and c_{03}, which depend on wind speed.

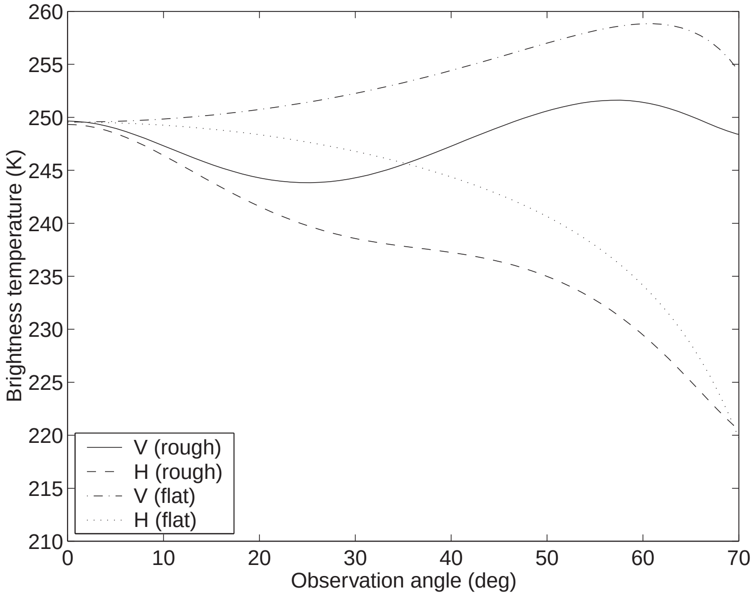

Figure 5-12: Brightness temperatures as a function of polar angle at $f = 19$ GHz.

In the following, we illustrate the brightness temperatures from a foam-covered rough ocean surface at $f = 19$ GHz. We choose the parameters to be the same as in Fig. 5-9(a). A wind speed of $w = 15$ m/s is used, and the integrations over slopes are truncated at $5\sigma_x$ for s_x and $5\sigma_y$ for s_y. As a result of the tilting, the angular dependence of the brightness temperatures is modified. Fig. 5-12 shows the variation of T_v and T_h as a function of the polar angle θ_o at azimuthal angle $\phi_o = 180°$. The flat surface results of Fig. 5-9(a) are also plotted for comparison. One interesting effect of the tilting is that both T_v and T_h drops more rapidly away from nadir. This kind of behavior agrees qualitatively with early foam emission measurements (see [93] and references therein).

The two-dimensional anisotropic rough surface also introduces azimuthal variations in the observed sea foam emission. Fig. 5-13 shows how T_v, T_h, and U vary with azimuthal angle $\phi = 180° - \phi_o$. (Note that ϕ corresponds to the radiometer looking direction and is used instead of ϕ_o to conform with customary usage in the literature [92].) The polar angle is fixed at $\theta_o = 30°$. The left-panel in Fig. 5-13 corre-

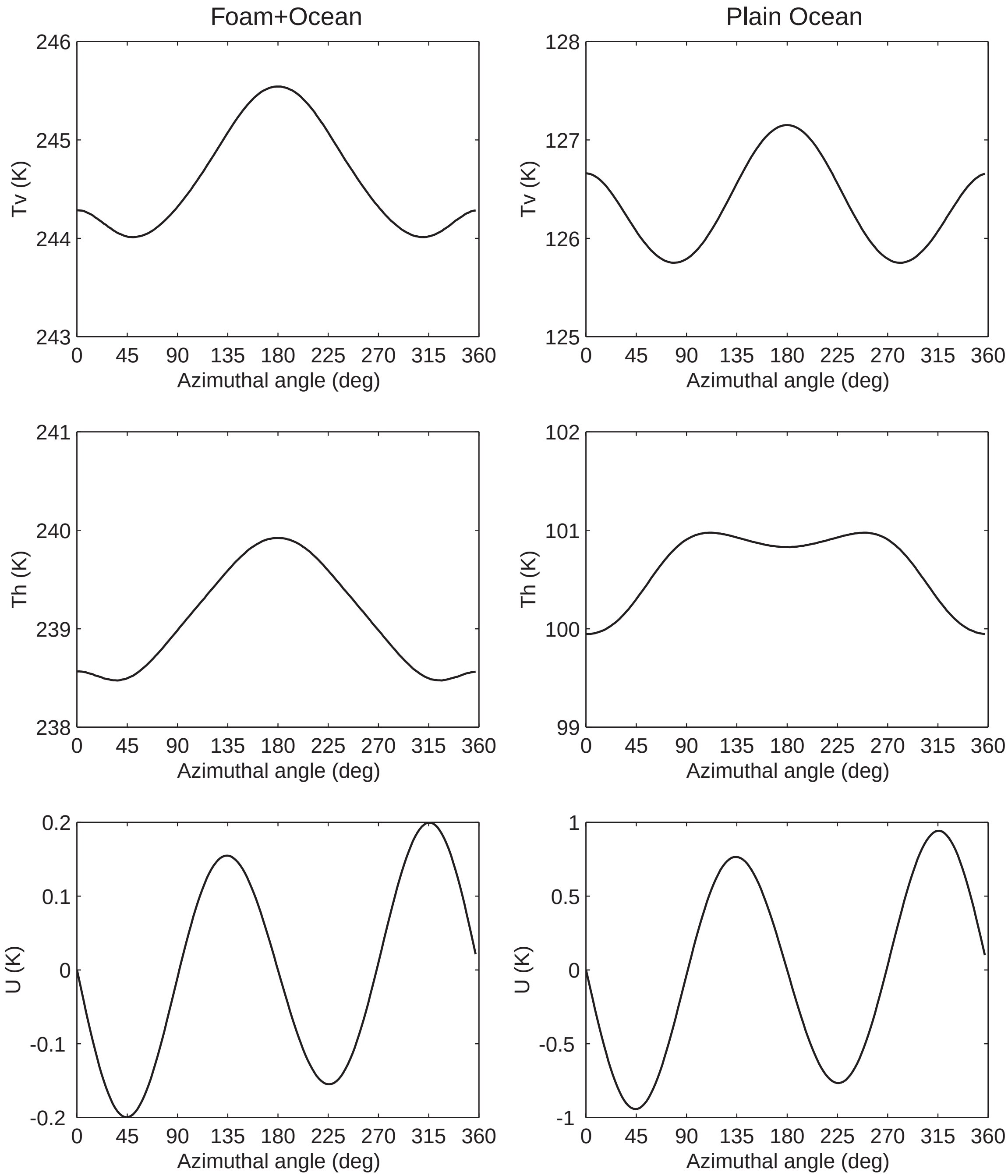

Figure 5-13: Brightness temperatures as a function of azimuthal angle at $f = 19$ GHz.

sponds to the foam-covered ocean, while the right-panel corresponds to plain ocean. The amplitudes of the azimuthal variations are small but measurable. Note that because of the upwind-downwind asymmetry in the Cox-Munk slope distribution, the brightness temperatures at $\phi = 0°$ and $\phi = 180°$ are not the same.

The plain ocean has U emission that is five times that of the foam-covered ocean. This is because the larger polarization difference of local emission $(T_{vl} - T_{hl})$ in the plain ocean surface case. Despite the difference in amplitudes, the azimuthal dependences of the U term for both cases are remarkably similar. The use of polarimetric brightness temperatures from satellite observations in deducing ocean wind vector information is an active area of research. The ability to predict the azimuthal variation of the brightness temperatures is important especially in inferring wind direction.

5.5 Conclusions

In this chapter, an electromagnetic model for the polarimetric emission of sea foam is presented where the foam is made up of air bubbles with thin outer layers of sea water. Because of uncertainties in bubble sizes and distributions, we seek a volume scattering formulation which has no strict limitations on particle size and concentration. Thus we use the quasi-crystalline approximation (QCA) based dense medium radiative transfer (DMRT) theory.

In this theory, QCA is first used to solve for the radiative transport parameters. By using a T-matrix formulation of QCA, exact Mie scattering is incorporated in the multiple scattering equations. Thus the solution is not limited to low-frequency or small particle size. We study the dispersion characteristics of densely packed bubble scatterers and compare the QCA-Mie solution with the low-frequency approximation. In particular, we contrast the dispersion characteristics of scatterers that are slightly lossy and ones that are very lossy. The latter is more typical of the foam bubbles, which contain sea water that has a large imaginary part in its permittivity. The lossy nature of the bubbles suppresses scattering resonance features present in the low-loss case.

The QCA solution allows us to investigate the extinction behavior of sea foam over a broad range of frequencies. Since bubbles are very lossy, the extinction characteristics are dominated by absorption. However, for larger bubbles and higher frequencies, scattering attenuation could also become an important factor. The absorption coefficient, scattering coefficient, and scattering phase matrix obtained using QCA are then used as inputs in the radiative transfer (RT) equation. A general exact numerical solution based on the quadrature method has been implemented. However, when the albedo is small, we can neglect the scattering phase matrix and derive a simple expression for the observed brightness temperatures. We demonstrate the high emissivities of the sea foam compared with plain ocean surface and study their angular and frequency dependences.

Finally, we also consider the effects of foam on a *rough* ocean surface using a tilting model based on the tangent-plane approximation. In this model, the polarimetric emission from the foam on a tilted facet can be obtained from the foam on a flat surface through coordinate transformation. In actual ocean surface, a distribution of sea slopes exists, and we must average the contributions from facets with different slopes. We use the Cox-Munk slope distribution to perform the averaging. The Cox-Munk slope distribution also allows us to relate the observed brightness temperature to the wind speed. The roughness of the underlying sea surface introduces interesting angular dependences, both in terms of polar angle and azimuthal angle. This has implications in the application of passive remote sensing of ocean for deducing wind speed and direction.

Chapter 6

Summary

In this thesis, we study several problems that deal with electromagnetic wave scattering in discrete random medium. The kind of scatterers we consider include conducting and permeable spheroids (Chapter 2), dielectric spheroids (Chapters 3 and 4), and layered dielectric spheres (Chapter 5). The methods used include separation of variables, method of moments, and analytical multiple scattering wave theory. While the overall thesis is theoretically oriented, the work done can be applied directly in applications that include discrimination of buried unexploded ordnance (UXO) (Chapter 2), scattering and emission from sea ice and vegetation (Chapters 3 and 4), and thermal emission from a foam-covered ocean surface (Chapter 5).

In Chapter 2, the quasi-magnetostatic solution for a conducting and permeable spheroid under arbitrary excitation is obtained using both an exact formulation and an approximation theory. The exact formulation relies on vector spheroidal wavefunction expansion of the internal field. The non-orthogonality of the angular spheroidal wavefunctions for different wavenumbers does not allow us to match the expansion coefficients term-by-term. As a result, a linear system of equations must be solved for the expansion coefficients. Despite some lack of elegance in the formulation, this method performs very well for low to moderate frequencies. However, it breaks down numerically at a frequency parameter of $|c_1| \approx 30$. Since c_1 is proportional to the focal length of the spheroid, the breakdown of the solution occurs at a lower frequency for a more elongated spheroid. This is somewhat discouraging because we are interested in a broadband response. To obtain accurate results at high frequency, an approximate theory is developed that avoids any reference to the spheroidal wavefunction. By taking advantage of the fact that the external field could manage to penetrate slightly into the spheroid at high frequency, we obtain expressions of the internal field just inside the surface as a function of the external field. A set of linear equations is obtained for the external field which presents no numerical difficulty with respect to frequency or elongation. We call this approximate theory the small penetration-depth approximation (SPA). Even though the SPA is initially developed to be used for high frequency, it is found to give accurate broadband results for spheroids with large permeability. The simplicity of the SPA coupled with its accuracy makes it an attractive forward model for model-based inversion schemes. By neglecting mutual interactions, the frequency responses from a collection of spheroids with different sizes, elongations, and orientations are also investigated. The results demonstrate that the frequency responses from spheroids of different species could overlap, making discrimination difficult.

In Chapter 3, multiple scattering of electromagnetic waves by densely packed dielectric spheroids is studied using numerical simulations. Recognizing the importance of particle positions on the collective scattering response, we first describe the Metropolis Monte Carlo method used to generate physically realistic configurations of hard prolate spheroids. Results of pair distribution functions show that the particle positions are far from uncorrelated. The correlation of particle positions affect the coherent addition of scattered waves from the spheroids. This fact is neglected in the independent scattering approximation which is widely used in the classical radiative transfer theory. By formulating the problem in terms of volume integral equation for the electric field and assuming that the spheroidal particles have sizes small compared to the electromagnetic wavelength, a method of moment (MoM) solution is provided.

In the MoM solution, the unknown electric field inside each spheroid is expanded in terms of electrostatic multipole basis functions. Reasonably good results can be obtained by keeping only the three dipole basis functions and assuming point interactions between two spheroids. Numerical results are presented in terms of scattering coefficient, scattering phase matrix, and absorption coefficient. These are important input physics for equations for describing radiative transport in a random medium. It is found that for appreciable fractional volume, the independent approximation overestimates the scattering coefficient and underestimates the absorption coefficient. The discrepancy also tends to increase as a function of elongation ratio. Results for the phase matrix elements show that depolarization effects become more significant as a result of multiple scattering.

In Chapter 4, the multiple scattering of densely packed dielectric prolate spheroids is studied using analytical wave theory. Unlike the Monte Carlo simulations, only spheroids with aligned orientation are considered here. The main constraint is the lack of an analytical pair distribution function for spheroids with general orientation distribution. The low-frequency solutions of QCA and QCA-CP are derived, giving the average Green's function and dispersion relation. For QCA-CP, a low-frequency expansion of the uniaxial Green's function is required. The leading real part of the uniaxial Green's function yields a polarization tensor that corresponds to a slightly less elongated spheroid, while the leading imaginary part gives rise to anisotropic radiative loss. The effective permittivities obtained using QCA and QCA-CP are compared with the Maxwell-Garnett mixing formula. We find that by neglecting the radiative loss term, QCA gives an identical expression to the mixing formula while QCA-CP gives a slightly larger value. We also compare the extinction coefficients obtained using QCA and QCA-CP with those of Monte Carlo simulations computed using the methods discussed in Chapter 3. Both methods are found to perform quite well, especially for smaller fractional volumes. At higher fractional volumes, higher order statistics of particle positions, which are not taken into account in QCA and

QCA-CP, might become important.

In Chapter 5, an electromagnetic model for the polarimetric emission of sea foam is presented where the foam is made up of air bubbles coated with a thin layer of sea water. The QCA-based dense medium radiative transfer (DMRT) theory is used. By using a T-matrix formulation of QCA, exact Mie scattering is incorporated in the multiple scattering equations. Thus the solution is not limited to low frequency or small particle size. The QCA-Mie formulation allows us to investigate the extinction behavior of sea foam over a broad range of frequencies. Since bubbles are very lossy, the extinction characteristics are dominated by absorption. However, for larger bubbles and higher frequencies, scattering attenuation could also become an important factor. The absorption coefficient, scattering coefficient, and scattering phase matrix obtained using QCA are then used as inputs in the radiative transfer (RT) equation. We demonstrate the high emissivities of the sea foam compared with plain ocean surface and study their angular and frequency dependences. Finally, we also consider the effects of foam on large-scale ocean surface using a tilting model based on the tangent-plane approximation. In this model, the polarimetric emission from the foam on a tilted facet can be obtained from the foam on a flat surface through coordinate transformation. We then use the Cox-Munk slope distribution to perform the averaging of Stokes vector over all slopes. The resulting brightness temperatures show interesting dependences in polar angle and azimuthal angle. Thus the foam emission model presented here is capable of relating the observed brightness temperatures to the microstructure of foam as well as to ocean wind speed and direction.

Appendix A

Computational Elements in Vector Spheroidal Wavefunction Expansions

A.1 Vector Spheroidal Wavefunctions

For computational purposes, it is convenient to express the vector spheroidal wavefunctions of (2.4) and (2.5) in partially separable forms. Explicit expressions of $\overline{M}$ and $\overline{N}$ in component forms can be found in Flammer's monograph on spheroidal wavefunctions [29]. They can be manipulated to yield

$$M_{\beta;pmn} = \frac{d}{2h_\beta}\frac{dT_{pmn}}{d\phi}\widetilde{M}_{\beta;mn}(\eta,\xi) \tag{A.1}$$

$$M_{\phi;pmn} = \frac{d}{2h_\phi}T_{pmn}(\phi)\widetilde{M}_{\phi;mn}(\eta,\xi) \tag{A.2}$$

$$N_{\beta;pmn} = \frac{1}{c}\frac{d}{2h_\beta}T_{pmn}(\phi)\widetilde{N}_{\beta;mn}(\eta,\xi) \tag{A.3}$$

$$N_{\phi;pmn} = \frac{1}{c}\frac{d}{2h_\phi}\frac{dT_{pmn}}{d\phi}\widetilde{N}_{\phi;mn}(\eta,\xi) \tag{A.4}$$

where $\beta = \eta, \xi$ and h_β, h_ϕ are the metric coefficients for the prolate spheroidal coordinates:

$$h_\eta = \frac{d}{2}\sqrt{\frac{\xi^2-\eta^2}{1-\eta^2}}, \quad h_\xi = \frac{d}{2}\sqrt{\frac{\xi^2-\eta^2}{\xi^2-1}}, \quad h_\phi = \frac{d}{2}\sqrt{(1-\eta^2)(\xi^2-1)} \tag{A.5}$$

The modified vector wavefunctions in (A.1)–(A.4) can be written as:

$$\widetilde{M}_{\beta;mn}(\eta,\xi) = F^{(M)(1)}_{\beta;mn}(\xi)G^{(M)(1)}_{\beta;mn}(\eta) \tag{A.6}$$

$$\widetilde{M}_{\phi;mn}(\eta,\xi) = \frac{1}{(\xi^2-\eta^2)}\sum_{t=1}^{2} F^{(M)(t)}_{\phi;mn}(\xi)G^{(M)(t)}_{\phi;mn}(\eta) \tag{A.7}$$

$$\widetilde{N}_{\beta;mn}(\eta,\xi) = \frac{1}{(\xi^2-\eta^2)^2}\sum_{t=1}^{5} F^{(N)(t)}_{\beta;mn}(\xi)G^{(N)(t)}_{\beta;mn}(\eta) \tag{A.8}$$

$$\widetilde{N}_{\phi;mn}(\eta,\xi) = \frac{1}{(\xi^2-\eta^2)}\sum_{t=1}^{2} F^{(N)(t)}_{\phi;mn}(\xi)G^{(N)(t)}_{\phi;mn}(\eta) \tag{A.9}$$

The functions $F^{(t)}_{mn}(\xi)$ and $G^{(t)}_{mn}(\eta)$ represent the separable parts of the vector spheroidal wavefunctions. They are listed below.

For the $\overline{M}$ wavefunctions:

$$F^{(M)(1)}_{\eta;mn}(\xi) = -\xi R_{mn}(\xi) \tag{A.10}$$

$$G^{(M)(1)}_{\eta;mn}(\eta) = \frac{1}{(1-\eta^2)}S_{mn}(\eta) \tag{A.11}$$

$$F^{(M)(1)}_{\xi;mn}(\xi) = \frac{1}{(\xi^2-1)}R_{mn}(\xi) \tag{A.12}$$

$$G^{(M)(1)}_{\xi;mn}(\eta) = \eta S_{mn}(\eta) \tag{A.13}$$

$$F^{(M)(1)}_{\phi;mn}(\xi) = (\xi^2-1)\xi R_{mn}(\xi) \tag{A.14}$$

$$G^{(M)(1)}_{\phi;mn}(\eta) = (1-\eta^2)\frac{dS_{mn}}{d\eta} \tag{A.15}$$

$$F^{(M)(2)}_{\phi;mn}(\xi) = -(\xi^2-1)\frac{dR_{mn}}{d\xi} \tag{A.16}$$

$$G^{(M)(2)}_{\phi;mn}(\eta) = (1-\eta^2)\eta S_{mn}(\eta) \tag{A.17}$$

For the $\overline{N}$ wavefunctions:

$$F^{(N)(1)}_{\eta;mn}(\xi) = 2\xi(\xi^2-1)\frac{dR_{mn}}{d\xi} - (\xi^2-1)(\lambda_{mn}-c^2\xi^2)R_{mn}(\xi) + m^2R_{mn}(\xi) \tag{A.18}$$

$$G^{(N)(1)}_{\eta;mn}(\eta) = \eta S_{mn}(\eta) \tag{A.19}$$

$$F^{(N)(2)}_{\eta;mn}(\xi) = -(\lambda_{mn}-c^2\xi^2)R_{mn}(\xi) \tag{A.20}$$

$$G^{(N)(2)}_{\eta;mn}(\eta) = (1-\eta^2)\eta S_{mn}(\eta) \tag{A.21}$$

$$F^{(N)(3)}_{\eta;mn}(\xi) = m^2(\xi^2-1)R_{mn}(\xi) \tag{A.22}$$

$$G^{(N)(3)}_{\eta;mn}(\eta) = \frac{1}{(1-\eta^2)}\eta S_{mn}(\eta) \tag{A.23}$$

$$F^{(N)(4)}_{\eta;mn}(\xi) = (\xi^2-1)^2\left[\xi\frac{dR_{mn}}{d\xi} + R_{mn}(\xi)\right] \tag{A.24}$$

$$G^{(N)(4)}_{\eta;mn}(\eta) = \frac{dS_{mn}}{d\eta} \tag{A.25}$$

$$F^{(N)(5)}_{\eta;mn}(\xi) = \xi(\xi^2-1)\frac{dR_{mn}}{d\xi} + (3\xi^2-1)R_{mn}(\xi) \tag{A.26}$$

$$G^{(N)(5)}_{\eta;mn}(\eta) = (1-\eta^2)\frac{dS_{mn}}{d\eta} \tag{A.27}$$

$$F^{(N)(1)}_{\xi;mn}(\xi) = (\xi^2-1)\left[-2\frac{dR_{mn}}{d\xi} + \left(\lambda_{mn} - c^2 + \frac{m^2}{\xi^2-1}\right)\xi R_{mn}(\xi)\right] \tag{A.28}$$

$$G^{(N)(1)}_{\xi;mn}(\eta) = S_{mn}(\eta) \tag{A.29}$$

$$F^{(N)(2)}_{\xi;mn}(\xi) = 3(\xi^2-1)\frac{dR_{mn}}{d\xi} + \left[(\xi^2-2)c^2 + \lambda_{mn} + \frac{m^2}{\xi^2-1}\right]\xi R_{mn}(\xi) \tag{A.30}$$

$$G^{(N)(2)}_{\xi;mn}(\eta) = (1-\eta^2)S_{mn}(\eta) \tag{A.31}$$

$$F^{(N)(3)}_{\xi;mn}(\xi) = \frac{dR_{mn}}{d\xi} + c^2\xi R_{mn}(\xi) \tag{A.32}$$

$$G^{(N)(3)}_{\xi;mn}(\eta) = (1-\eta^2)^2 S_{mn}(\eta) \tag{A.33}$$

$$F^{(N)(4)}_{\xi;mn}(\xi) = (\xi^2-1)\frac{dR_{mn}}{d\xi} - 2\xi R_{mn}(\xi) \tag{A.34}$$

$$G^{(N)(4)}_{\xi;mn}(\eta) = (1-\eta^2)\eta\frac{dS_{mn}}{d\eta} \tag{A.35}$$

$$F^{(N)(5)}_{\xi;mn}(\xi) = \frac{dR_{mn}}{d\xi} \tag{A.36}$$

$$G^{(N)(5)}_{\xi;mn}(\eta) = (1-\eta^2)^2\eta\frac{dS_{mn}}{d\eta} \tag{A.37}$$

$$F^{(N)(1)}_{\phi;mn}(\xi) = (\xi^2 - 1)\left[\xi \frac{dR_{mn}}{d\xi} + R_{mn}(\xi)\right] \tag{A.38}$$

$$G^{(N)(1)}_{\phi;mn}(\eta) = S_{mn}(\eta) \tag{A.39}$$

$$F^{(N)(2)}_{\phi;mn}(\xi) = R_{mn}(\xi) \tag{A.40}$$

$$G^{(N)(2)}_{\phi;mn}(\eta) = (1 - \eta^2)\left[S_{mn}(\eta) + \eta \frac{dS_{mn}}{d\eta}\right] \tag{A.41}$$

A.2 Coupling Matrices and System Matrices

The definitions for the coupling matrices are given below:

$$I_\xi(n', n) = \frac{2n'+1}{2}\,\frac{(n'-m)!}{(n'+m)!}\int_{-1}^{1} d\eta P^m_{n'}(\eta)\widetilde{M}_{\xi;mn}(\eta, \xi_o) \tag{A.42}$$

$$I_\eta(n', n) = \frac{2n'+1}{2}\,\frac{(n'-m)!}{(n'+m)!}\int_{-1}^{1} d\eta P^m_{n'}(\eta)(1-\eta^2)\widetilde{M}_{\eta;mn}(\eta, \xi_o) \tag{A.43}$$

$$I_\phi(n', n) = \frac{2n'+1}{2}\,\frac{(n'-m)!}{(n'+m)!}\int_{-1}^{1} d\eta P^m_{n'}(\eta)\widetilde{M}_{\phi;mn}(\eta, \xi_o) \tag{A.44}$$

$$J_\xi(n', n) = \frac{2n'+1}{2}\,\frac{(n'-m)!}{(n'+m)!}\int_{-1}^{1} d\eta P^m_{n'}(\eta)\widetilde{N}_{\xi;mn}(\eta, \xi_o) \tag{A.45}$$

$$J_\eta(n', n) = \frac{2n'+1}{2}\,\frac{(n'-m)!}{(n'+m)!}\int_{-1}^{1} d\eta P^m_{n'}(\eta)(1-\eta^2)\widetilde{N}_{\eta;mn}(\eta, \xi_o) \tag{A.46}$$

$$J_\phi(n', n) = \frac{2n'+1}{2}\,\frac{(n'-m)!}{(n'+m)!}\int_{-1}^{1} d\eta P^m_{n'}(\eta)\widetilde{N}_{\phi;mn}(\eta, \xi_o) \tag{A.47}$$

The explicit expressions of $\widetilde{M}_{\beta;mn}(\eta, \xi_o)$ and $\widetilde{N}_{\beta;mn}(\eta, \xi_o)$ for $\beta = \eta, \xi, \phi$ are given in Appendix I. Once they are determined, the integrals can be easily evaluated numerically by Gaussian quadrature.

The system matrices $\overline{\overline{Z}}_\beta$ and $\overline{\overline{W}}_\beta$ are given as follows. We distinguish the cases of even and odd excitations by defining

$$r_i = \begin{cases} 2i+m-2 & \text{for even excitation} \\ 2i+m-1 & \text{for odd excitation} \end{cases} \tag{A.48}$$

The matrices $\overline{\overline{Z}}_\beta$ are of size $L_T \times 2L_T$. For $i, j = 1, ..., L_T$,

$$Z_\xi(i,j) = \mu_r \left[\frac{dQ_{r_i}^m}{d\xi_o}\right]^{-1} J_\xi(r_i, r_j) \tag{A.49}$$

$$Z_\xi(i,j+L_T) = \mu_r \left[\frac{dQ_{r_i}^m}{d\xi_o}\right]^{-1} mI_\xi(r_i, r_j \pm 1) \tag{A.50}$$

$$Z_\eta(i,j) = J_\eta(r_i+1, r_j) - \gamma_{1m}(r_i+2) Q_{r_i+2}^m(\xi_o) Z_\xi(i+1,j)$$
$$+\gamma_{2m}(r_i) Q_{r_i}^m(\xi_o) Z_\xi(i-1,j) \tag{A.51}$$

$$Z_\eta(i,j+L_T) = mI_\eta(r_i+1, r_j \pm 1) - \gamma_{1m}(r_i+2) Q_{r_i+2}^m(\xi_o) Z_\xi(i+1,j+L_T)$$
$$+\gamma_{2m}(r_i) Q_{r_i}^m(\xi_o) Z_\xi(i-1,j+L_T) \tag{A.52}$$

$$Z_\phi(i,j) = mJ_\phi(r_i, r_j) - mQ_{r_i}^m(\xi_o) Z_\xi(i,j) \tag{A.53}$$

$$Z_\phi(i,j+L_T) = -I_\phi(r_i, r_j \pm 1) - mQ_{r_i}^m(\xi_o) Z_\xi(i,j+L_T) \tag{A.54}$$

In (A.50), (A.52), and (A.54), the upper sign is for even excitation and the lower sign is for odd excitation.

The matrices $\overline{\overline{W}}_\beta$ are of size $L_T \times L_T$. For $i, j = 1, ..., L_T$,

$$W_\xi(i,j) = -\left[\frac{dQ_{r_i}^m}{d\xi_o}\right]^{-1} \frac{dP_{r_i}^m}{d\xi_o} \delta_{ij} \tag{A.55}$$

$$W_\eta(i,j) = -\gamma_{1m}(r_i) \left[P_{r_i}^m(\xi_o)\delta_{(i+1)j} + Q_{r_i}^m(\xi_o) W_\xi(i+1,j)\right]$$
$$+\gamma_{2m}(r_i+2) \left[P_{r_i+2}^m(\xi_o)\delta_{(i-1)j} + Q_{r_i+2}^m(\xi_o) W_\xi(i-1,j)\right] \tag{A.56}$$

$$W_\phi(i,j) = -m\left[P_{r_i}^m(\xi_o)\delta_{ij} + Q_{r_i}^m(\xi_o) W_\xi(i,j)\right] \tag{A.57}$$

where δ_{ij} is the Kronecker delta.

Appendix B

Electric Dipole and Quadrupole Basis Functions

The explicit expressions for the dipole and quadrupole basis functions $\overline{f}_\alpha$ with $\alpha = 1, 2, \ldots, 8$, along with the self-patch coefficients C_α, are given in this appendix. The coordinates used here are with respect to the body axes of the spheroid. Note that for a prolate spheroid with semiaxes a and c, the focal distance is $d = 2\sqrt{c^2 - a^2}$, and the surface of the spheroid is specified by $\xi = \xi_o$ with $\xi_o = c/\sqrt{c^2 - a^2}$. The volume of the spheroid is $v = (4\pi/3)a^2c$.

From Eq. (3.19), the Laplace solutions are

$$\Phi_1 = -\eta\xi = -\left(\frac{2}{d}\right) z \tag{B.1}$$

$$\Phi_2 = -(1-\eta^2)^{1/2}(\xi^2-1)^{1/2}\cos\phi = -\left(\frac{2}{d}\right) x \tag{B.2}$$

$$\Phi_3 = -(1-\eta^2)^{1/2}(\xi^2-1)^{1/2}\sin\phi = -\left(\frac{2}{d}\right) y \tag{B.3}$$

$$\Phi_4 = \frac{1}{4}(3\eta^2-1)(3\xi^2-1) = -\left(\frac{2}{d}\right)^2 \frac{3}{2}\left[z^2 - \frac{1}{2}(x^2+y^2)\right] + \frac{1}{2} \tag{B.4}$$

$$\Phi_5 = -9\eta\xi(1-\eta^2)^{1/2}(\xi^2-1)^{1/2}\cos\phi = -9\left(\frac{2}{d}\right)^2 zx \tag{B.5}$$

$$\Phi_6 = -9\eta\xi(1-\eta^2)^{1/2}(\xi^2-1)^{1/2}\sin\phi = -9\left(\frac{2}{d}\right)^2 zy \tag{B.6}$$

$$\Phi_7 = -9(1-\eta^2)(\xi^2-1)\cos 2\phi = -9\left(\frac{2}{d}\right)^2 (x^2-y^2) \tag{B.7}$$

$$\Phi_8 = -9(1-\eta^2)(\xi^2-1)\sin 2\phi = -18\left(\frac{2}{d}\right)^2 xy \tag{B.8}$$

The normalization factors of (3.24) give

$$N_1 = N_2 = N_3 = \left(\frac{2}{d}\right)^2 v \tag{B.9}$$

$$N_4 = \left(\frac{2}{d}\right)^4 \frac{9}{10} v(a^2+2c^2) \tag{B.10}$$

$$N_5 = N_6 = \left(\frac{2}{d}\right)^4 \frac{81}{5} v(a^2+c^2) \tag{B.11}$$

$$N_7 = N_8 = \left(\frac{2}{d}\right)^4 (18)^2 \frac{2}{5} va^2 \tag{B.12}$$

Thus the normalized basis functions are, in Cartesian coordinates,

$$\overline{f}_1 = \frac{1}{\sqrt{v}}\hat{z} \tag{B.13}$$

$$\overline{f}_2 = \frac{1}{\sqrt{v}}\hat{x} \tag{B.14}$$

$$\overline{f}_3 = \frac{1}{\sqrt{v}}\hat{y} \tag{B.15}$$

$$\overline{f}_4 = \sqrt{\frac{5}{2v(a^2+2c^2)}}\,(2z\hat{z} - x\hat{x} - y\hat{y}) \tag{B.16}$$

$$\overline{f}_5 = \sqrt{\frac{5}{v(a^2+c^2)}}\,(x\hat{z} + z\hat{x}) \tag{B.17}$$

$$\overline{f}_6 = \sqrt{\frac{5}{v(a^2+c^2)}}\,(y\hat{z} + z\hat{y}) \tag{B.18}$$

$$\overline{f}_7 = \sqrt{\frac{5}{2va^2}}\,(x\hat{x} - y\hat{y}) \tag{B.19}$$

$$\overline{f}_8 = \sqrt{\frac{5}{2va^2}}\,(y\hat{x} + x\hat{y}) \tag{B.20}$$

From (3.43), the self-patch coefficients can be obtained. They are given by

$$C_1 = -(\varepsilon_s - 1)\left(\xi_o^2 - 1\right)\left[\frac{\xi_o}{2}\ln\left(\frac{\xi_o + 1}{\xi_o - 1}\right) - 1\right] + i(\varepsilon_s - 1)\frac{2}{3}k^3 v \tag{B.21}$$

$$C_2 = C_3 = \frac{1}{2}(\varepsilon_s - 1)\xi_o\left[\frac{\xi_o^2 - 1}{2}\ln\left(\frac{\xi_o + 1}{\xi_o - 1}\right) - \xi_o\right] + i(\varepsilon_s - 1)\frac{2}{3}k^3 v \tag{B.22}$$

$$C_4 = -(\varepsilon_s - 1)\frac{3\xi_o}{2}\left(\xi_o^2 - 1\right)\left[\frac{1}{2}\left(3\xi_o^2 - 1\right)\ln\left(\frac{\xi_o + 1}{\xi_o - 1}\right) - 3\xi_o\right] \tag{B.23}$$

$$C_5 = C_6 = (\varepsilon_s - 1)\frac{(\xi_o^2 - 1)}{2}\left(2\xi_o^2 - 1\right)\left[\frac{3\xi_o}{2}\ln\left(\frac{\xi_o + 1}{\xi_o - 1}\right) - \frac{3\xi_o^2 - 2}{\xi_o^2 - 1}\right] \tag{B.24}$$

$$C_7 = C_8 = -(\varepsilon_s - 1)\left(\frac{\xi_o^2 - 1}{4}\right)\xi_o\left[\frac{3}{2}\left(\xi_o^2 - 1\right)\ln\left(\frac{\xi_o + 1}{\xi_o - 1}\right) - \frac{3\xi_o^3 - 5\xi_o}{\xi_o^2 - 1}\right] \tag{B.25}$$

Appendix C

Dyadic Green's Function for Uniaxial Medium

In this appendix, we derive the low-frequency limit of the dyadic Green's function for an uniaxial medium. Consider a homogeneous uniaxial medium with permittivity tensor given by

$$\overline{\overline{\epsilon}} = \epsilon \begin{pmatrix} \varepsilon_a & 0 & 0 \\ 0 & \varepsilon_a & 0 \\ 0 & 0 & \varepsilon_c \end{pmatrix} \tag{C.1}$$

The relative permittivity is $\overline{\overline{\varepsilon}} = \overline{\overline{\epsilon}}/\epsilon$. The dyadic Green's function satisfies the vector wave equation

$$\nabla \times \nabla \times \overline{\overline{G}}(\overline{r}, \overline{r}') - k^2\, \overline{\overline{\varepsilon}}\, \overline{\overline{G}}(\overline{r}, \overline{r}') = \overline{\overline{I}}\delta(\overline{r} - \overline{r}') \tag{C.2}$$

where $k = \omega\sqrt{\epsilon\mu}$. In the spectral domain, the dyadic Green's function can be written as

$$\overline{\overline{G}}(\overline{r}, \overline{r}') = \int \frac{d\overline{p}}{(2\pi)^3} e^{i\overline{p}\cdot(\overline{r}-\overline{r}')}\, \overline{\overline{G}}(\overline{p}) \tag{C.3}$$

Putting (C.3) into (C.2), we obtain

$$\overline{\overline{G}}^{-1}(\overline{p}) = p^2(\overline{\overline{I}} - \hat{p}\,\hat{p}) - k^2\overline{\overline{\varepsilon}} \tag{C.4}$$

For the special case of isotropic medium, $\overline{\overline{\varepsilon}} = \overline{\overline{I}}$. Then

$$\overline{\overline{G}}_o^{-1}(\overline{p}) = (p^2 - k^2)\overline{\overline{I}} - \overline{p}\,\overline{p} \tag{C.5}$$

In component form,

$$\overline{\overline{G}}^{-1}(\overline{p}) = \begin{pmatrix} p^2 - p_x^2 - k^2\varepsilon_a & -p_x p_y & -p_x p_z \\ -p_y p_x & p^2 - p_y^2 - k^2\varepsilon_a & -p_y p_z \\ -p_z p_x & -p_z p_y & p^2 - p_z^2 - k^2\varepsilon_c \end{pmatrix} \tag{C.6}$$

The dispersion relation for the characteristic waves can be found by setting

$$\det \overline{\overline{G}}^{-1}(\overline{p}) = 0 \tag{C.7}$$

which yields

$$\frac{1}{\varepsilon_a} p^2 = k^2 \tag{C.8}$$

$$\frac{1}{\varepsilon_c}(p_x^2 + p_y^2) + \frac{1}{\varepsilon_a} p_z^2 = k^2 \tag{C.9}$$

Eqs. (C.8) and (C.9) give the dispersion relations that correspond to the familiar ordinary and extraordinary waves of an uniaxial crystal [101].

The Fourier integral in (C.3) can be performed to give a closed form expression for the coordinate representation of the dyadic Green's function [102, 103].

$$\overline{\overline{G}}(\overline{r}, \overline{r}') = \frac{1}{4\pi\sqrt{\varepsilon_a}} \left[\left(\overline{\overline{A}} + \frac{1}{k^2} \nabla\,\nabla \right) \frac{e^{ikR_e}}{R_e} + \overline{\overline{F}}_1(\overline{R}) + \overline{\overline{F}}_2(\overline{R}) \right] \tag{C.10}$$

where

$$\overline{\overline{F}}_1(\overline{R}) = \left[\varepsilon_a \frac{e^{ikR_o}}{R_o} - \varepsilon_c \frac{e^{ikR_e}}{R_e} \right] \frac{(\overline{R} \times \hat{z})(\overline{R} \times \hat{z})}{|\overline{R} \times \hat{z}|^2} \tag{C.11}$$

$$\overline{\overline{F}}_2(\overline{R}) = \frac{e^{ikR_o} - e^{ikR_e}}{ik|\overline{R} \times \hat{z}|^2} \left[\overline{\overline{I}} - \hat{z}\hat{z} - 2\frac{(\overline{R} \times \hat{z})(\overline{R} \times \hat{z})}{|\overline{R} \times \hat{z}|^2} \right] \tag{C.12}$$

$$R_o = \sqrt{\varepsilon_a} R \tag{C.13}$$

$$R_e = \left[\overline{R}^t \cdot \overline{\overline{A}} \cdot \overline{R} \right]^{1/2} \tag{C.14}$$

and

$$\overline{\overline{A}} = \begin{pmatrix} \varepsilon_c & 0 & 0 \\ 0 & \varepsilon_c & 0 \\ 0 & 0 & \varepsilon_a \end{pmatrix} \tag{C.15}$$

Similar to the isotropic Green's function, the uniaxial Green's function contains a non-integrable source singularity at $\overline{r} = \overline{r}'$ as a result of the term

$$\frac{1}{4\pi\sqrt{\varepsilon_a}} \nabla \nabla \frac{e^{ikR_e}}{R_e} \tag{C.16}$$

In the low-frequency limit, this gives rise to the leading real part of the Green's function. Let

$$g_e(R_e) = \frac{1}{4\pi R_e} \tag{C.17}$$

$$\overline{\overline{K}} = k^2 \sqrt{\overline{\overline{\varepsilon}}} \tag{C.18}$$

$$\overline{\overline{B}} = \sqrt{\varepsilon_a} \begin{pmatrix} 1 & 0 & 0 \\ 0 & 1 & 0 \\ 0 & 0 & \alpha \end{pmatrix} \tag{C.19}$$

where

$$\alpha = \frac{\varepsilon_c}{\varepsilon_a} \tag{C.20}$$

The leading order real part of the dyadic Green's function is then given by

$$\mathrm{Re}\overline{\overline{G}}(\overline{r}, \overline{r}') \to -\overline{\overline{K}}^{-2} \overline{\overline{N}} \delta(\overline{r} - \overline{r}') \tag{C.21}$$

where

$$\overline{\overline{N}} = -\overline{\overline{B}} \int dS \hat{n} \nabla g_e(R_e) \tag{C.22}$$

with the integration taken over the surface of the exclusion volume [59]. For an exclusion volume of a prolate spheroid, it is straightforward to show that $\overline{\overline{N}}$ corresponds to the depolarization tensor $\overline{\overline{L}}$ of the isotropic Green's function [Eqs. (4.52)–(4.54)], but it is now computed with a modified eccentricity of

$$\tilde{\tilde{e}} = \sqrt{1 - \alpha \frac{a^2}{c^2}} \tag{C.23}$$

More explicitly, let $\overline{\overline{N}} = N_a \hat{x}\hat{x} + N_a \hat{x}\hat{x} + N_c \hat{z}\hat{z}$. Then

$$N_c = -\frac{(1-\tilde{\tilde{e}}^2)}{\tilde{\tilde{e}}^2}\left[1 + \frac{1}{2\tilde{\tilde{e}}}\ln\left(\frac{1-\tilde{\tilde{e}}}{1+\tilde{\tilde{e}}}\right)\right] \tag{C.24}$$

$$N_a = \frac{1}{2}(1 - L_c) \tag{C.25}$$

The leading imaginary part of the dyadic Green's function gives rise to the radiative correction. By Taylor expansion of (C.10) for small k, we get

$$\mathrm{Im}\overline{\overline{G}}(\overline{r}, \overline{r}') \to \frac{i}{6\pi}\overline{\overline{K}}\,\overline{\overline{M}} \tag{C.26}$$

where

$$\overline{\overline{M}} = \begin{pmatrix} \frac{3}{4} + \frac{\alpha}{4} & 0 & 0 \\ 0 & \frac{3}{4} + \frac{\alpha}{4} & 0 \\ 0 & 0 & \frac{1}{\sqrt{\alpha}} \end{pmatrix} \tag{C.27}$$

In contrast to the low-frequency expansion of the isotropic Green's function, the radiative correction in an uniaxial medium is anisotropic.

Bibliography

[1] H. C. van de Hulst, *Light Scattering by Small Particles*, Dover Publications, New York, 1981.

[2] M. Kerker, *The Scattering of Light and Other Electromagnetic Radiation*, Academic Press, New York, 1969.

[3] C. F. Bohren and D. R. Huffman, *Absorption and Scattering of Light by Small Particles*, Wiley, New York, 1983.

[4] L. Tsang, J. A. Kong, and K-.H. Ding, *Scattering of Electromagnetic Waves: Theories and Applications*, Wiley-Interscience, New York, 2000.

[5] M. I. Mishchenko, J. W. Hovenier, and L. D. Travis, Eds., *Light Scattering by Nonspherical Particles: Theories, Measurements, and Applications*, Academic Press, San Diego, 2000.

[6] V. Twersky, "Coherent electromagnetic waves in pair-correlated random distributions of aligned scatterers," *J. Math. Phys.*, vol. 19, no. 1, pp. 215–230, 1978.

[7] L. Tsang and J. A. Kong, "Multiple scattering of electromagnetic waves by random distributions of discrete scatterers with coherent potential and quantum mechanical formulism," *J. Appl. Phys.*, vol. 51, no. 7, pp. 3465–3485, July 1980.

[8] L. Tsang, J. A. Kong, and T. Habashy, "Multiple scattering of acoustic waves by random distribution of discrete spherical scatterers with quasicrystalline and Percus-Yevick approximation," *J. Acoust. Soc. Am.*, vol. 71, no. 3, pp. 552–558, Mar. 1982.

[9] L. Tsang, J. A. Kong, K-.H. Ding, and C. O. Ao, *Scattering of Electromagnetic Waves: Numerical Simulations*, Wiley-Interscience, New York, 2001.

[10] S. Chandrasekhar, *Radiative Transfer*, Dover, New York, 1960.

[11] A. Ishimaru, *Wave Propagation and Scattering in Random Media*, Academic Press, New York, 1978.

[12] P. Sheng, *Introduction to Wave Scattering, Localization, and Mesoscopic Phenomena*, Academic Press, San Diego, 1995.

[13] P. Sheng, Ed., *Scattering and Localization of Classical Waves in Random Media*, World Scientific Publishing, Singapore, 1990.

[14] L. Tsang and J. A. Kong, *Scattering of Electromagnetic Waves: Advanced Topics*, Wiley-Interscience, New York, 2001.

[15] C. E. Baum, Ed., *Detection and Identification of Visually Obscured Targets*, Taylor & Francis, Philadelphia, 1999.

[16] I. J. Won, D. A. Keiswetter, and T. H. Bell, "Electromagnetic induction spectroscopy for clearing landmines," *IEEE Trans. Geosci. Remote Sensing*, vol. 39, no. 4, pp. 703–709, Apr. 2001.

[17] I. J. Won, D. A. Keiswetter, D. R. Hanson, E. Novikova, and T. M. Hall, "GEM-3: A monostatic broadband electromagnetic induction sensor," *J. Env. Eng. Geophys.*, vol. 2, pp. 53–64, Mar. 1997.

[18] J. R. Wait, "A conducting sphere in a time varying magnetic field," *Geophysics*, vol. 16, pp. 666–672, 1951.

[19] J. R. Wait, "A conducting permeable sphere in the presence of a coil carrying an oscillating current," *Can. J. Phys.*, vol. 31, pp. 670–678, 1953.

[20] H. Braunisch, C. O. Ao, K. O. Neill, and J. A. Kong, "Magnetoquasistatic response of conducting and permeable prolate spheroid under axial excitation," *IEEE Trans. Geosci. Remote Sensing*, accepted 2001.

[21] K. Sun, K. O'Neill, S. A. Haider, and K. D. Paulsen, "Numerical modeling of scattering from targets with small but non-negligible skin depths," in *Proc. IEEE Int. Geosci. Remote Sensing Symp. (IGARSS)*, Honolulu, July 24–28, 2000, vol. 4, pp. 1411–1414.

[22] F. Shubitidze, K. O'Neill, S. A. Haider, K. Sun, and K. D. Paulsen, "Analysis of induction responses from metal objects using the method of auxiliary sources," in *Proc. 8th Int. Conf. Mathematical Methods in Electromagnetic Theory (MMET)*, Kharkov, Sep. 12–15, 2000, pp. 468–470.

[23] N. Geng, C. E. Baum, and L. Carin, "On the low-frequency natural response of conducting and permeable targets," *IEEE Trans. Geosci. Remote Sensing*, vol. 37, pp. 347–359, Jan. 1999.

[24] T. Oguchi, "Scattering properties of oblate raindrops and cross polarization of radio waves due to rain: calculations at 19.3 and 34.8 GHz," *J. Radio Res. Lab.*, vol. 20, no. 102, pp. 79–118, 1973.

[25] S. Asano and G. Yamamoto, "Light scattering by a spheroidal particle," *Appl. Opt.*, vol. 14, pp. 29–49, Jan. 1975.

[26] M. F. R. Cooray and I. R. Ciric, "Scattering by systems of spheroids in arbitrary configurations," *Comp. Phys. Comm.*, vol. 68, pp. 279–305, 1991.

[27] N. V. Voshchinnikov and V. G. Farafonov, "Optical properties of spheroidal particles," *Astrophys. Space Sci.*, vol. 204, pp. 19–86, June 1993.

[28] L. D. Landau, E. M. Lifshitz, and L. P. Pitaevskii, *Electrodynamics of Continuous Media*, Pergamon, Oxford, 2rd edition, 1984.

[29] C. Flammer, *Spheroidal Wave Functions*, Stanford University Press, Stanford, 1957.

[30] M. Abramowitz and I. A. Stegun, Eds., *Handbook of Mathematical Functions with Formulas, Graphs, and Mathematical Tables*, Dover Publications, New York, 1972.

[31] F. Shubitidze, K. O'Neill, S. A. Haider, K. Sun, and K. D. Paulsen, "Application of the method of auxiliary sources to the wideband electromagnetic induction problem," *IEEE Trans. Geosci. Remote Sensing*, submitted 2000.

[32] H. Braunisch, C. O. Ao, K. O'Neill, and J. A. Kong, "Magnetoquasistatic response of a distribution of small conducting and permeable objects," in *Proc. IEEE Int. Geosci. Remote Sensing Symp. (IGARSS)*, Honolulu, July 24–28, 2000, vol. 4, pp. 1424–1426.

[33] M. A. Karam and A. K. Fung, "Leaf-shape effects in electromagnetic wave scattering from vegetation," *IEEE Trans. Geosci. Remote Sensing*, vol. 27, no. 6, pp. 689–697, Nov. 1989.

[34] W. F. Weeks and S. F. Ackley, "The growth, structure, and properties of sea ice," *CRREL Monograph*, vol. 82-1, 1982.

[35] G. F. N. Cox and W. F. Weeks, "Equations for determining the gas and brine volumes in sea-ice samples," *J. Glaciology*, vol. 29, pp. 306–316, 1983.

[36] Y. Kuga and A. Ishimaru, "Retroreflectance from a dense distribution of spherical particles," *J. Opt. Soc. Am. A*, vol. 1, pp. 831–835, 1984.

[37] L. Tsang, C. Mandt, and K. H. Ding, "Monte Carlo simulations of the extinction rate of dense media with randomly distributed dielectric spheres based on solution of Maxwell's equations," *Opt. Lett.*, vol. 17, no. 5, pp. 314–316, 1992.

[38] C. Mandt, Y. Kuga, L. Tsang, and A. Ishimaru, "Microwave propagation and scattering in a dense distribution of spherical particles: Experiment and theory," *Waves in Random Media*, vol. 2, no. 3, pp. 225–234, 1992.

[39] G. Koh, "Experimental study of electromagnetic wave propagation in dense random media," *Waves in Random Media*, vol. 2, pp. 39–48, 1992.

[40] R. West, D. Gibbs, L. Tsang, and A. K. Fung, "Comparison of optical scattering experiments and the quasicrystalline approximation for dense media," *J. Opt. Soc. Am. A*, vol. 11, no. 6, pp. 1854–1858, June 1994.

[41] L. Tsang and J. A. Kong, "Scattering of electromagnetic waves from a dense medium consisting of correlated mie scatterers with size distributions and applications to dry snow," *J. Electromagnetic Waves and Applications*, vol. 6, no. 3, pp. 265–286, 1992.

[42] L. M. Zurk, L. Tsang, and D. P. Winebrenner, "Scattering properties of dense media from Monte Carlo simulations with application to active remote sensing of snow," *Radio Sci.*, vol. 31, no. 4, pp. 803–819, Jul.-Aug. 1996.

[43] B. Peterson and S. Strom, "T matrix for electromagnetic scattering from an arbitrary number of scatterers and representation of E(3)," *Phys. Rev. D*, vol. 8, pp. 3661–3678, 1973.

[44] J. A. Stratton, *Electromagnetic Theory*, McGraw-Hill, New York, 1941.

[45] E. M. Purcell and C. R. Pennypacker, "Scattering and absorption of light by non-spherical dielectric grains," *Astrophys. Journal*, vol. 186, pp. 705–714, 1973.

[46] B. T. Draine and P. J. Flatau, "Discrete-dipole approximation for scattering calculations," *J. Opt. Soc. Am. A*, vol. 11, pp. 1491–1499, 1994.

[47] L. M. Zurk, L. Tsang, K. H. Ding, and D. P. Winebrenner, "Monte Carlo simulations of the extinction rate of densely packed spheres with clustered and non-clustered geometries," *J. Opt. Soc. Am. A*, vol. 12, pp. 1772–1781, Aug. 1995.

[48] O. R. Cruzan, "Translational addition theorems for spherical vector wave functions," *Quart. J. Appl. Math.*, vol. 20, pp. 33–40, 1962.

[49] M. F. R. Cooray and I. R. Ciric, "Rotational-translational addition theorems for vector spheroidal wave functions," *Compel*, vol. 8, no. 3, pp. 151–166, 1989.

[50] N. Metropolis, A. W. Rosenbluth, N. Rosenbluth, A. H. Teller, and E. Teller, "Equation of state calculation by fast computing machines," *J. Chem. Phys.*, vol. 21, no. 6, pp. 1087–1092, 1953.

[51] J. W. Perram, M. S. Wertheim, J. L. Lebowitz, and G. O. Williams, "Monte Carlo simulation of hard spheroids," *Chem. Phys. Lett.*, vol. 105, no. 3, pp. 277–280, Mar. 1984.

[52] P. G. de Gennes, *The Physics of Liquid Crystals*, Clarendon Press, Oxford, 1975.

[53] J. W. Perram and M. S. Wertheim, "Statistical mechanics of hard ellipsoids. I. Overlap algorithm and the contact function," *J. Comp. Phys.*, vol. 58, pp. 409–416, 1985.

[54] J. A. Barker and D. Henderson, "What is "liquid"? understanding the states of matter," *Rev. Mod. Phys.*, vol. 48, no. 4, Oct. 1976.

[55] J. M. Ziman, *Models of Disorder*, Cambridge University Press, Cambridge, 1979.

[56] M. P. Allen and D. J. Tildesley, *Computer Simulation of Liquids*, Oxford University Press, New York, 1989.

[57] L. Tsang, K. H. Ding, S. E. Shih, and J. A. Kong, "Scattering of electromagnetic waves from dense distributions of spheroidal particles based on Monte Carlo simulations," *J. Opt. Soc. Am. A*, vol. 15, no. 10, pp. 2660–2669, Oct. 1998.

[58] R. F. Harrington, *Field Computation by Moment Methods*, Macmillan, New York, 1968.

[59] A. D. Yaghjian, "Electric dyadic Green's functions in the source region," *Proc. IEEE*, vol. 68, no. 2, pp. 248–263, Feb. 1980.

[60] P. M. Morse and H. Feshbach, *Methods of Theoretical Physics*, McGraw-Hill, New York, 1953.

[61] G. H. Goedecke and S. G. O'Brien, "Scattering by irregular inhomogeneous particles via the digitized Green's function algorithm," *Applied Optics*, vol. 27, no. 12, pp. 2431–2438, 1988.

[62] B. T. Draine, "The discrete-dipole approximation and its application to interstellar graphite grains," *Astrophys. Journal*, vol. 333, pp. 848–872, Oct. 1988.

[63] H. A. van der Vorst, "Bi-CGSTAB: A fast and smoothly converging variant of Bi-CG for the solution of nonsymmetric linear systems," *SIAM J. Scientific and Statistical Computing*, vol. 13, no. 2, pp. 631–644, 1992.

[64] L. Tsang, M. C. Kubacsi, and J. A. Kong, "Radiative transfer theory for active remote sensing of a layer of small ellipsoidal scatterers," *Radio Sci.*, vol. 16, no. 3, pp. 321–329, May-Jun. 1981.

[65] V. Twersky, "Coherent scalar field in pair-correlated random distributions of aligned scatterers," *J. Math. Phys.*, vol. 18, pp. 2468–2486, 1977.

[66] L. Tsang, "Scattering of electromagnetic waves from a half space of nonspherical particles," *Radio Sci.*, vol. 19, pp. 1450–1460, 1984.

[67] V. V. Varadan, Y. Ma, and V. K. Varadan, "Anisotropic dielectric properties of media containing aligned nonspherical scatterers," *IEEE Trans. Antennas Propagat.*, vol. 33, no. 8, pp. 886–890, Aug. 1987.

[68] V. V. Varadan, V. K. Varadan, Y. Ma, and W. A. Steele, "Effects of nonspherical statistics on EM wave propagation in discrete random media," *Radio Sci.*, vol. 22, no. 4, pp. 491–498, 1987.

[69] J. K. Percus and G. J. Yevick, "Analysis of classical statistical mechanics by means of collective coordinates," *Phys. Rev.*, vol. 110, pp. 1–13, 1958.

[70] M. S. Wertheim, "Exact solution of the Percus-Yevick integral equation for hard spheres," *Phys. Rev. Lett.*, vol. 20, pp. 321–323, 1963.

[71] M. S. Wertheim, "Analytical solution of the Percus-Yevick equation," in *Equilibrium Theory of Classical Fluids*, H. L. Frisch and J. L. Lebowitz, Eds., pp. 181–230. W. A. Benjamin, Inc., New York, 1964.

[72] E. Thiele, "Equation of state for hard spheres," *J. Comp. Phys.*, vol. 39, pp. 474–479, 1963.

[73] J. P. Hansen and I. R. McDonald, *Theory of Simple Liquids*, Academic Press, New York, 1986.

[74] J. L. Lebowitz and J. W. Perram, "Correlation functions for nematic liquid crystals," *Molecular Phys.*, vol. 50, no. 6, pp. 1207–1214, 1983.

[75] L. Tsang, J. A. Kong, and R. T. Shin, *Theory of Microwave Remote Sensing*, Wiley, New York, 1985.

[76] M. Lax, "The multiple scattering of waves. II. The effective field in dense systems," *Phys. Rev.*, vol. 85, no. 4, pp. 621–629, 1952.

[77] P. Soven, "Coherent-potential model of substitutional disordered alloys," *Phys. Rev.*, vol. 156, pp. 809–813, 1967.

[78] B. L. Gyorffy, "Electronic states in liquid metals: A generalization of the coherent-potential approximation for a system with short-range order," *Phys. Rev. B*, vol. 1, pp. 3290–3299, 1970.

[79] J. Korringa and R. L. Mills, "Coherent-potential approximation for random systems with short range correlations," *Phys. Rev. B*, vol. 5, pp. 1654–1655, 1972.

[80] K.-H. Ding and L. Tsang, "Effective propagation constants and attenuation rates in media of densely distributed coated dielectric particles with size distributions," *J. Electromagnetic Waves and Applications*, vol. 5, no. 2, pp. 117–142, 1991.

[81] A. H. Sihvola, *Electromagnetic Mixing Formulas and Applications*, The Institution of Electrical Engineers, London, 1999.

[82] N. Harfield, "Conductivity calculation for a two-phase composite with spheroidal inclusions," *J. Phys. D: Appl. Phys.*, vol. 32, pp. 1104–1113, 1999.

[83] A. H. Sihvola and J. A. Kong, "Effective permittivity of dielectric mixtures," *IEEE Trans. Geosci. Remote Sensing*, vol. 26, no. 4, pp. 420–429, July 1988.

[84] B. E. Barrowes, C. O. Ao, F. L. Teixeira, J. A. Kong, and L. Tsang, "Monte Carlo simulation of electromagnetic wave propagation in dense random media with dielectric spheroids," *IEICE Trans. Electron.*, vol. E83-C, no. 10, Dec. 2000.

[85] G. F. Williams, “Microwave radiometry of the ocean and the possibility of marine wind velocity determination from satellite observations,” *J. Geophys. Res.*, vol. 74, no. 18, pp. 4591–4594, 1969.

[86] J. Hollinger, “Passive microwave measurements of the sea surface,” *J. Geophys. Res.*, vol. 75, no. 27, pp. 5209–5213, 1970.

[87] W. Nordberg, J. Conaway, D. Ross, and T. Wilheit, “Measurements of microwave emission from a foam covered, wind driven sea,” *J. Atmos. Sci.*, vol. 28, pp. 429–435, 1971.

[88] P. M. Smith, “The emissivity of sea foam at 19 and 37 GHz,” *IEEE Trans. Geosci. Remote Sensing*, vol. 26, no. 5, pp. 541–547, Sep. 1988.

[89] J. D. Droppleman, “Apparent microwave emissivity of sea foam,” *J. Geophys. Res.*, vol. 75, no. 3, pp. 696–698, Jan. 1970.

[90] P. W. Rosenkranz and D. H. Staelin, “Microwave emissivity of ocean foam and its effect on nadiral radiometric measurements,” *J. Geophys. Res.*, vol. 77, no. 33, pp. 6528–6538, Nov. 1972.

[91] D. B. Kunkee and A. J. Gasiewski, “Simulation of passive microwave wind direction signatures over the ocean using an asymmetric-wave geometrical optics model,” *Radio Sci.*, vol. 32, no. 1, pp. 59–78, Jan.–Feb. 1997.

[92] S. H. Yueh, “Modeling of wind direction signals in polarimetric sea surface brightness temperatures,” *IEEE Trans. Geosci. Remote Sensing*, vol. 35, no. 6, pp. 1400–1418, Nov. 1997.

[93] A. Stogryn, “The emissivity of sea foam at microwave frequencies,” *J. Geophys. Res.*, vol. 77, no. 9, pp. 1658–1666, Mar. 1972.

[94] Y. Zhang, *Forward and Inverse Problems in Microwave Remote Sensing of Objects in a Complex Medium*, Ph.D. thesis, Massachusetts Institute of Technology, 1999.

[95] L. Tsang, C.-T. Chen, A. T. C. Chang, J. Guo, and K-.H. Ding, "Dense media radiative transfer theory based on quasicrystalline approximation with applications to passive microwave remote sensing of snow," *Radio Sci.*, vol. 35, no. 3, pp. 731–749, 2000.

[96] L. Tsang and J. A. Kong, "Effective propagation constants for coherent electromagnetic wave propagation in media embedded with dielectric scatterers," *J. Appl. Phys.*, vol. 53, no. 11, pp. 7162–7173, Nov. 1982.

[97] M. Born and E. Wolf, *Principles of Optics*, Pergamon Press, New York, 5th edition, 1983.

[98] L. A. Klein and C. T. Swift, "An improved model for the dielectric constant of sea water at microwave frequencies," *IEEE Trans. Antennas Propagat.*, vol. 25, no. 1, pp. 104–111, 1977.

[99] H. L. Chan and A. K. Fung, "A theory of sea scatter at large incident angles," *J. Geophys. Res.*, vol. 82, no. 24, pp. 3439–3444, 1977.

[100] C. Cox and W. Munk, "Measurement of the roughness of the sea surface from photographs of the sun's glitter," *J. Opt. Soc. Am.*, vol. 44, no. 11, pp. 838–850, Nov. 1954.

[101] J. A. Kong, *Electromagnetic Wave Theory*, EMW Publishing, Cambridge, MA, 2000.

[102] H. C. Chen, *Theory of Electromagnetic Waves: a Coordinate-Free Approach*, McGraw-Hill, New York, 1983.

[103] W. S. Weiglhofer, “Dyadic Green’s functions for general uniaxial media,” *IEE Proc. H (Microwaves, Antennas and Propag.)*, vol. 137, no. 1, pp. 5–10, Feb. 1990.